Miocene humid intervals and establishment of drainage networks by 23 Ma in the Central Sahara, Southern Libya

Mark W. Hounslow*[a], Helena White[b], Nick A. Drake[c], Mustafa J. Salem[d], Ahmed El-Hawat[e], Sue J. McLaren[b], Vassil Karloukovski[a], Stephen R. Noble[f], Osama Hlal[d].

[a] Lancaster Environment Centre, Lancaster University, Bailrigg, Lancaster, LA1 4YW, UK (m.hounslow@lancaster.ac.uk)

[b] Department of Geography, University of Leicester, University Road, Leicester LE1 7RH, UK (hew12@leicester.ac.uk and sjm11@leicester.ac.uk)

[c] Department of Geography, Kings College, London WC2R 2LS, UK (nick.drake@kcl.ac.uk)

[d] Department of Geology, Faculty of Science, University of Tripoli, P.O. Box 13040 and 13258, Tripoli, Libya (southlibya@gmail.com and osama.hlal@gmail.com)

[e] Earth Sciences Department, University of Garyounis, P.O. Box 1308, Benghazi, Libya (ashawat@hotmail.com)

[f] NERC Isotope Geosciences Laboratory, British Geological Survey, Keyworth, Nottingham, NG12 5GG, UK (srn@bgs.ac.uk)

*Corresponding author

Abstract

Terrestrial and lacustrine Neogene and Quaternary sediments in the Libyan Fezzan provide key evidence for paleoclimate changes in the central Sahara, associated with Lake Megafezzan. Understanding of Holocene and late Pleistocene deposits is resolved, but the age of older sediments is not. We provide the first high-resolution chronology and stratigraphy of the Neogene deposits in the Fezzan Basin, and so also the central Sahara. The sediments are divided into three unconformity-bounded units, the oldest unit, comprising the Shabirinah and Brak formations, is dated using magnetostratigraphy. The Shabirinah Formation is a succession of lacustrine and fluvial units, locally with humid and arid paleosols, which progressively show evidence of increasing aridity up through the succession. The overlying Brak Formation is a pedogenically modified palustrine limestone at basin margin locations. All these units are dated to the early Aquitanian to late Serravallian in the early to mid-Miocene, having formed prior to major volcanic fields to the east. During the mid-late Aquitanian widespread stromatolitic lake sediments developed in SE Fezzan. In the late Burdigalian palustrine carbonate units developed that typically pass laterally into mixed clastic-paleosol-carbonate units that characterise basin margin situations. The Serravallian-aged Brak Formation is a highstand deposit developed during maximum

lake extent, which formed due to restriction of basin drainage to the north and east, due to growth of the Jabal as Sawda volcanic centre and uplift of the SW shoulder of the Sirte Basin. Gradual aridification of the central Sahara occurred from the early Miocene, but this trend was periodically interrupted by humid phases during which Lake Megafezzan developed. The hyperaridity of the central Sahara must have developed after 11 Ma and the main drainage networks from the Fezzan Basin were established before 23 Ma, in the Oligocene indicating the great antiquity of major central Saharan river basins.

1. Introduction

Lake Megafezzan is hypothesised as a giant paleolake that periodically existed in south-west Libya during past Saharan humid phases (Thiedig et al., 2000 ; Drake et al., 2008). This lake has been proposed as important evidence for the greening of the Sahara, allowing early hominins to migrate northwards out of east Africa (Drake et al., 2011a; Drake et al., 2013 ; Larrasoaña et al., 2013). Our understanding of climate change in the Sahara during the Holocene is reasonably well understood (Lézine et al., 2011 ; Drake et al., 2011a), and we are beginning to gain an understanding of the Middle to Upper Pleistocene climate change (Pachur and Hoelzmann, 2000; Larrasoaña et al., 2013 ; Drake et al., 2013). However, for earlier age intervals knowledge is limited and often controversial, particularly the onset of the Sahara Desert, where late Miocene dune systems are thought to be preserved in northern Chad (Schuster et al., 2006), in contrast to the supposed wetter and warmer late Miocene climate based on fossil evidence (Wanas et al., 2009 ; Stoetzel, 2013). Addressing this issue, climate models have been proposed for the late Miocene, often with conflicting results (Bradshaw et al., 2012 ; Zhang et al., 2014), but crucially with little solid data to validate them against well-dated sedimentary successions in the central Sahara.

Based on interfluve height assessments from digital elevation models, Lake Megafezzan had a maximum potential size of ca. 135,000 km2 (Drake et al., 2008); but its area likely depended on the intensity of humid phases, and the nature of its connection to drainage channels east and north-eastwards into the Sirte Basin. The paleolake deposits since ca. 400 ka have been well studied and dated (Petit-Maire et al., 1980; Thiedig and Geyh, 2004; Armitage et al., 2007 ; Geyh and Thiedig, 2008). In addition, channel networks draining southern Libya and its surroundings, have been proposed for various time intervals since the late Miocene (Drake et al., 2008; Drake et al., 2011a ; Paillou et al., 2009). Those thought to be the most important drainage systems from the Fezzan Basin (Drake et al., 2008 ; Drake et al., 2011a), are directed through NE and eastern routes along Wadi Nashu and Wadi Barjuj (Fig. 1), ultimately outflowing into the Gulf of Sirte.

However, detailed data about the lacustrine and fluvial sediments for the age interval prior to the Upper Pleistocene has not been described. This is in part due to a lack of a

detailed chronology and understanding of regional relationships for these older units; even though widespread limestone and clastic units have been mapped (e.g. Koráb, 1984; Parizek et al., 1984 ; Seidl and Röhlich, 1984; Fig. 1). During fieldwork in the Fezzan between 2005 and 2011, we recognised extensive sedimentary sequences exposed beneath deposits dated to the Middle Pleistocene by Geyh and Thiedig (2008), that could potentially help fill this gap (Fig. 1). We here outline a new regional lithostratigraphic framework for these deposits.

In North Africa, the chronology of late Cenozoic terrestrial successions is largely based on vertebrate fossils, which are rather rare and appear to be largely restricted to localities off the Sahara platform (Stoetzel, 2013), with scant occurrences from the central Sahara (Boaz et al., 2008). Our new lithostratigraphic framework is securely tied to a detailed chronology, using magnetostratigraphy, which so far in studies of the late Cenozoic of the central Sahara, has yielded only ambiguous evidence of age (Beyer, 2008); although magnetostratigraphic dating of Moroccan Miocene successions has resolved high-resolution ages in parallel with biochronology (Benammi and Jaeger, 2001).

With the new detailed chronology, we evaluate the regional stratigraphic relationships of these Lake Megafezzan sediments, re-assess the relationships between the sediment successions and the volcanic centres to the north and east, that have been inferred to restrict basin drainage. We assess the implications of this chronology on the north-Saharan paleoclimate and proposed paleohydrology before the beginning of the hyperarid Sahara.

2. Geological setting and stratigraphic framework

The Fezzan Basin is a broad post-Paleogene depression bounded by uplifted shoulders of the Sirte Basin to the east and the Al Hamadah al Hamra escarpment to the north (Fig. 1), along with older uplifted Paleozoic successions to the northeast (Qarqaf), SE (Dur al Qussah) and SW (Jabal Akakus). Neogene and younger sediments are scattered across the Fezzan, broadly on the fringes of the Awbari and Murzuq Sand seas, since these sediments also underlie the modern dune systems (Fig. 1).

Sediments of Lake Megafezzan have been called the ‘Al Mahruqah formation’ by Theidig et al., (2000) and Geyh and Thiedig (2008). However, a new lithostratigraphy of these units is needed for the following four reasons. First, we have examined a wide variety of units over a large part of the Fezzan Basin, and none of the existing member designations for units of the ‘Al Mahruqah formation’ (Thiedig et al., 2000; Geyh and Thiedig, 2008) can be adequately applied to our sections. Secondly, in the mapping of the Fezzan Basin, the naming and usage of this unit is inconsistent. The same units have been given different names in different geological maps, ranging from the Al Mahruqah formation in the Al

Fuqaha, Al Haruj al Abyad and Sabha maps (Seidl and Röhlich, 1984; Woller, 1984; Korab, 1984) to 'continental deposits' in the Awbari and Hamadat Tanghirt maps (Gundobin, 1985; Roncevic, 1984; Berendeyv, 1985; Grubic et al., 1991), to both these units on the Tmassah and Idri geological maps (Parizek et al., 1984; Koráb, 1984). Thirdly, originally Seidl and Röhlich (1984), and later Domaci et al. (1991) and El Ebaidi and Abdulsamad, (2005) applied the 'Al Mahruqah formation' to the carbonate unit (termed the Brak Formation here) exposed on the north side of Wadi ash Shati, when in fact the major thickness of these post-Oligocene sediments in Wadi ash Shati are clastic deposits, with minor carbonates. Finally, Thiedig et al. (2000) expanded the 'Al Mahruqah formation' to include all the 'Pleistocene' to Holocene carbonate units, whereas our work shows some of these units are much older than Pleistocene, and range into the Miocene, as inferred by earlier mapping (Collomb, 1962; Goudarzi, 1970). The new lithostratigraphic framework fits existing and new data into a more detailed stratigraphic sub-division, and allows our new descriptions, and age assignments to be tied into the findings of prior research.

This new framework upgrades the Al Mahruqah formation to group status, the Al Mahruqah Group, that includes all the clastic units, not just the carbonates (Fig. 2). The Al Mahruqah Group includes two major unconformities bounding different sediment packages, thus the expansion to Group status allows a more detailed lithostratigraphic designation of these units. Lithostratigraphic boundaries imply no age information, just the stratigraphic order of the successions in the Fezzan Basin, based on evidence described. This lithostratigraphy applies to all previously mapped deposits, from those found on the fringes of the Awbari Sand Sea and east towards the western edges of the Paleogene and Eocene outcrops in the SW fringes of the Sirte Basin in Sarir al Qattusah, and south towards Tmassah turning east along Wadi ash Shabirinah (Fig. 1). Neogene and younger deposits exist on the fringes of the Murzuq Sand Sea, but these have not been investigated by us.

Three new formations are proposed; the Shati Formation, the Zarzur Formation and the Shabirinah Formation (Fig. 2). This is in addition to the Brak Formation, which is upgraded from the Brak member, used previously by Thiedig et al. (2000) and Geyh and Thiedig (2008). The units of the Al Mahruqah Group all unconformably overly various older strata ranging in age from the Cretaceous to the Cambrian. The lithostratigraphy is illustrated with detailed section logs, coded into three regions (Fig. 1): SK for the Wadi ash Shati to Wadi Kunayr region (Fig. 5); NU for the northern Awbari Sand Sea area (Si Fig. S1) and TS for the Tmassah- Wadi ash Shabirinah region (Fig. 1). A brief description of these new formations is provided below whilst a formal lithostratigraphic description of the formations and their members is detailed in the Supplementary Information. Our on-going chronology work on the younger Zarzur Formation will be published elsewhere.

2.1. Lithostratigraphy for the Al Mahruqah Group

2.1.1. Shabirinah Formation

The Shabirinah Formation underlies the Brak Formation, and its lower parts are dominated by the Tmassah Member of clear fluvial-origin with down-cutting channels, which show paleocurrents and channel systems directed to the ESE to SE (Fig. 6). These channels cut into the red mudstones forming the upper part of the Stromatolite Member (sections TS2 and TS3, Fig. 6 and Supplementary data). The Tmassah Member is overlain by the Kunayr Member which typically shows (but not always) an upwards increase in calcretisation, often within a predominantly clastic succession. This bipartite-facies association (i.e. fluvial siliciclastics, below calcretised clastics) can be recognised throughout the Fezzan, even at basin margin locations, where the lower fluvial-dominated part of the Shabirinah Formation may be channel conglomerates. At some locations lateral to the channels rootleted aeolian facies probably occur, but still retaining the overlying carbonate-rich Kunayr Member (section TS6, Fig. 6). In the north side of Wadi ash Shabirinah lacustrine limestones (in sections TS2, TS3) in the base of the Kunayr Member pass laterally eastwards (at sections TS4, TS5, TS6) into nodular calcretes and calcretised palustrine limestones, indicating the basin centre of the Kunayr Member was to the west or SW of section TS2 and TS3. The oldest two members of the Shabirinah Formation occur along the northern fringe of Wadi ash Shabirinah, along Wadi Maharshim and in the 'Qattusah corridor' to the north (Fig. 1, Fig. 3 ; Fig. 5).

Near Tmassah, Thiedig et al. (2000) has also illustrated stromatolitic beds which probably belong to our Stromatolite Member (but they assigned them to their Bir az Zallaf Member - i.e. their plates 1e,1f, 3h,5c). This distinctive bed can be traced westwards along the north side of Wadi ash Shabirinah towards Tmassah. It can be found again in the outcrops north and NW of Tmassah (Fig. 5). This same distinctive bed has been seen by us some 118 km north of Tmassah at 27°26′2.8″N; 15°34′15.6″E. The overlying Kunayr Member was also seen 4 km to the west at 27°25′7.2″N; 15°32′4.2″E. The Stromatolite Member in Wadi ash Shabirinah appears to pass eastwards into clastic-rich units of the Tmassah Member (Fig. 6), making it distinctly different from palustrine carbonates in the Kunayr Member, which pass eastwards into palustrine limestones, more pedogenically- modified.

Where we have seen the base of the Shabirinah Formation, it rests on Mesozoic or Paleozoic formations, and to our knowledge has no other intervening clastic or carbonate units (Fig. 3 ; Fig. 6). The NE rim of the basin in which the Shabirinah Formation developed was Cretaceous to Eocene sediments of the Sarir al Qattusah and Dur al Msid (Fig. 1 ; Fig. 5), uplifted in the late Oligocene when clastic supply to the western Sirte basin increased (Abouessa et al., 2012) and gentle folding developed in the Zallah Trough (Abdunaser and McCaffrey, 2015; Fig. 1)..

2.1.2. Brak Formation

The Brak Formation consists of various Fe-poor dolomitic and micritic limestones. The sediments are highly indurated, showing multiple cementation phases and are typically extensively mottled and brecciated. Abdullah (2010) previously classed the Brak Formation sediments in Wadi ash Shati as groundwater calcretes, however the limestones do not have chalky, nodular or laminated textures of other calcretes (Alonso-Zarza, 2003). A groundwater calcrete origin also seems less-likely, in that the boundaries of the limestone are diffuse, and the formation is also very thick compared to most other groundwater calcretes (cf. Alonso-Zarza, 2003). The Brak Formation instead shares most characteristics with modified palustrine limestones (Wright and Platt, 1995 ; Freytet and Verrecchia, 2002) and thus likely indicates the formation is a basin-margin palustrine limestone, with the main Brak basin centre somewhere to the southwest of the Qattusah corridor and south of Brak (Fig. 1 ; Fig. 3).

In Wadi ash Shati the Brak Formation oversteps and on-laps the basement to the north, showing that it represents an expression of the maximum fill of the 'Brak-basin', with the Brak Formation representing the highstand unit of its underlying successions.

Seidl and Röhlich (1984) and Domaci et al. (1991), report ostracods, gastropods and bivalves from this unit, but the more extensive studies of Abdullah (2010) from the Brak area do not record such findings, concurring with our observations. It may be these earlier studies confused Brak Formation carbonates with the Bir az Zallaf Member carbonate units (which can be locally calcretised), or it could be they identified more basinal correlatives of the Brak Formation, which might be expected more centrally in the Fezzan.

The Brak Formation in its type area in Wadi ash Shati (near Brak) occupies heights which range from 390 m (at SK-3 section, Fig. 4 ; Fig. 7) to ca. 438 m on the southern flanks of the Qarqaf uplift, on the northern fringes of Wadi ash Shati (Fig. 1 ; Fig. 7). ENE of Ashkidah the base of the Brak Formation rises to ca. 435 m, with the top of the Brak Formation to the NE of this area, around 457 m, at Geyh and Thiedig (2008) Brak 'member' site 8 (Fig. 7). These E-W differences in elevation reflect some tilting (or faulting) after deposition of the Brak Formation. In most of the outcrops in Wadi ash Shati the Brak Formation rests directly on a heavily calcretised basement breccia between 2 and 5 m thick, sometimes having the appearance of cemented scree (Abdullah, 2010). In one southerly outcrop (section SK-3) in Wadi ash Shati the lower parts of the formation overly and grade into siliciclastics and red mudstones that we assign to the underlying Shabirinah Formation (Fig. 7).

Basalt fragments (from the Jabal as Sawda volcanics?) have been reported from the basal breccias in the Brak Formation in Wadi ash Shati (Goudarzi, 1970). This indicates the Brak Formation there is younger, or its early parts are coeval, with the Jabal as Sawda

volcanic field to the NE. Similarly, north of Wadi Kunayr, map evidence (Woller, 1984) shows basalts of the Jabal as Sawda volcanic centre interbedded in the boundary interval between the Shabirinah Formation and the overlying Brak Formation (Fig. 8). In Wadi Kunayr the underlying Shabirinah Formation fills a paleo-wadi, since the Paleozoic and Mesozoic basement rises to the north and south (Fig. 8).

We have not documented the transition between the Brak Formation and the top of the underlying Shabirinah Formation in the Wadi Kunayr area (Fig. 4), but infer that the Brak Formation terminates the upwards increase in calcretisation we see through the underlying Shabirinah Formation, so the transition is inferred to be conformable to the north of Wadi Kunayr (Fig. 7). In the outcrops east of Tmassah (Fig. 1, Fig. 5 ; Fig. 6) the contact between the Brak and Shabirinah formation appears to be conformable or there is a south-westwards (i.e. towards basin centre) lateral transitional from heavily calcretised palustrine limestones and clastics at basin margins to more clastic-rich units in the upper parts of the Shabirinah Formation. In the south of the Sarir al Qattusah (Fig. 1), the thickest carbonates (the Brak Formation) appear to be restricted to the NE margin of the outcrops (Fig. 5). In the area north of Tmassah, El Ebaidi and Abdulsamad (2005) and Domaci et al. (1991) also record the possible(?) conformable transition between the Brak Formation (their Al Mahruqah) and the underlying clastic continental deposits (our Shabirinah Formation).

2.1.3. Zarzur Formation

The Zarzur Formation largely consists of green to tan-coloured siliciclastic units, of coarse-silt to coarse-sand, often heavily rootleted (and poorly consolidated), but occasionally containing cross-bedded intervals. This formation includes the unit attributed to the Bir az Zallaf Member of Geyh and Thiedig (2008). From their lithostratigraphic description, it is clear their Bir az Zallaf unit largely relates to the two to three limestone beds of the Bir az Zallaf Member at the top of our Zarzur Formation, and not the ca. 60 m of underlying clastics found at Bir az Zallaf (Fig. 9 and Supplementary data). The inverted stratigraphic elevation in Wadi ash Shati, and unconformable relationships with the overlying Shati Formation clearly shows the Zarzur Formation is much older than the Shati Formation (Fig. 3, Fig. 4 ; Fig. 9). This is also borne-out by saturated and near saturated OSL dates (> 420 ka) from the top of the Zarzur Formation (Armitage et al., 2007).

The base of the Zarzur Formation is marked by a major erosional unconformity, which in Wadi ash Shati cuts down into the underlying Paleozoic (Fig. 9). Similar relationships are seen in the Qarārat al Marār area in the northern Awbari Sand Sea (Fig. 1 ; Fig. 3 and supplementary Figs. S3, S4). This lower elevation of the earliest Zarzur Formation with respect to the Brak Formation (Fig. 9), signifies a major interval of erosion of the Brak Formation and older units, prior to Zarzur Formation deposition. However, we have not seen

any location where the Zarzur Formation rests on the Brak Formation. Only in the northern Awbari Sand Sea area, do we see the Zarzur Formation resting on what we interpret as the Shabirinah Formation (section NU2-b, Supplementary data Fig. S4). However, like Geyh and Thiedig (2008), we consider the Brak Formation to be an older unit of the Al Mahruqah Group, because of the inverted stratigraphy clearly seen in Wadi ash Shati (Fig. 9). In Wadi ash Shati the youngest units of the Zarzur Formation range up to ca. 379 m elevation. In the Qarārat al Marār area (Fig. 1) the youngest units of the Zarzur Formation range up to an elevation of 400 m, and in Wadi Tanarat up to 577 m (Supplementary data Figs. S3, S4). Hence, elevations as used by Geyh and Thiedig (2008) to infer relative age, is an erroneous assumption. Equivalents of the Zarzur Formation occur on the northern fringes of the Murzuq Sand Sea, but we have not investigated these in detail, however our reconnaissance observations share similarities with those of Geyh and Thiedig (2008).

The Zarzur Formation locally contains an impoverished, often poorly preserved fauna of ostracods, gastropods and rare bivalves and charophytes (Domaci et al., 1991 ; Abdullah, 2010). Basin-margin representatives of the Zarzur Formation are known from the Qarārat al Marār area, where the clastic units are replaced by fluvial conglomerates (section NU2-c, NU2-b, Supplementary data Figs. S3, S4) and the carbonate units can be laterally substituted by several metres of calcretised limestone resting on basement (section NU3-e; Supplementary data Fig. S4).

2.1.4. Shati Formation

The Shati Formation consists of a wide variety of lacustrine sediments deposited since the Upper Pleistocene. This includes the coquinas of the Aqar Member with ages around 100–125 ka (Petit-Maire et al., 1980; Armitage et al., 2007 ; Geyh and Thiedig, 2008). Various fossiliferous late Pleistocene to middle Holocene poorly cemented silts and muds, have also been widely investigated (White et al., 2000; Armitage et al., 2007; Drake et al., 2008 ; Cremaschi and Zerboni, 2009), which are here assigned to the Bir al Hasy Member (Fig. 2 ; Fig. 3). These units give OSL and radiocarbon, dates from 12 to 3 ka. The base of the Shati Formation is marked by a major erosional unconformity everywhere in the Fezzan. In Wadi ash Shati this unconformity cuts down into the underlying Zarzur Formation and other older units of the Al Mahruqah Formation, so the top of the Shati Formation occupies similar elevations to the lower parts of the Zarzur Formation (Fig. 9). Similar relationships are seen in the Qarārat al Marār area (Fig. 1) in the Northern Awbari Sand Sea and in Wadi al Ajal (west-northwest of the Murzuq Sand Sea).

3. Sampling for chronology

Three sections were sampled in 2009 for magnetostratigraphy to investigate the age of the Brak and Shabirinah formations (Table 1 and Fig. 10). Section SK8 is exposed along a trackway into Wadi Kunayr, through south and SW facing bluffs below the Areal Agricultural Station on the plateau top (Fig. 4 ; Fig. 7). The SK8 section represents the Kunayr Member and the underlying parts of the Shabirinah Formation. The lower few metres of this succession are composed of reddish mudstones and sandstone, overlain by black to maroon silty paleosols, capping fining-up channel sandstones (Fig. 10). The channels of the sandstone units are well exposed 3.7 km to east of section SK8 (at 27°,39′,50.3″N;15°,10′,18.2″E), where they are oriented towards 135°, with shallow channels up to ca. 200 m wide. The Kunayr Member consists of mottled and rootleted sandstones, locally with nodular calcrete development, some within paleosol horizons. The documented section ends with paleochannels that show complex down-cutting relationships that make stratigraphic correlations with respect to overlying units unclear. This carbonate-rich upper-most unit is exposed extensively on the plateau to the N and NE of the section and is probably transitional into the Brak Formation, since Geyh and Thiedig (2008) identified the Brak Formation some 33 km to the NE (Fig. 8), some 15–20 m stratigraphically above the top of the measured section.

The lower boundary of the Kunayr Member can be traced westwards along the bluffs for around 7 km, with the basement elevation rising to the NW (Figs. 5, 6). The extent of the Shabirinah Formation outcrops to the east was not fully investigated, but satellite imagery suggests it may extend 20 -40 km eastwards, and then rest on the Maastrichtian (Woller, 1984).

Section ID	Thickness (m)	No. composite sections	No. Paleomag. samples and code	Stratigraphic Units
SK-3	18.9	2	25 [BC]	Brak Fm, Shabirinah Fm
SK-8	39.2	4	59 [AP]	Kunayr Mbr, Shabirinah Fm
TS-3	27.8	5	43 [TM]	Kunayr Mbr, Tmassah Mbr, Stromatolite Mbr, Maharshim Mbr

Table 1. Sections sampled for magnetostratigraphy. See Supplementary Table S1 for latitude/longitude location information, and Figs. 5, 8 for map locations. SK sections are in the Wadi ash Shati to Wadi Kunayr area. TS sections are in the Tmassah to Wadi ash Shabirinah area. The TS3 section was also sampled for radiometric dating (Fig. 9).

Section TS3 is the proposed type section of the Tmassah and Stromatolite Members of the Shabirinah Formation (Fig. 6 ; Fig. 10). The section is dominated by clastic units, but contains well-developed lacustrine limestone beds towards the base (lower part of Stromatolite Member) and in the basal and lower parts of the Kunayr Member. The red mudstones of the upper part of the Stromatolite Member thicken considerably a little to the south and west (e.g. section TS2; Fig. 6), indicating the Tmassah Member here is an incised channel (i.e. there is a hiatus at the base of this member). The Stromatolite Member continues for at least another 3 km to the east (to 26°,30′,55.3″N;16°,31′,57.6″E), and was seen 9.3 km to the west (at 26°,31′,47.9″N;16°,24′,31.7″E) in this area. In the TS3 section the upper part of the Kunayr Member is exposed in a hillside (at 26°,30′,47.9″N;16°,30′,6.6″E), which is capped by a rootleted silica-cemented sandstone. The same sandstone bed was seen capping plateaus 11 km to the east (at 26o,30′,32.8″N;16o,36′,43.8″E). Samples from the carbonate bed in the Stromatolite Member in sections TS2 and TS3 were sampled for U-Th and U-Pb dating (Supplementary data Table S2).

The SK3 section was exposed in a working quarry in central Wadi ash Shati (Figs. 1,6, 10). This section is the type location of the 'Al Mahruqah formation' of Seidl and Röhlich (1984), and of our Brak Formation. The lower part of the section is composed of red mudstones with green mottling, passing up into a calcareous sandstone- sandy limestone, which in turn grades up into the main limestone rich part of the Brak Formation (Fig. 10).

In total 127 paleomagnetic samples were collected from these three sections, and located onto sedimentary logs (Fig. 10). The samples were oriented using a compass. About 60% of the samples (other than the well-cemented limestones and calcretes) were poorly consolidated, and were impregnated with a 2:1 mix of Na- silicate and water (Kostadinova et al., 2004) to consolidate them prior to cutting into specimens. For some of these samples, this impregnation process started in the field, and was left to dry and harden overnight before orientating and packing for transport. After further consolidation in the laboratory, cubic specimens were cut from the hand samples using a circular saw, often re-treating the specimen slices several times during this process to consolidate them for final specimen preparation.

3.1. Laboratory Methodology

Low field magnetic susceptibility (K_{lf}) was measured using a Bartington MS2B sensor. Measurements of Natural Remanent Magnetisation (NRM) were made using a CCL 3-axis cryogenic magnetometer (noise level ~0.002 mA/m), using multiple specimen positions, from which the magnetisation variance was determined. Generally 2 to 3 specimens from each sample were subjected to stepwise thermal demagnetisation, using a Magnetic Measurements Ltd thermal demagnetiser, in 100 °C steps up to 400°C, followed by 30°C

steps until around 630°C, sometimes 650°C, or until instability set-in or the specimen demagnetised down to the magnetometer noise. Alternating field (AF) demagnetisation was used on a few samples from the SK8 section, after heating to 350°C, but proved ineffective. K_{lf} was monitored after heating stages to monitor mineralogical change. Specimens were kept in mu-metal boxes (residual field <20 nT) between demagnetisation and measurements steps.

In total 28 and 247 paleomagnetic specimens were demagnetised from the Brak and Shabirinah formations respectively. The bedding dips in all these units are zero so a fold test was not possible.

Characteristic remanence (ChRM) directions were isolated using principle component-based statistical procedures implemented in LINEFIND, which uses the measurement variance along with statistical procedures for identifying linear and planar structure in the demagnetisation data (Kent et al., 1983). Both linear trajectory fits and great circle (remagnetisation circle) data were used in defining the paleomagnetic behaviour, guided by objective and qualitative selection of the excess standard deviation parameter (ρ), which governs how closely the model variance, used for analysis, matches the data measurement variance (Kent et al., 1983). The PMagTools (version 4.2) software Hounslow (2006) was used for the analysis of mean directions and virtual geomagnetic poles.

Backfield isothermal remnant magnetisation (IRM) up to 1.75 T was applied to a representative sub-set of specimens, to investigate the magnetic mineralogy. Anhysteretic magnetisations were applied to investigate the granulometry of the iron oxides. Anisotropy of magnetic susceptibility (AMS) (Liu et al., 2001 and references therein) was evaluated on selected specimens from section SK8, to assess grain fabrics and paleoflow information (Supplementary data Fig. S5).

U-Pb isotope reconnaissance by laser ablation ICP mass spectrometry (LA-ICP-MS) and solution-mode U-Th chronology by multicollector ICP mass spectrometry (MC-ICP-MS) was attempted on six samples from the Stromatolite Member in the TS2 and TS3 sections. Sample selection was guided by thin section petrography to screen samples for minimum possible silicate detritus contents. U-Th data were obtained on samples subjected to total dissolution with HF-HNO_3-$HClO_4$. Analytical procedures, including ion exchange chemistry and mass spectrometry followed Douarin et al. (2013), with details given in the Supplementary data. Data were obtained on a Thermo Scientific Neptune Plus MC-ICP-MS and calculation of activity ratios and ages used the decay constants of Cheng et al. (2013).

4. Results

4.1. Magnetic Mineralogy Results

The NRM intensity and magnetic susceptibility (MS) are broadly related to each other (see Supplementary data Fig. S5a), with carbonate-rich samples having weak (sometimes diamagnetic) susceptibilities, and red or mud-rich samples (e.g. in paleosols) having the largest NRM intensity or magnetic susceptibility. Some clustering of these magnetic data into the various lithostratigraphic units, is related in part to the often higher carbonate content of the Brak Formation and Kunayr Member samples, compared to those of the Tmassah Member (Supplementary data Fig. S5a).

Red mudstones and sandstones from the SK3 and TS3 sections, and all non-red samples from the SK8 section do not saturate in IRM fields of 1.75 T, indicating substantial amounts of haematite (or goethite) in these types of samples. Other lithologies in the SK3 and TS3 sections saturate by ca. 1 T, but still have 10–35% of IRM acquisition above 300 mT probably indicating a substantial haematite contribution to the IRM, as well as a more dominant low coercivity phase, possibly magnetite, or Ti-magnetite (Supplementary data Fig. S6). Remanent coercivity of non-red samples from the TS3 section are between 109 and 253 mT, in comparison to non-red samples from other sections, which range between 44 and 98 mT, indicating a substantial difference in the relative contributions of low coercivity (magnetite) and haematite between the southerly (near Tmassah) and northerly sections (Wadi ash Shati to Wadi Kunayr). The large contributions from haematite (or goethite) tally with the ineffective application of AF demagnetisation on the NRM. Early and mid-Miocene clastic and carbonate rocks from the western Desert in Egypt, share similar magnetic properties (Abdeldayem, 1996). The AMS data displays depositional fabrics (Supplementary data Fig. S5b), with Kmax axes showing approximate E-W alignment, generally consistent with the trend of fluvial channels to the east of section SK8. There is also evidence of a weaker lateral transport direction, reflected also in paleocurrent data from the SK7 section (Fig. 7; Supplementary data Fig. S5c).

4.2. Paleomagnetic Results

During demagnetisation specimens generally have stable MS values until ca. 450 °C, when the majority show either a small increase (up to 2 × initial value) or decrease in MS, indicating initiation of some mineralogical alteration (Van Velzen and Zijderveld, 1992). Reddened samples tend to show less change in MS values. In non-red specimens, this alteration sometimes obscured the recovery of the remanence at higher demagnetisation temperatures. Unblocking temperatures of the NRM are generally distributed throughout the

443 demagnetisation range up to ca. 600–650 °C (demagnetisation is often complete by 600–
444 650 °C), with most often more than half of the NRM removed by around 300–450 °C, after
445 which the rate of unblocking decreased. Reddened samples tend to have a more rapid drop
446 in NRM intensity at < 200 °C, possibly suggestive of goethite (or pigmentary haematite;
447 Márton et al., 1980) partly carrying the NRM.
448 Of the 275 specimens measured, some 88% give data that can be confidently
449 interpreted as containing a ChRM component. Low stability components between room
450 temperature and up to 300 to 450 °C, appear to be composed of two groups. Firstly, in 70%
451 of specimens (regardless of if they are interpreted as having reverse or normal polarity) the
452 low stability component is a Brunhes-like magnetisation with mean direction of 002°/42°
453 (Supplementary data Fig. S7). The remainder appear to have a variety of 'mixed directions'
454 somewhat scattered, either northerly directed negative inclination components or southerly
455 directed positive inclination components. These mixed directions are interpreted as
456 composite components, mostly mixes between the Brunhes overprint, and the primary
457 reverse direction, since 68% of them have interpreted reverse polarity (see Supplementary
458 data). Random viscous components also probably contribute to the large scatter in these low
459 stability components. Intermediate stability components seem to be entirely random
460 (Supplementary data Fig. S7).
461 High stability components inferred to be the ChRM are difficult to extract from most
462 specimens, with only 25% of the specimens giving suitable line-fits to the demagnetisation
463 data (here called S-class data). These are largely at demagnetisation temperatures
464 beginning around 350 to 400 °C, either to the origin or until around 600 °C (Fig. 11A, E).
465 Often above 600 °C, the directional scatter is large, or the specimen demagnetised. The
466 remaining, 75% of specimens display greater circle trends towards interpreted normal or
467 reverse polarity (here called T-class data, Fig. 11B–D, F). The low to moderate success rate
468 in obtaining line-fits may reflect the often sandy, well sorted, silt and clay-poor nature of most
469 samples; as such sediments tend to be rather poor paleomagnetic field recorders. Silt-rich or
470 reddened lithologies generally display the best paleomagnetic behaviour, but are few in
471 number. The 75% of specimens with great circle trends reflects the difficulty in isolating the
472 ChRM from the low and intermediate stability components during demagnetisation (e.g. Fig.
473 11F).

474 ***4.2.1. Mean Directions and Paleopoles***
475
476 Mean directions were determined using specimen-based means, by combining the
477 great circle paths with those specimens with line-fit ChRM (Table 2), to produce combined
478 means using the method of McFadden and McElhinny (1988). This method determines a
479 mean direction, by including the 'fixed-point' ChRM directions, and those points on the
480 projected great circles, which maximise the resultant length (i.e. in effect those calculated

481 points on the great circle which are closest to the combined mean direction). The great-circle
482 combined means pass the reversal test for the TS3 and SK3 sections, but marginally fail for
483 the SK8 section, with <10^{o} between antipodal directions (Table 2).
484
485

Section [code]	Mean Dec/Inc	α95	$N_T/N_l/N_p$	Reversal Test [γ_o;γ_c]	VGP Pole Long./Lat.	D_p/D_m
SK8 [AP]	3.5/42.1	3.1	134/32/72	R- [7.7;6.5]	146/86	2.3/3.8
TS3 [TM]	1.1/42.9	3.8	95/19/58	Rb [1.6;7.6]	153/88	2.9/4.7
SK3 [BC]	1.2/45.2	5.7	46/9/20	Rc [9.0;12.7]	298/89	4.5/7.2

486 Table 2. Mean paleomagnetic directions for the three sections. Code=sample code. α95= Fisher 95%
487 cone of confidence. N_T=Total specimens measured, N_l=Number of specimens with line-fits,
488 N_p=Number of specimens with great circle fits. For the reversal test (McFadden and McElhinny,
489 1990), γ_o=observed angle; γ_c=critical angle. Virtual geomagnetic pole (VGP) is the normal pole.
490

491 The confidence intervals on our paleopoles overlap with the apparent polar wander
492 path (APWP) for the 0–30 Ma interval for Africa (Torsvik et al., 2012), showing the reliability
493 of the mean directions (Supplementary data Fig. S8). The limited number of Miocene to
494 recent age poles from Africa, tend to show a general displacement to the east of the APWP,
495 whereas the poles from the Jabal as Sawda volcanic rocks tend to have lower latitudes, due
496 to shallower mean inclinations than our data. This discrepancy is not due to inclination
497 shallowing in our sediment sections, which if corrected for tends to move the poles
498 northwards to steeper poles (see Supplementary data Fig. S8).
499

500 ***4.2.2. Magnetostratigraphic Interpretation***
501

502 The line-fit ChRM directions from the sections were converted to virtual geomagnetic
503 pole (VGP) latitude (Opdyke and Channell, 1996) using the great circle ChRM means in
504 Table 2 (Fig. 12). For those specimens that had no line-fit, the point on their great circle
505 nearest this mean, was used for calculating the VGP latitude. All specimens were also
506 assigned a 'polarity quality' based on the quality of demagnetisation behaviour and, if from
507 T-class specimens, the length and end-position of the great circle trend (similar to the
508 procedures used by Ogg and Steiner, 1991; Hounslow and McIntosh, 2003). One specimen
509 of good-quality polarity (i.e. S-Type) was sufficient to define the horizon polarity, whereas
510 with specimens of poorer quality at least two are required (Fig. 12). Some 11% of all
511 specimens failed to yield data which could be used to determine specimen polarity, but no
512 horizons failed to yield specimens which could be reliably used to determine magnetic
513 polarity (Fig. 12).

The SK8 and TS3 sections can be correlated together using the base of the Kunayr Member, where the underlying upper part of the Tmassah Member is reverse polarity dominated. The youngest parts of the Shabirinah Formation in all three sampled sections have dominantly normal polarity, which allows us to construct a composite magnetostratigraphy using the three sections (Fig. 13). The composite magnetostratigraphy is generated using the numerical optimisation techniques described in Hounslow (2016). For this data, the optimisation shifts the SK3 section (without a metre-scale change), but has both a shift and a scale change for the data in the TS3 section. The optimised composites are in the metre- scale of the SK8 section, whose data remain unscaled.

From the TS2 and TS3 section logs and field evidence it is clear that at least ca. 3 m of red mudstones is missing from the upper part of the Stromatolite Member at sampled section TS3 (Fig. 6 ; Fig. 10). This is due to down-cutting of the channel sandstone in the base of the Tmassah Member at section TS3. We therefore break the TS3 section into two sub-divisions, with the youngest normal polarity sample in the Tmassah Member correlating to the base of the normal polarity interval at SK8 with its lower boundary at 11.4 m (Fig. 13). This broadly correlates the red-black (humid) paleosols seen in the SK8 section with the fluvial lower part of the Tmassah Member at section TS3 (Fig. 10; Fig. 13). A slightly lower position of the Stromatolite Member at TS3 was considered, which correlated the interval of red mudstones in the TS3 and SK8 sections (Fig. 10). This gave a projected missing thickness for the upper part of the Stromatolite Member of 9.7 m, which appears too large based on the field evidence, so was rejected as a possibility.

We derive two likely composite magnetostratigraphies (Fig. 13), because of ambiguity in how to correlate the SK3 section to the upper parts of the SK8 and TS3 sections. The differences between composites A and B relate to the position of the SK3 section, which is correlated to a younger magnetozone in the TS3 section in the composite B (Fig. 13). Composite-B better correlates the sandstone bed in the uppermost part of the TS3 section with the clastic interval (with red mudstones) at section SK3. Composites A and B both give a projected missing 2.9 m and 2.5 m of section respectively, from the top of the Stromatolite Member at TS3, similar to the estimated amount based on field data and nearby sections such as TS2 (Fig. 10). Normal polarity magnetozone Sb6r.1n (normal sub-magnetozone in Sb6r) was not detected at section TS3, which may relate to a potentially missing part in section TS3, due to some uncertainty in exactly how to correlate sampled sub-sections in the field, which join at this level.

4.3. U-Pb and U-Th chronology results

The samples from the TS3 section have U contents of ca. 1–1.5 ppm while the samples from the TS2 section have a wider range of U contents from 0.5 to ca. 5.4 ppm.

Both groups of samples have variable and significant amounts of Th with resultant low $^{230}Th/^{232}Th$ activity ratios ([$^{230}Th/^{232}Th$]) ranging from ca.1 to 18 (Supplementary data Table S2). Detritus-corrected age uncertainties are large and significantly limit the utility of the dataset. Nevertheless, the data are sufficient to indicate that most of the carbonates analysed are at or close to U-Th secular equilibrium, and are thus > ca. 500 ka old (Supplementary data Table S2, Fig. S9). The exception, and only apparently 'reliable' date obtained, was sample TM6 at 242 ± 24 ka. Given that this date is not in stratigraphic order and there is evidence of a much older age from other chronometers, it is interpreted as reflecting a post-depositional disturbance of the carbonate mineralogy. In oxidizing environments uranium is very mobile and recrystallisation or major disturbance of the carbonate at any time can cause uranium to be redistributed. This is clearly an issue with these sediments, since oxidizing sediment systems are the norm. One other sample nominally records a < 500 ka age, but as [$^{230}Th/^{232}Th$] is ca. 1.3, the calculated age is strongly controlled by the assumed initial Th isotope composition and is therefore not interpreted here. Overall, the data obtained indicate these carbonates are unsuitable for U-Th or U-Pb chronology (see Supplementary data for further discussion).

5. Discussion

5.1. Other chronological controls

The basalt fragments in the basal Brak Formation in Wadi ash Shati, and basalt flows inferred in the basal Brak Formation in mapped outcrops to the north of Wadi Kunayr (Fig. 8), are probably derived from the Jabal as Sawda lava field to the north (but may be from the older al Hasawinah lava fields). The Jabal as Sawda lavas are dated to 12.3–10.5 Ma (Ade-Hall et al., 1975 ; Liégeois et al., 2005) using the K/Ar method. This implies the Brak Formation is younger than ca. 12–10 Ma, and the Shabirinah Formation is older than this.

The SE and E flowing paleocurrents in the Tmassah Member, indicate the formation pre-dates the bulk of the Haruj al Aswad volcanic field, otherwise the volcanic field would have been an effective barrier to eastwards fluvial transfer into the Sirte Basin. The Haruj al Aswad volcanic field, has mean K/Ar ages of 2.8 ± 2.0 Ma (range 8.1 ± 0.11 Ma to 0.5 ± 0.1 Ma; Cvetković et al., 2010 ; Bardintzeff et al., 2012; uncertainty as 1 SD), indicating the Tmassah Member is older than ca. 8 Ma. However, both Cvetković et al. (2010) and Drake et al. (2008) report outlier K/Ar dates of 11.8 ± 0.4 Ma and 10.2 ± 1.3 Ma respectively, so minor earlier phases of the Haruj al Aswad seem possible. This is consistent with radiometric dating from the Jabal Eghei volcanic centre, illustrating the long-lived nature of the Libyan volcanic centres (Radivojević et al., 2015). It is not clear if these minor early phases of the Haruj al Aswad volcanic field could have blocked fluvial access into the Sirte Basin.

590 Hence, together the volcanic field radiometric dating, and stratigraphic relationships
591 indicate the Shabirinah Formation is older than about 11–8 Ma, with the Brak Formation
592 younger than 10–12 Ma, placing these formations in the Miocene to Pliocene.
593 Between the Brunhes chron until the mid-Oligocene (chron C11) the mean duration
594 between geomagnetic field reversals was 0.248 Ma (Lowrie and Kent, 2004). Since we have
595 33 to 37 magnetozones in our two composites, this implies the minimum duration of our
596 composite magnetostratigraphy is of the order of 8–9 Ma, so the oldest parts of the
597 Shabirinah Formation likely range down to 19–16 Ma, as a minimum age estimate (ca. 20
598 Ma as an older estimate). However, it is unlikely our sampling of this 55–60 m succession
599 has detected every magnetochron, since using these duration estimates and the average
600 sample spacing (ca. 1 sample per 0.75 m) indicates a mean duration between sampling
601 levels of ca. 70 kyrs, indicating that chrons < ca. 40 kyrs are unlikely to have been detected.
602 This suggests the age duration of our composites may be closer to ca. 9 Ma, and the age of
603 the oldest parts of the Shabirinah Formation to lie between 20 and 17 Ma.
604 Geyh and Thiedig (2008) have dated the Brak Formation and the Bir az Zallaf Member
605 using the 230Th/U method. The Brak Formation gives a median age of 353 ± 31 ka (1 SD)
606 while the Bir az Zallaf Member has a median age of 223 ± 26 ka (excluding open system
607 samples). These ^{230}Th/U dates seem highly implausible, based on the stratigraphic
608 relationships in Wadi ash Shati, since a major unconformity, followed by ca. 90 m of erosion
609 (Fig. 9), with a subsequent ca. 30 m of clastic sediment deposition of the Sifar and Sayl
610 members, separate the Brak Formation and Bir az Zallaf Member, with an apparent ca.130
611 ka age difference.
612 In the Sarir al Qattusah, west of the Haruj al Aswad (Fig. 1) Schlüter et al. (2002)
613 estimate an erosion rate on carbonate dominated hamada surfaces of 1–2 m/Ma. In the
614 hyperarid (1–10 mm/year of rainfall), low elevation parts of the Atacama Desert, cosmogenic
615 isotope determined erosion rates of bedrock are 0.4 to 10 m/Ma (Fujioka and Chappell,
616 2011). In the Namib Desert erosion rates of sediment basins are of the order of 5–16 m/Ma,
617 higher than bed rock erosion rates (3–5 m/Ma) in the same region, and both are consistent
618 with fission track estimates (Fujioka and Chappell, 2011). Using the maximum of these
619 desert erosion rate estimates suggests the ca. 90 m of erosion in Wadi ash Shati took at
620 least ca. 5 Ma to produce rather than the ca. 130 ka suggested by 230Th/U dating.
621 Hence, the ^{230}Th/U dates are grossly out of step with both the regional stratigraphic
622 relationships of these units, our magnetostratigraphy and likely erosion rates, which instead
623 suggest a 130 ka time difference, should occupy around 1.5 m in our sediment successions.
624 However, like our attempted U-Th dating, the ^{230}Th/U dates themselves likely relate to late
625 Pleistocene surface weathering, with groundwater mobilisation of uranium prior to deposition
626 of the earliest parts of the Shati Formation (i.e. the Aqar Member), starting at around 100–
627 136 ka. The consistent positive relationship between elevation and age (and negative

between relationship between inferred age and $\delta^{13}O$) in the $^{230}Th/U$ dates (Geyh and Thiedig, 2008) may relate to the characteristics of the groundwater modification process, with the U-system fixed-in slightly earlier at higher elevation sites. Intervals of Quaternary pluvial mobilisation of U are also known from the Egyptian deserts between 240 and 80 ka (Osmond and Dabous, 2004).

5.2. Magnetostratigraphic age model

Without firm age tie points for the magnetostratigraphy, we use quantitative correlation methods to correlate to the geomagnetic polarity timescale (GPTS) to date objectively these successions. Three main methods have been previously used. Firstly, cross-correlation using either magnetozone lengths, L_i (and GPTS chron durations; Lowrie and Alvarez, 1984), or loge of the ratio (r_i) of lengths of the underlying magnetozone (i.e. $r_i = L_i/L_{i-1}$, with L in metres or Ma duration for the GPTS; Man, 2008). Secondly, a likelihood-based method linked to a stochastic model of sediment deposition (Man, 2011). Both of these methods are limited by the necessity for a complete recording of all GPTS polarity chrons in the section, which is a problem with our data. The method of Man (2011) is also restricted to a limited number of section magnetozones (8 to 12) due to adherence to a single stochastic sedimentation model. Thirdly, the dynamic time warping method, proposed by Lallier et al. (2013), using r_i values but incorporating potentially missing magnetozones in sections, by considering correlations which minimise the local variation of the accumulation rate.

In all these methods, converting magnetozone height to r_i in effect transforms the GPTS and section data into a consistent dimensionless scale, and reduces the impact of changes in sedimentation rate. However, it does impose non-linear noise on r_i, since shorter magnetozones have the least well-defined heights in the section (due to sample spacing issues), so the intervals with the least uncertainty in r_i are those with r_i ca. 1, and longer magnetozone lengths. Lallier et al. (2013) used a correction factor to account for the biased uncertainty in r_i.

However, in essence all these methods utilise only one characteristic (magnetozone height, or r_i) of the polarity pattern, when the character of the GPTS may be better expressed by multiple parameters which express characteristics like polarity bias around the chron, or relative durations of more than two adjacent chrons (Olson et al., 2014). The advantage of utilising characteristics from the adjacent magnetozones, is some smoothing of the response function to limit impacts of magnetozone thickness uncertainty.

We use the sequence slotting method (Clark, 1985; Gordon et al., 1988 ; Thompson and Clark, 1989), as implemented in the CPLSlot programme (Hounslow and Clark, 2016), an objective method of quantitative correlation that can deal with multivariate datasets (See Supplementary data). The method seeks a correlation which minimises the dissimilarity (defined by a distance metric) between the two aligned datasets. Sequence slotting is not constrained to

have sequential matching of data points across matched successions (e.g. as in cross correlation), so can deal with missing chrons in the GPTS, and variable sedimentation rates. We parameterise each magnetozone with its polarity (− 1, or + 1), duration (in Ma), $Log_e(r_i)$, polarity bias (including the two adjacent chrons), and Sherman's ω_2 statistic (using the two adjacent chrons). ω_2 measures the deviation of magnetozone lengths as a proportion of the average length (Olson et al., 2014). The durations of magnetozones in the polarity composites were estimated using section durations based on reversal rates of 0.259 Ma^{-1}, which is the median rate for the last 29 Ma, if chrons < 40 ka are excluded from the GPTS of Ogg (2012). All 5 chron parameters also then approximately fall in the numerical range − 2 to + 2, which allows no parameter scaling to be used in the sequence slotting. A Euclidean distance metric was used (Gary et al., 2005). A blocking constraint of 2 (Thompson and Clark, 1989) was used which limits missing chrons in the GPTS to one subchron normal-reverse polarity pair.

The goodness-of-match of the sequence slotting is evaluated in two ways. Firstly, from the conventional slotting parameters, particularly the Δ parameter, which takes values from >0 to ~1 (Δ <~0.5 indicates very good similarity; Thompson and Clark, 1989). Secondly, matrix association coefficients (R_c, RV_2 and standardized RV) which evaluate the similarity of the whole configuration of variables between the two datasets (Smilde et al., 2009; Abdi, 2010). The weakness of the Δ parameter is that it is most strongly impacted by data variability proximal to the levels considered, so quite different correlation solutions can give similar Δ, so using Δ alone can be misleading. Δ tends to indicate the goodness of the 'local-match' in a simple sense. In contrast, the R_c, RV_2 and standardized RV (matrix association coefficients) tend to respond better to longer-scale structure in the data, are less impacted by local noise, and tend to respond closer to visual similarity when data are plotted side by side. Likely solutions can also be imaged by the H-matrix (Gordon et al. 1988), which is a visual representation of the matching similarity of the two data successions are as they are slid past each other (the concept is similar to the similarity matrix of Gary et al., 2005). See the Supplementary Data for further details.

Testing composite-A indicates there are two likely match solutions, one which places the upper part of the composite polarity in the Tortonian (top SB10n.2n=C3Br.2n; base SB1r=C5Cn.2r), and one which places it in the Serravallian (top SB10n.2n=C5An.1n; base SB1r=C6Br, Supplementary Data Fig. S9). The one with the larger matrix association coefficients is the Serravallian solution, whereas the slotting parameter Δ is similar for both age models. Composite-B indicates, like composite-A, that the two most likely solutions place the upper part of the polarity composite in the Tortonian (SB10n.2n=C3Br.2n; SB1r=C5Cn.2r) and Serravallian (SB10n.2n=C5An.1n; SB1r=C6Br). Like composite-A the Serravallian solution has the larger matrix association coefficients, with the Δ parameter similar for both age models. The Serravalian composite-B solution also has lower Δ and larger matrix association coefficients compared to the Serravallian Composite-A solution (Supplementary Data Figs. S10, S11) and is the final preferred solution (Fig. 13). This places

706 the base of the Brak Formation at ~13 Ma, a little bit older than inferred by the supposedly
707 interbedded Jabal as Sawda lava's. It could be the case, the inferred interbedded basalts
708 occur slightly higher in the Brak succession north of Wadi Kunayr. At section SK3 the Brak
709 Formation ranges up into chron C5An.1n of age 12.0 to 12.2 Ma, similar to the oldest Ar/K
710 dates from the Jabal as Sawda lavas. Hence, it is probable the Brak Formation continues to
711 younger ages than those seen in section SK3, as inferred by its presence at higher
712 elevations (Fig. 7).
713 The accumulation rates are broadly similar through the Tmassah Member to Brak
714 Formation, but decline markedly through the Stromatolite Member (Supplementary Data Fig.
715 S11). This may relate to a regional hiatus (missing interval) at the base of the Tmassah
716 Member, since the composite polarity does not appear to capture the dominant reverse
717 polarity well through chrons C6Ar and C6AA. Alternatively, it may relate to a shut-down in
718 coarse clastic supply in the Stromatolite Member, which is dominated by micritic carbonates
719 and mudstones.
720

721 ***5.3. Implications***
722

723 It is clear the lacustrine humid intervals associated with Al Mahruqah Group are not
724 only found in the late Quaternary Shati Formation, but also occur in the early and mid-
725 Miocene. Three lacustrine-palustrine phases are present in the Shabirinah and Brak
726 formations that suggest episodes of greater humidity when Lake Megafezzan developed.
727 These are separated by clastic sediments and paleosols deposited in less humid intervals in
728 which we have no direct evidence for lake deposits. The first of these intervals of greater
729 humidity is during the late Aquitanian and is represented by the limestone bed in the
730 Stromatolite Member, which is most widespread in the region east and north of Tmassah, to
731 within 45 km south of Wadi Kunayr. Since in the Wadi ash Shabirinah area the lower parts of
732 the Shabirinah Formation are dominated by fluvial clastics furthest to the east, it implies we
733 are dealing with fluvial fringes to a large lake, located further west, which is dominated by
734 fine-grained red clastics and stromatolitic limestones. In the Wadi ash Shabirinah area in
735 spite of dominant cross-bedding directions to the SE (Fig. 6), some clastic material was also
736 supplied from the NNE, since the units pinch out in this direction. We also have evidence of
737 proximal channels supplying material southwards (section TS7, Fig. 6). These imply the
738 paleotopography during this interval was a valley-like fluvial transport system (with some
739 lateral supply), likely flowing eastwards through a low in the Paleozoic basement ridge north
740 of Dur al Qussah into the Abu Tumayan Trough (Fig. 1). A similar situation may have existed
741 in the Wadi Kunayr area, where a secondary mode in the AMS Kmax axes, and some
742 paleocurrent data suggest lateral flow (Supplementary data Fig. S5c).

743 The part of the Shabirinah Formation below the Kunayr Member equates in time to
744 Aquitanian-Burdigalian fluvial (or part fluvial) units seen in the Sirte Basin (Qarat Janannam
745 Member). Equivalent age units in the Egyptian western Desert are the Al Moghra Formation
746 and the Messiouta and Sehib formations in Tunisia (Fig. 14). Dating of these other North
747 African fluvial or estuarine (Hassan, 2013) units is either by lithostratigraphic correlation in
748 Tunisia (Mannaï-Tayech, 2009) or their vertebrate faunas (Fig. 14). The vertebrates in these
749 Aquitanian-Burdigalian deposits in Egypt and Libya are large vertebrates such a
750 hippopotamus and land carnivores together with micro-vertebrate remains, such as rodents
751 (Morlo et al., 2007) along with fossilised tree logs and fish (Cook et al., 2010). Vertebrates
752 from the Marada Formation in Libya are diverse and include large land and water mammals
753 and reptiles together with small vertebrates such as rodents, bats and rabbits/hares
754 (Wessels et al., 2003 ; Llinás-Agrasar, 2004).These together indicate the tropical and
755 savanna climatic conditions along the Tunisian-Libyan- Egyptian coastline during the
756 Aquitanian-Burdigalian.
757 The second palustrine interval is found in the lower part of the Kunayr Member,
758 restricted so far to the area east of Tmassah. It dates to the latest Burdigalian (chron C5Cn)
759 through into the early Langhian. These limestones laterally grade north-eastwards and
760 eastwards into interbedded calcreted clastic units. Such lateral relationships follow the model
761 outlined by Alonso-Zarza (2003) for palustrine-calcrete units in semi-arid settings, indicating
762 that the central part of the Kunayr Member paleolake basin was to the west or SW of the
763 current outcrops, a region where the deepest part of the southern sub-basin of the Fezzan
764 topographic low is found today (Drake et al., 2008). Compared to the underlying Tmassah,
765 Stromatolite and Maharshim members calcretisation and pedogenically modified clastics and
766 palustrine limestones are significant components of the Kunayr Member. Calcrete occurs in
767 regions that experience an annual soil moisture deficit, either from a low annual rainfall or
768 sub-humid regions characterised by a pronounced dry season (Candy et al., 2004). The
769 chron interval C5Cn to C5AC corresponds with the higher temperatures of the mid-Miocene
770 Climatic Optimum, covering most of the Langhian (Hilgen et al., 2012). Therefore, the
771 calcretisation in the Kunayr Member is likely a response to the increased moisture deficit
772 stimulated by the higher temperatures.
773 The age of the base of the Kunayr Member is closely aligned in time with the
774 transgressive base of the marine Ar Rahlah Member (of the Marada Formation in the Sirte
775 Basin) and the marine Marmarica Formation of the Egyptian Western Desert (Fig. 14).
776 These southward marine incursions in the North African margin seem to record the higher
777 global eustatic sea-levels starting in the late Burdigalian (Chron C5C) and ending before
778 Chron C5AB (Hilgen et al., 2012). Similar aged marine transgressive units are seen in
779 central Tunisia dated to foraminifera zones N7 to N10 (Chrons C5C to C5AC; Fig. 14;
780 Mannaï-Tayech, 2009). In the Fezzan Basin, this closer proximity to the sea perhaps drove

781 the climate to be less seasonal suggesting the higher temperatures of the mid-Miocene
782 climatic optimum, were the primary reason driving soil moisture deficits and calcretisation in
783 the Kunayr Member.
784 The main palustrine phase of the Fezzan Basin Miocene is represented by the
785 deposition of the Brak Formation during the Serravallian. This limestone may represent the
786 most extensive palustrine deposit in the Fezzan basin, since it oversteps onto basement
787 highs and eastern fringes of the Fezzan Basin, along the foot of the Sarir al Quttasah
788 Paleogene escarpment. Although we have no direct evidence about the nature of the basin-
789 centre equivalent of the Brak Formation, it is assumed to be a more open lacustrine version
790 of the palustrine limestone unit (or a mudstone unit) we see at basin margins. One of the
791 reasons the Brak Formation may be so extensive is that the exits from the Fezzan into the
792 Sirte Basin were restricted by initial growth of the Jabal as Sawda volcanic centre (restricting
793 the NE Wadi Nashu exit?; Fig. 1) and uplift of the western side of the Sirte Basin, thus
794 allowing a larger lake to develop.
795 The best-dated evidence we have for other Serravallian terrestrial sediments in
796 countries adjacent to Libya, is from Tunisia, where the Beglia Formation forms a NE
797 prograding succession above marine and non-marine strata in central and SW Tunisia (Fig.
798 14; Mannaï-Tayech and Otero, 2005). A humid terrestrial climate in North Africa during the
799 Serravallian is indicated by fossil crocodiles and a variety of other large land vertebrates
800 from the Beglia Formation (Serravallian – Tortonian in age; Pickford, 2000 ; Mannaï-Tayech,
801 2009), which are associated with a large NE flowing river system exiting from the Algerian-
802 Tunisian central Sahara (Mannaï-Tayech and Otero, 2005). A larger regional assessment by
803 Swezey (2009) suggested the central Saharan Miocene strata were deposited by fluvial
804 systems that reached a maximum extent during the Langhian–Serravallian. The Brak
805 Formation therefore may be expression of this maximum extent of fluvial-related units in the
806 central Sahara, of which the Beglia Formation may also be an expression.
807 The uplift of the southwestern shoulder of the Sirte Basin continued after the Brak
808 Formation, since clearly in both the Wadi ash Shati and Wadi ash Shabirinah regions the
809 units are tilted to the west (or their eastern parts are up-faulted; Fig. 6 ; Fig. 7). The extent of
810 the Shabirinah and Brak formations to the west is unclear, we only have glimpses of these
811 units in the Northern Awbari Sand Sea, it may be lateral equivalents exist beneath the
812 Murzuq and Awbari Sand seas.
813 Preliminary magnetostratigraphic results from the upper part of the overlying Zarzur
814 Formation suggest it may be mid Pliocene (ca. 3 Ma) in age (Drake et al., 2011b), and our
815 results indicate the younger part of the Brak Formation is at least 12 Ma (or younger). This
816 suggests the erosion event and unconformity between these two formations likely started
817 during the late Miocene. Late Miocene unconformities are recognised throughout the Sirte
818 Basin and have been used as a correlation datums for the top of the Marada and Al Khoms

819 formations (Selley, 1968; El-Hawat, 1980 ; El-Hawat, 2008; Fig. 14) and their equivalents in
820 western Egypt (Gerdes et al., 2010 ; Zaki et al., 2013). El-Hawat and Salem (1987) also
821 used the unconformity on the top of the Marada Formation to divide the Miocene stratigraphy
822 in northern Cyrenaica (NE Libya) into Middle and Upper Miocene units (Fig. 14). The earlier
823 event probably relates to an interval of karst development on the Marmarica Formation in the
824 Egyptian Western Desert, which is dated to mammal zone MN9 (ca. 10–11 Ma) in the early
825 Tortonian (Wanas et al., 2009 ; Zaki et al., 2013). These circum-Mediterranean and North
826 African events are associated with Mediterranean tectonic reorganisation and eustatic lows
827 in global and Mediterranean sea level during the Tortonian-Messinian (Gerdes et al., 2010 ;
828 Hilgen et al., 2012).
829 Evidence for the geometry of the fluvial transport systems in the Shabirinah Formation,
830 suggest axial-drainage networks. This is clearly seen in Wadi Kunayr, where the Shabirinah
831 Formation occupies a linear topographic depression (ca. 50 m deep over ca. 20 km distance;
832 Fig. 1 ; Fig. 8) in the Mesozoic and Paleozoic basement. Such an axial system is also
833 inferred in the Wadi ash Shabirinah region, where we have a ca. 50 m basement elevation
834 difference over some ca. 9 km normal to the axial transport. Thus, the Fezzan Basin axial
835 transport systems must be older than the Aquitanian, suggesting that the major drainage
836 systems of the central Sahara were inherited from networks that initially developed over 23
837 Ma ago, during the Oligocene.
838 The new evidence of the age of these units shows that the Shabirinah and Brak
839 formations are comparable in age to the Marada Formation of the Sirte Basin, which ranges
840 between Aquitanian and Serravallian in age (Mastera, 1985 ; El-Hawat and Pawellek, 2004;
841 Fig. 14). In its type area in the eastern Sirte Basin, the Marada Formation is composed of a
842 lower fluvial clastic unit, the Qarat Jahannam Member of Aquitanian to Burdigalian age
843 (Wessels et al., 2003). This is overlain by a diachronous marine carbonate-clastic unit, the
844 Ar Rahlah Member of Langhian–Serravallian age (El-Hawat and Pawellek, 2004; Fig. 4 ;
845 Fig. 14). Similar aged fluvial successions dominate in the western Sirte Basin in the Hun
846 Graben and Zallah Trough, laterally transitional to marine units to the NE. Although the
847 dating evidence (mammal fossils for the early-mid-Miocene; Wessels et al., 2003) for the
848 Marada Formation may not be quite as precise as the magnetostratigraphy from the
849 Shabirinah- Brak formations, the upwards transition to carbonate-clastic units in the Kunayr
850 Member appear to be synchronous with those of the Ar Rahlah Member of the Marada
851 Formation. This evidence, plus the paleocurrent data from the Shabirinah Formation
852 suggests that these units were connected across what is now the Al Haruj al Aswad volcanic
853 fields, which became active later as the Sirte Basin was tilted north-westwards (Abdunaser
854 and McCaffrey, 2015).
855

6 6. Conclusions

We provide the first detailed assessment of the lithostratigraphy of the Lake Megafezzan sediments, as represented by the Al Mahruqah Group, dividing them into three unconformity-bound packages. The oldest of these packages, the Shabirinah and Brak formations are a succession of lacustrine and fluvial units locally with humid paleosols in its lower parts, which progressively show evidence of semi-arid paleosol development up through the succession, culminating in the palustrine limestone unit represented by the Brak Formation.

Paleomagnetic data from 124 samples, demonstrate the Shabirinah and Brak formations hold a magnetic polarity stratigraphy, which is carried by a combination of magnetite and haematite. The mean directions obtained concur with the expected paleopoles position for Africa in the Miocene to recent interval. A composite polarity succession has 10 major reverse and normal polarity magnetozone couplets, estimated to span ca. 9 Ma. Sequence slotting methods are used to quantitatively correlate the magnetozone composite to the geomagnetic polarity timescale, demonstrating that these formations are lower to mid-Miocene in age, 12 to 23 Ma older than previously implied by 230Th/U dating. The new dating broadly confers with Ar/K dates from the Jabal as Sawda lavas, which are probably interbedded with the sediment succession around the lower to mid parts of the Brak Formation. Attempts at Th/U dating of these successions are strongly impacted by mid and late Pleistocene U-mobility in ground water, and do not reflect sediment deposition ages.

Three main phases of lacustrine limestones developed. During the late Aquitanian a widespread stromatolitic lake developed in the SE Fezzan, which passes laterally into basin margin fluvial clastic units. During the late Burdigalian palustrine carbonate units typically pass laterally into mixed clastic to more calcretised palustrine units which characterise basin margin situations. The Serravallian age Brak Formation, a palustrine unit is a highstand deposit showing the maximum likely extent and elevation of lake levels in a more extensive Fezzan Basin, although its basin centre lateral equivalent, is not seen. These formations largely developed prior to the development of the volcanic centres in the western fringes of the Sirte Basin, and suggest the major drainage networks of the Libyan Sahara developed prior to 23 Ma in the Oligocene. Increasing paleosol modification of the lake carbonates develop upwards through these successions and are the response to increasing soil-moisture deficits. The increasing prevalence of lacustrine limestones may be due to the development of a larger topographic basin in the Fezzan with the initial growth of the Jabal as Sawda volcanic centre and associated uplift of the SW shoulder of the Sirte Basin, progressively restricting water into the Fezzan basin. Alternatively, the maximum Serravallian expansion may relate to maximum development of fluvial systems across the

whole central Sahara during the mid-Miocene. These results show the hyper-aridity of the central Sahara must have developed after about 11 Ma.

Acknowledgements

Field work logistics would not have been possible without Toby Savage and Kevin White. Support was from Repsol/REMSA and David Mattingly's field teams (supported from the Society for Libyan Studies Desert Migrations Project) along with logistic and financial support provided by the University of Benghazi Research Centre. The Libyan Dept of Antiquities assisted with desert permits. Some paleomagnetic data was measured by Matt Riding, but most was obtained by HEW during a self-funded PhD. NIGL colleagues Nick Roberts, Neil Boulton and Diana Sahy assisted with the U-Pb and U-Th work which was funded by NIGL project IP-1180-0510 to Sue McLaren.

References

Abdeleldayem, A.L., 1996. Palaeomagnetism of some Miocene rocks, Qattara depression, Western Desert, Egypt. J. Afr. Earth Sci., 22, 525-533.

Abdi, H., 2010. Congruence: Congruence coefficient, RV -coefficient, and Mantel coefficient. In: Salkind, N. (Ed.), Encyclopaedia of Research Design. Thousand Oaks, CA, Sage, pp. 223-230.

Abdullah, M., 2010. Petrography and Facies of the Al- Mahruqah Formation in the Murzuq Basin, SW Libya. (PhD thesis), Universität Hamburg.

Abdunaser, K. M., McCaffrey, K. J., 2015. Tectonic history and structural development of the Zallah-Dur al Abd Sub-basin, western Sirt Basin, Libya. Journal of Structural Geology 73, 33-48.

Abouessa A., Pelletier J., Duringer P., Schuster M., Schaeffer P., Métais E., Benammi M., Salem M., Hlal O., Brunet M., Jaeger J-J., Rubino J-L., 2012. New insight into the sedimentology and stratigraphy of the Dur At Talah tidal-fluvial transition sequence (Eocene–Oligocene, Sirt Basin, Libya). Journal of African Earth Sciences 65, 72–90.

Ade-Hall, J.M., Reynolds, P.H., Dagley, P., Mussett, A.E., Hubbard, T.P., 1975. Geophysical studies of North African Cenozoic volcanic areas: II. Jebel Soda, Libya. Canadian Journal of Earth Sciences 12, 1257–1263.

Alonso-Zarza, A. M., 2003. Palaeoenvironmental significance of palustrine carbonates and calcretes in the geological record. Earth-Science Reviews, 60, 261-298.

Armitage, S.J., Drake, N.A., Stokes, S., El-Hawat, A., Salem, M.J., White, K., Turner, P., McLaren, S.J., 2007 Multiple phases of North African humidity recorded in lacustrine sediments from the Fezzan Basin, Libyan Sahara. Quaternary Geochronology 2, 181–186.

Bardintzeff, J. M., Deniel, C., Guillou, H., Platevoet, B., Télouk, P., Oun, K. M., 2012. Miocene to recent alkaline volcanism between Al Haruj and Waw an Namous (southern Libya). International Journal of Earth Sciences, 101, 1047-1063.

934 Benammi, M., and Jaeger, J.J., 2001. Magnetostratigraphy and palaeontology of the
935 continental Middle Miocene of the Aït Kandoula Basin, Morocco. Journal of African
936 Earth Science, 33, 335-348.

937 Berendeyev, N.S., 1985. Geological map of Libya 1:250,000, Sheet: Hamadat Tanghirt (NH
938 32-16) Explanatory Booklet. Industrial Research Centre, Tripoli.

939 Beyer, C., 2008. Establishment of a chronostratigraphical framework for the As Sahabi
940 sequence in NE Libya. In: N.T. Boaz, A. El-Arnauti, P. Pavlakis, M.J. Salem (Eds.),
941 Circum-Mediterranean Geology and Biotic Evolution of the Neogene Period: The
942 Perspectives from Libya. Garyounis University Scientific Bulletin, Special Issue No. 5,
943 p. 59–69.

944 Blondel, T.J.A., Gorin, G.E., Jan Du Chene, R. 1993. Sequence stratigraphy in coastal
945 environments: sedimentology and palynofacies of the Miocene in central Tunisia. In:
946 H.W. Posamentier, C.P. Summerhayes, B.U. Haq, G.P. Allen (Eds.), Sequence
947 Stratigraphy and Facies Associations. Special Publication of the International
948 Association of Sedimentologists vol. 18, Blackwell Publishing, Oxford (1993), p. 161–
949 179.

950 Boaz, N.T., El-Arnauti, A., Agustí, J., Bernor, R.L., Pavlakis, P. and Rook, L., 2008.
951 Temporal, lithostratigraphic, and biochronologic setting of the Sahabi Formation, North-
952 Central Libya. In: M.J. Salem (Ed.), Geology of East Libya: Third Symposium on the
953 Sedimentary Basins of Libya Vol. 3, Earth Science Society of Libya, Tripoli, p. 959–
954 972.

955 Bradshaw, C. D., Lunt, D. J. Flecker, R. Salzmann, U., Pound, M. J., Haywood, A. M.,
956 Eronen, J. T., 2012. The relative roles of CO_2 and paleogeography in determining Late
957 Miocene climate: results from a terrestrial model-data comparison. Climates of the Past
958 Discussions 8, 715–786.

959 Candy, I., Black, S., and Sellwood, B.W., 2004. Quantifying time scales of pedogenic
960 calcrete formation using U-series disequilibria. Sedimentary Geology, 170, p. 177–187.

961 Cheng, H., Edwards, R.L., Shen, C.C., Polyak, V.J., Asmerom, Y., Woodhead, J., Hellstrom,
962 J., Wang, Y., Kong, X., Spötl, C. and Wang, X., 2013. Improvements in ^{230}Th dating,
963 ^{230}Th and ^{234}U half-life values, and U–Th isotopic measurements by multi-collector
964 inductively coupled plasma mass spectrometry. Earth and Planetary Science Letters,
965 371, 82-91.

966 Clark, R.M., 1985. A FORTRAN program for constrained sequence-slotting based on
967 minimum combined path length. Computers & Geosciences 11, 605–617.

968 Collomb, G.R., 1962. E`tude geologique du Jabal Fezzan et de sa bordure paléozoque.
969 Notes Mém. Comp.Fr. Pétrole, 1, 35.

970 Cook, T.D., Murray, A.M., Simons, E.L., Attia, Y.S. and Chatrath P., 2010. A Miocene
971 selachian fauna from Moghra, Egypt. Hist. Biol vol 22, 78-87.

972 Cremaschi, M., Zerboni, A., 2009. Early to Middle Holocene landscape exploitation in a
973 drying environment: two case studies compared from the central Sahara (SW Fezzan,
974 Libya). Comptes Rendus Geoscience, 341, 689-702.

975 Cvetković, V., Toljić, M., Ammar, N. A., Rundić, L., Trish, K. B., 2010. Petrogenesis of the
976 eastern part of the Al Haruj basalts (Libya). Journal of African Earth Sciences, 58, 37-
977 50.

978 Domaci, L., Roehlicj, P., Bosak, P., 1991. Neogene to Pleistocene continental deposits in the
979 northern Fezzan and central Sirt Basin. In: Salem M.J., Beliad, M.N. (Eds.), The
980 geology of Libya, Elsevier, Amsterdam, 5, pp. 1785-1801.

981 Douarin, M. Elliot, M., Noble, S.R., Sinclair, D., Henry, L.A., Long, D., Moreton, S.G. and
982 Roberts, J.M., 2013. Growth of north-east Atlantic cold-water coral reefs and mounds
983 during the Holocene: a high resolution U-series and ^{14}C chronology. Earth Planet. Sci.
984 Lett., 375, 176–187

985 Drake, N.A., El-Hawat, A.S., Turner, P., Armitage, S.J., Salem, M.J., White, K.H., McLaren,
986 S., 2008. Palaeohydrology of the Fezzan Basin and surrounding regions: the last 7
987 million years. Palaeogeography, Palaeoclimatology, Palaeoecology 263, 131-145.

988 Drake, N.A., Blench, R.,M., Armitage, S.J., Bristow, C.S. White, K.H., 2011a. Ancient
989 watercourses and biogeography of the Sahara explain the peopling of the desert. Proc
990 National Acad. Sci. USA 108, 458–462.

991 Drake, N.A., Salem, M.J., Armitage, S.J., Francke, J., Hounslow, M.W., Hlal, O., White,
992 K.H., El-Hawat, A. 2011b. DMP XV: Palaeohydrology and Palaeoenvironment: Initial
993 results and report of 2010 and 2011 Fieldwork. Libyan Studies 42, 139-149.

994 Drake, N. A., Breeze, P., Parker, A., 2013. Palaeoclimate in the Saharan and Arabian
995 Deserts during the Middle Palaeolithic and the potential for hominin dispersals.
996 Quaternary International, 300, 48-61.

997 El Ebaidi S.A, Abdulsamad, E.O., 2005. Petrography and evaluation of some Meso-
998 Cenozoic raw materials deposits in Murzuq Basin, SW Libya: review and contribution.
999 The Fourth International Conference on the Geology of Africa, Vol. 2, pp. 255-26.
1000 Assiut, Egypt.

1001 El-Hawat, A.S., 1980. Carbonate-Terrigenous Cyclic Sedimentation and Palaeogeography of
1002 the Marada Formation (Middle Miocene), Sirt Basin. In: Salem, M.J., Busrewil, M.T.
1003 (Eds.) The Geology of Libya, Vol. 3. London, Academic Press pp. 427-448.

1004 El-Hawat, A.S., 2008. The Pre-Messinian Miocene stratigraphy and sedimentation in the
1005 Marada-Zaltan area, Sirte Basin, Libya. In: N.T. Boaz, A. El-Arnauti, P. Pavlakis, M.J.
1006 Salem (Eds.), Circum-Mediterranean Geology and Biotic Evolution of the Neogene
1007 Period: The Perspectives from Libya. Garyounis University Scientific Bulletin, Special
1008 Issue No.5, p. 23–32.

1009 El- Hawat, A., Pawellek, T., 2004. A field guidebook to the geology of Sirt Basin, Libya. RWE
1010 Dea North Africa, 73p.

1011 El-Hawat, A.S. and Salem, M.J., 1987. A case study of the stratigraphic subdivision of Ar-
1012 Rajmah Formation and its implication on the Miocene of Northern Libya. In: M. Deák
1013 (Ed.), VIII'th Congress of the Regional Committee on Mediterranean Neogene
1014 Stratigraphy: Symposium on European Late Cenozoic Mineral Resources, Budapest,
1015 15–22 September 1985, Geological Institute Yearbook vol. 70, Technical Publishing,
1016 Budapest, p. 173–183.

1017 Freytet, P. and Verrecchia, E.P., 2002. Lacustrine and palustrine carbonate petrography: an
1018 overview. J. Palaeolimnol., 27, 221–237 .

1019 Fujioka, F., Chappell, J., 2011. Desert landscape processes on a timescale of millions of
1020 years, probed by cosmogenic nuclides. Aeolian Research, 3, 157-164.

1021 Gary, A.C., Johnson, G.W. Ekart, D.D., Platon E., Wakefield, M.I., 2005. A method for two-
1022 well correlation using multivariate biostratigraphical data. In: Powell, A. J., Riding, J. B.
1023 (Eds.) Recent Developments in Applied Biostratigraphy. The Micropalaeontological
1024 Society, Special Publications, pp. 205–217.

1025 Gerdes, K.D., Winefield, P., Simmons, M.D., Van Oosterhout, C., 2010. The influence of
1026 basin architecture and eustacy on the evolution of Tethyan Mesozoic and Cenozoic
1027 carbonate sequences. In: F.S.P. Van Buchem, K.D. Gerdes, M. Esteban (Eds.),
1028 Mesozoic and Cenozoic Carbonate Systems of the Mediterranean and the Middle East:
1029 Stratigraphic and Diagenetic Reference Models, Geological Society, London, Special
1030 Publications, Vol. 329, p. 9–41.

1031 Geyh, M.A., Thiedig, F., 2008. The Middle Pleistocene Al Mahruqah Formation in the
1032 Murzuq Basin, northern Sahara, Libya evidence for orbitally-forced humid episodes
1033 during the last 500,000 years. Palaeogeography, Palaeoclimatology, Palaeoecology
1034 257,1-21.

1035 Gordon, A.D., Clark, R.M. Thompson, R., 1988. The use of constraints in sequence slotting.
1036 In: Diday, E. (Ed). Data analysis and informatics, V. North Holland Publishing,
1037 Amsterdam, pp. 353-364.

1038 Goudarzi, G.H., 1970. Geology and mineral resources of Libya — a reconnaissance. U.S.
1039 Geol. Surv. Prof. Pap. 660, 104p.

1040 Grubic, A., Dimitrijevic, M., Galecic, M., Jakovljevic, Z., Komarnicki, S., Protic, D., Radulovic,
1041 P., Roncevic N.S., 1991. Stratigraphy of Western Fezzan (SW Libya). In: Salem, M.J.,
1042 Belaid, M.N. (Eds), The Geology of Libya. Vol. 4, pp. 1529-1564.

1043 Gundobin, V.M., 1985. Geological map of Libya 1:250,000, Sheet: Qararat al Marar (NH 33-
1044 13) Explanatory Booklet. Industrial Research Centre, Tripoli.

1045 Hassan, S.M., 2013 Sequence Stratigraphy of the Lower Miocene Moghra Formation in the
1046 Qattara Depression, North Western Desert, Egypt. Springer Science & Business
1047 Media.

1048 Hilgen, F.J., Lourens, L.J., Van Dam, J.A., 2012. The Neogene Period. In: Gradstein, F. M.,
1049 Ogg, J. G., Schmitz, M., Ogg, G. (Eds.). Vol. II, The Geologic Time Scale 2012,
1050 Elsevier, pp. 923-978.

1051 Hounslow, M.W., McIntosh, G., 2003. Magnetostratigraphy of the Sherwood Sandstone
1052 Group (Lower and Middle Triassic), south Devon, UK: detailed correlation of the marine
1053 and non-marine Anisian. Palaeogeography, Palaeoclimatology, Palaeoecology 193,
1054 325-348.

1055 Hounslow, M.W., 2006. PMagTools version 4.2- a tool for analysis of 2-D and 3-D directional
1056 data. http://dx.doi.org/10.13140/RG.2.2.19872.58880

1057

1058 Hounslow, M.W., 2016. Paleozoic geomagnetic reversal rates following superchrons have a
1059 fast re-start mechanism. Nat. Commun., 7, http://dx.doi.org/10.1038/ncomms12507

1060

1061 Hounslow, M.W. and Clark, R.M., 2016. CPLSlot a program for objective correlation between
1062 successions using sequence slotting. http://dx.doi.org/10.13140/RG.2.2.17513.29288 .

1063 IRC, 1985. 1:1,000000 geological map of Libya, Industrial Research Centre, Tripoli.

1064 Kent, J.T., Briden, J.C., Mardia, K.V., 1983. Linear and planar structure in ordered
1065 mulivariate data as applied to progressive demagnetisation of palaeomagnetic
1066 remanence. Geophysical Journal Royal Astronomical Society 81, 75-87.

1067 Koráb, T.,1984. Geological Map of Libya 1: 250 000. Sheet: Tmassah NG 33-7. Explanatory
1068 Booklet. Industrial Research Centre, Tripoli.

1069 Kostadinova M., Jordanova N., Jordanova D., Kovacheva M., 2004. Preliminary study on the
1070 effect of water glass impregnation on the rock-magnetic properties of baked clay.
1071 Studia Geophysica et Geodaetica, 48, 637-646.

1072 Lallier, F., Antoine, C., Charreau, J., Caumon, G., Ruiu, J., 2013. Management of
1073 ambiguities in magnetostratigraphic correlation. Earth and Planetary Science Letters,
1074 371, 26-36.

1075 Larrasoaña J.C., Roberts, A.P., Rohling, E.J., 2013. Dynamics of green Sahara periods and
1076 their role in hominin evolution. PLoS one 8, doi: 10.1371/journal.pone.0076514

1077 Lézine, A.M., Hély, C., Grenier, C., Braconnot, P., Krinner, G., 2011. Sahara and Sahel
1078 vulnerability to climate changes, lessons from Holocene hydrological data. Quaternary
1079 Science Reviews, 30, 3001-3012.

1080 Liégeois, J. P., Benhallou, A., Azzouni-Sekkal, A., Yahiaoui, R., Bonin, B., 2005. The Hoggar
1081 swell and volcanism: reactivation of the Precambrian Tuareg shield during Alpine
1082 convergence and West African Cenozoic volcanism. In. Foulger, G.R., Hatland, J.H.
1083 Presnall, D.C., Anderson, D.L. (Eds). Plates, plumes and paradigms. Geological
1084 Society of America Special Papers, 388, 379-400.

1085 Liu, B., Saito, Y., Yamazaki, T. Abdeldayem, A., Oda, H. Hori, K., Zhao, Q., 2001.
1086 Paleocurrent analysis for the Late Pleistocene–Holocene incised-valley fill of the
1087 Yangtze delta, China by using anisotropy of magnetic susceptibility data. Marine
1088 Geology, 176, 175–189.

1089 Liu, B., Saito, Y., Yamazaki, T., Abdeldayem, A., Oda, H., Hori, K., Zhao, Q., 2001.
1090 Paleocurrent analysis for the Late Pleistocene–Holocene incised-valley fill of the
1091 Yangtze delta, China by using anisotropy of magnetic susceptibility data. Mar. Geol.,
1092 176 (2001), 175–189.

1093 Llinás-Agrasar, E.L., 2004. Crocodile remains from the Burdigalian (lower Miocene) of Gebel
1094 Zelten (Libya). Geodiversitas, 26, 309–321.

1095 Lowrie, W., Alvarez, W., 1984. Lower Cretaceous magnetic stratigraphy in Umbrian pelagic
1096 limestone sections. Earth and Planetary Science Letters 71, 315−328.

1097 Lowrie, W., Kent, D.V., 2004. Geomagnetic polarity timescales and reversal frequency
1098 regimes, In: Channell, J.E.T., Kent, D.V., Lowrie, W., Meert, J. (Eds.) Timescales of
1099 the paleomagnetic field, America Geophysical Union, pp. 117-129.

1100 Man, O., 2008. On the identification of magnetostratigraphic polarity zones. Stud. Geophys.
1101 Geod. 52, 173−186.

1102 Man, O., 2011. The maximum likelihood dating of magnetostratigraphic sections.
1103 Geophysical Journal International, 185, 133-143.

1104 Mannaï-Tayech, B., 2009. The lithostratigraphy of Miocene series from Tunisia, revisited

1105 J. Afr. Earth Sci., 54, 53–61.

1106 Mannaï-Tayech, B., Otero, O. 2005. Un nouveau gisement miocène à ichthyofaune au sud
1107 de la chaîne des Chotts (Tunisie méridionale). Paléoenviron. Paléobiogéogr. Comptes
1108 Rendus Palevol, 4, 405–412 .

1109 Márton, E., Márton, P., Heller, F., 1980. Remanent magnetization of a Pliensbachian
1110 limestone sequence at Bakonycsernye (Hungary). Earth and Planetary Science
1111 Letters, 48, 218-226.

1112 Mastera, L., 1985. Geological map of Libya 1:250 000. Sheet Maradah (NH 34–9).
1113 Explanatory Booklet. Industrial Research Centre, Tripoli, Libya.

1114 McFadden, P.L., McElhinny, M.W., 1988. The combined analysis of remagnetisation circles
1115 and direct observations in paleomagnetism. Earth Planetary Science Letters 87, 161-
1116 172.

1117 McFadden, P.L., McElhinny, M.W., 1990. Classification of the reversal test in
1118 paleomagnetism. Geophysical Journal International 103, 725-729.

1119 Morlo, M., Miller, E.R., El-Barkooky, A.N., 2007. Creodonta and Carnivora from Wadi
1120 Moghra, Egypt. J. Vertebr. Paleontol., 27, 145–159 .

1121 Ogg, J.G., Steiner, M.B., 1991. Early Triassic polarity time-scale: integration of
1122 magnetostratigraphy, ammonite zonation and sequence stratigraphy from stratotype
1123 sections (Canadian Arctic Archipelago). Earth and Planetary Science Letters 107, 69-
1124 89.

1125 Ogg, J.G., 2012. Geomagnetic polarity timescale. In: Gradstein, F. M., Ogg, J. G., Schmitz,
1126 M., Ogg, G. (Eds.), Vol.1. The Geologic Time Scale 2012, Elsevier, pp. 85-114.

1127 Olson, P., Hinnov, L., Driscoll, P., 2014. Nonrandom geomagnetic reversal times and
1128 geodynamo evolution. Earth and Planetary Science Letters 388, 9–17.

1129 Opdyke, N.D., Channell, J.E., 1996. Magnetic stratigraphy. International Geophysical Series
1130 Vol. 64, Academic Press, London.

1131 Osmond, J. K., Dabous, A. A., 2004. Timing and intensity of groundwater movement during
1132 Egyptian Sahara pluvial periods by U-series analysis of secondary U in ores and
1133 carbonates. Quaternary Research 61, 85-94.

1134 Pachur, H.-J., Hoelzmann, P., 2000 Late Quaternary paleoecology and paleoclimates of the
1135 eastern Sahara. Journal of African Earth Sciences 30, 929-939.

1136 Paillou, P., Schuster, M., Tooth, S., Farr, T., Rosenqvist, A., Lopez S., Malezieux, J.M. 2009.
1137 Mapping of a major paleodrainage system in eastern Libya using orbital imaging radar:
1138 The Kufrah River. Earth and Planetary Science Letters 277, 327–333.

1139 Parizek, A., Klen, L., Röhlich, P., 1984. Geological map of Libya 1:250,000, Sheet: Idri (NG
1140 33-1) Explanatory Booklet. Industrial Research Centre, Tripoli.

1141 Petit-Maire, N., Delibrias, G., Gaven, C., 1980. Pleistocene lakes in the Shati area, Fezzan
1142 (27 30'N). Paleoecology of Africa 12, 289-295.

1143 Radivojević, M., Toljić, M., Turki, S. M., Bojić, Z., Šarić, K., Cvetković, V., 2015. Neogene to
1144 Quaternary basalts of the Jabal Eghei (Nuqay) area (south Libya): Two distinct volcanic
1145 events or continuous volcanism with gradual shift in magma composition? Journal of
1146 Volcanology and Geothermal Research 293, 57-74.

1147 Roncevic, N.S., 1984. Geological map of Libya 1:250,000, Sheet: Hasi Anjiwal (NG 32-4)
1148 Explanatory Booklet. Industrial Research Centre, Tripoli.

1149 Schlüter, J. Schultz, L. Thiedig, F., Al-Mahdi, B.O., Abu Aghreb, A.E., 2002. The Dar al Gani
1150 meteorite field (Libyan Shara): geological setting, pairing of meteorites and recover
1151 density. Meteorite and Planetary Science 37, 1079-1093.

1152 Schuster, M., Duringer, P., Ghienne, J.-F., Vignaud, P., Taisso, H., Likius, M.A., Brunet, M.,
1153 2006. The Age of the Sahara Desert. Science, 311, 821.

1154 Seidl, K., Röhlich, P., 1984. Geological map of Libya, 1: 250 000. Sheet Sabhá (NG 33-2),
1155 Explanatory Booklet, Industrial Research Centre, Tripoli.

1156 Smilde, A. K., Kiers, H.A.L., Bijlsma S., Rubingh C.M., van Erk, M.J., 2009. Matrix
1157 correlations for high-dimensional data: the modified RV-coefficient. Bioinformatics 25,
1158 401–405.

1159 Stoetzel, E., 2013. Late Cenozoic micromammal biochronology of northwestern Africa.
1160 Palaeogeogr. Palaeoclimatol. Palaeoecol., 392 (2013), pp. 359–381

1161 Swezey, C.S., 2009. Cenozoic stratigraphy of the Sahara, northern Africa J. Afr. Earth Sci.,
1162 53, 89–121.

1163 Thiedig, F.M., Oezen, D., El-Chair, M., Geyh, M.A., 2000. The absolute age of the
1164 Quaternary lacustrine limestone of the Al Mahruqah Formation — Murzuq Basin, Libya.
1165 In: Sola, M.A., Worsley, D. (Eds.), Geological Exploration in the Murzuq Basin.
1166 Elsevier, Amsterdam, pp. 89–116.

1167 Thiedig, F.M., Geyh, M.A., 2004. Zyklische lakustrine Kalke im abflusslosen Murzuq-Becken
1168 (Libyen) als Zeugnisse interglazialer Feuchtphasen in Nordafrika während der letzten
1169 500 ka. Beitrag zur Regionalen Geographie 135, 267-288.

1170 Thompson, R., Clark, R.M., 1989. Sequence slotting for stratigraphic correlation between
1171 cores: theory and practice. Journal of Paleolimnology 2, 173–184.

1172 Torsvik, T. H., Van der Voo, R., Preeden, U., Mac Niocaill, C., Steinberger, B., Doubrovine,
1173 P. V., van Hinsbergen D.J.J., Domeiere, M., Gaina, C., Tohver, E. , Meert, J.G.,
1174 McCausland, P. J.A., Cocks, L. R. M., 2012. Phanerozoic polar wander,
1175 paleogeography and dynamics. Earth-Science Reviews 114, 325-368.

1176 Van Velzen, A. J., Zijderveld, J. D. A., 1992. A method to study alterations of magnetic
1177 minerals during thermal demagnetization applied to a fine-grained marine marl (Trubi
1178 formation, Sicily). Geophysical journal international, 110, 79-90.

1179 Wanas, H.A. Pickford, M. Mein, P., Soliman, H. Segalen, L. 2009. Late Miocene karst
1180 system at Sheikh Abdullah, between Bahariya and Farafra, Western Desert, Egypt:
1181 implications for palaeoclimate and geomorphology. Geologica Acta, 7, 275-287.

Wessels, W., Fejfar, O., Peláez-Campomanes, P. van der Meulen, A., de Bruijn, H., 2003. Miocene small mammals from Jebel Zelten, Libya. Coloquuis de Paleontologia, Vol. 1, 699-715.

White, K., McLaren, S., Black, S., Parker, A., 2000. Evaporite minerals and organic horizons in sedimentary sequences in the Libyan Fezzan: implications for palaeoenvironmental reconstruction. In: McLaren, S.J., Kniveton, D.R. (eds) Linking climate change to land surface change, Springer, Netherlands, pp. 193-208.

Woller, F., 1984. Geological Map of Libya 1: 250 000. Sheet: Al Fuqaha (NG 33-3). Explanatory Booklet. Industrial Research Center, Tripoli.

Wright, V.P., Platt, N.H. 1995. Seasonal wetland carbonate sequences and dynamic catenas: a re-appraisal of palustrine limestones. Sediment. Geol., 99, 65–71.

Zaki, A., Abdel-Fattah, Z.A., Kora, M.A., Ayyad, S.N. 2013. Facies architecture and depositional development of Middle Miocene carbonate strata at Siwa Oasis, Northwestern Egypt. Facies, 59, 505–528.

Zhang, Z., Ramstein, G., Schuster, M., Li, C., Contoux, C. Yan, Q., 2014. Aridification of the Sahara desert caused by Tethys Sea shrinkage during the Late Miocene. Nature, 513, 401-404.

Figure and Table Captions.

Fig. 1. Outline geology of the Fezzan with location of inserts indicated, showing the edge of the SW fringe of the Sirte Basin, indicated by the eastern outcrop edge of the Paleogene. To the north, the edge of the Ghadamas Basin in the Al Hamadah al Hamra (shown as Paleogene outcrop) indicates the northern edge of the Fezzan Basin. Position of this larger map shown on the outline of Libya in the corner. Important troughs and uplifts shown, indicate by major fault-bounding systems in the SW Sirte Basin. Large grey arrows are hypothesised drainage exists from the Fezzan Basin referred to as the northerly Wadi Nashu, and easterly Wadi Barjuj exits (Drake et al., 2008, 2011a). Locations of detailed maps and cross-sections in Figs. 3,5,6,7,8 also shown. Map simplified and based on IRC (1985).

Fig. 2. New lithostratigraphy of the Al Mahruqah Group in the Fezzan, with major events and features indicated. The major erosion/deflation events are indicated in blue, which sub-divide the new formations.

Fig. 3. Regional stratigraphic relationships of the Miocene and younger sediments in the Fezzan study area, based on this work. The Zarzur Formation ages are inferred based on this work and Armitage et al. (2007). Data for the Sirte Basin from El-Hawat (1980), El-Hawat and Pawellek (2004).

Fig. 4. Regional stratigraphic relationships of the Miocene and younger sediments in the Fezzan study area. The Zarzur Formation ages are inferred based on this work and

Armitage et al. (2007). Miocene ages based on this work. Data for the Sirte Basin from El-Hawat (1980), El Hawat and Pawellek (2004).

Fig. 5. Locations of sections shown in Fig. 6, along the Wadi ash Shati to Wadi Kunayr depression. The dark coloured Paleozoic formations are clearly shown to the north side of the Wadi ash Shati to Ar Ramish as Saghirah region. The pale-coloured Shabirinah Formation on the east can clearly be seen overstepping onto the Paleozoic. Image from bing.co.uk. The highest elevation Zarzur Formation is 379 m at Bir az Zallaf, the lowest elevation Shabirinah Formation in the east of this map is at around 395 m, similar to that at the SK3 site (Fig. 6). Line of cross-section shown in Fig. 3 is dashed line.

Fig. 6. Schematic section and correlation along North side of Wadi ash Shati towards Wadi Kunayr area. See Fig. 5 for locations. Vertical filled bars (blue) show the height ranges of the plateau formed on the top of the Brak Formation, implying the Brak Formation extends to these maximum elevations (tops of bars) at these locations. Those locations with existing logs, have the top of the logs located at the estimated lowest plateau elevation to determine the base of the Brak Formation. Dashed (red) line is the elevation of the Paleozoic basement. All sections with same metre scale, as shown on the right. Heights from Google Earth. Some logs from Abdullah (2010). Also shown are the equivalent Geyh and Theidig (2008) sites. Log key in Fig. 10.

Fig. 7. Interpreted geological cross-section from the North side of Wadi Kunayr through section SK8 to the NNE. Topography shown in red. Elevations from Google Earth. Based on our interpretation of the Al Fuqha geological map (Woller, 1984). Woller (1984) wrongly interpret the Mahruqah outcrops as the Maastrichtian Bin Affin Member in parts of the Wadi Kunayr area. G&T= Geyh and Theidig (2008). A photo of the clastic units in the deepest endoreic depression is shown as Plate 5a in Theidig et al. (2000). To the south of section SK8 basement rises again to 480-490 m elevation within 16 km.

Fig. 8. The figured sections and locations in the Tmassah- Wadi ash Shabirinah areas. The Stromatolite Member in the Sarir al Qattusah can be traced a further 70 km north of the map boundary, along the bright coloured ground in the satellite image- along the Qattusah corridor. Base image from Bing.co.uk. Log key in Fig. 10. The grey-lines are supposed track/roadways. Some 30 km south of the TS2/TS3 sections the Jurassic-Cretaceous basement of the Dur an Naqah rises (off the map) to above 500 m elevation.

Fig. 9. Schematic relationships of sections east of Tmassah in the area north of Wadi ash Shabirinah. GE= Google Earth elevation on section top or bottom. Same vertical scale for all sections, except TS3, which is shrunk to fit the other scales better. Distances (in blue) between sections indicated. Location of sections shown on Fig. 8.

Fig. 10. Section logs and summary horizon magnetic polarity data for the sections. Width of the bar in the polarity boxes indicates the confidence in the polarity information obtained from the two to three specimens from each sample level.

Fig. 11. Representative demagnetisation data from the Al Mahruqah Group. A,b)= section SK8; c,d)= section SK3, e,f)=section TS3. a) Specimen AP2A, normal polarity (N, behaviour S2), showing a ChRM from 400 to 570^{o}C. b) AP46C, reverse polarity (R, behaviour T2), showing component A from NRM to 350^{o}C, above which an erratic trend towards reverse polarity, sith reverse polarity evident from 500^{o}C. c) BC18A, normal polarity (N?, behaviour T2), showing component A from NRM to 400^{o}C. A great circle is fitted from 490^{o}C-origin. d) BC22, reverse polarity (R?, behaviour T1), showing component A NRM to 300^{o}C, with plane fitted from 300^{o}C-origin. e) TM71, reverse polarity (R, behaviour S2), showing a ChRM from 510 to the origin. f) TM1A, reverse polarity (R??, behaviour T3), showing a strong A component from 100-460^{o}C, the steps at 520-550^{o}C recovers a reverse component. Great circle plane fitted from 490^{o}C to origin. See Fig. 10 for specimen locations.

Fig. 12. Detailed magnetostratigraphic data for the sections a) SK3, b) SK8 and c) TS3. In each case the columns are: i) Strength of the specimen natural remanent magnetisation (NRM), ii) Specimen demagnetisation behaviour showing categorisation into good (S1) and poor (S3) ChRM line-fits; great circle fit quality range from good (T1) to poor (T3), and specimens with no Miocene magnetisation are indicated in the X column (see text for details). iii) Interpreted specimen polarity quality, with those in the mid-grey column not assigned a polarity. Poorest quality in column headed ??. iv) Specimen VGP latitude, and horizon polarity. Filled symbols= those specimens possessing an S-class ChRM, and unfilled symbols for specimens with T-class, great-circle behaviour. Polarity key in Fig.10.

Fig. 13. The two composite magnetic polarity stratigraphies (composite A (left) and B (right)) discussed in the text, and the basis of these derived from the section data. Scales in metres. The final age model using composite-B is shown on the right, with the chron correlation lines to the geomagnetic polarity timescale (Ogg, 2012) derived from the sequence slotting (see Supplementary Data for details).

Fig. 14. Comparison of environmental systems in the early and mid-Miocene between Libya, Tunisia and western Egypt. Data for Tunisia based on Blondel et al. (1993) and Mannaï-Tayech (2009). Egyptian data from Albritton et al. (1990) and Hassan (2013). Sirte Basin data from El-Hawat (2008) and El-Hawat and Pawellek (2004). The chronology of the non-Fezzan Basin formation is mostly secure in the marine units (pelagic foraminifera zones indicated on Tunisia data), and is based on vertebrates in some units and lithostratigraphically inferred in other units.

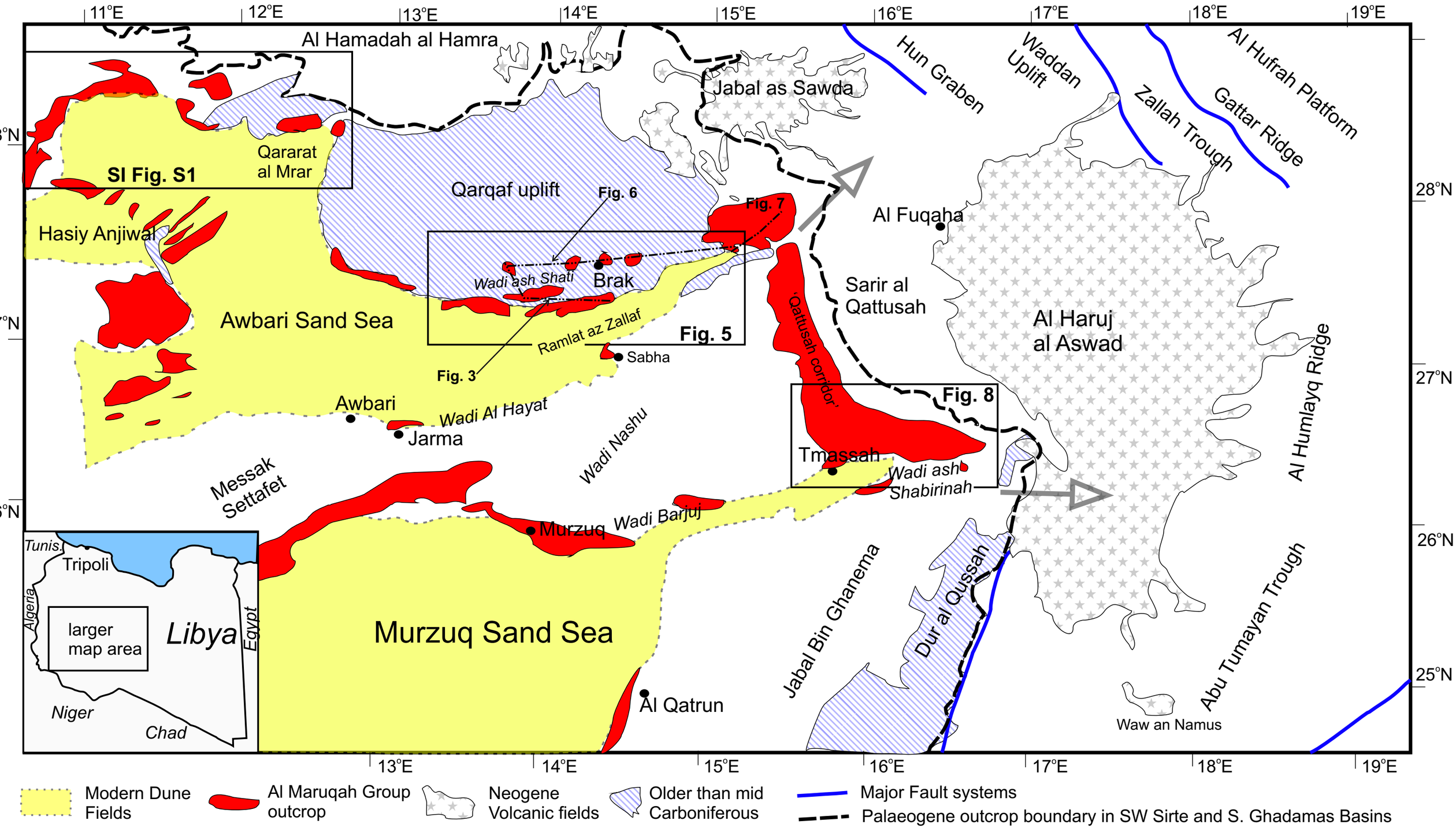
11°E
12°E
13°E
14°E
15°E
16°E
17°E
18°E
19°E
28°N
27°N
26°N
25°N
Al Hamadah al Hamra
Jabal as Sawda
Hun Graben
Waddan Uplift
Zallah Trough
Gattar Ridge
Al Hufrah Platform
SI Fig. S1
Qararat al Mrar
Qarqaf uplift
Fig. 6
Fig. 7
Hasiy Anjiwal
Wadi ash Shati
Brak
Awbari Sand Sea
Ramlat az Zallaf
Fig. 5
Sabha
Fig. 3
Awbari
Wadi Al Hayat
Jarma
Wadi Nashu
'Qattusah corridor'
Fig. 8
Tmassah
Wadi ash Shabirinah
Sarir al Qattusah
Al Fuqaha
Al Haruj al Aswad
Al Humlayq Ridge
Messak Settafet
Murzuq
Wadi Barjuj
Murzuq Sand Sea
Jabal Bin Ghanema
Dur al Qussah
Abu Tumayan Trough
Waw an Namus
Al Qatrun
Tunis
Tripoli
Algeria
Egypt
larger map area
Libya
Niger
Chad
Modern Dune Fields
Al Maruqah Group outcrop
Neogene Volcanic fields
Older than mid Carboniferous
Major Fault systems
Palaeogene outcrop boundary in SW Sirte and S. Ghadamas Basins

Fig. 1.

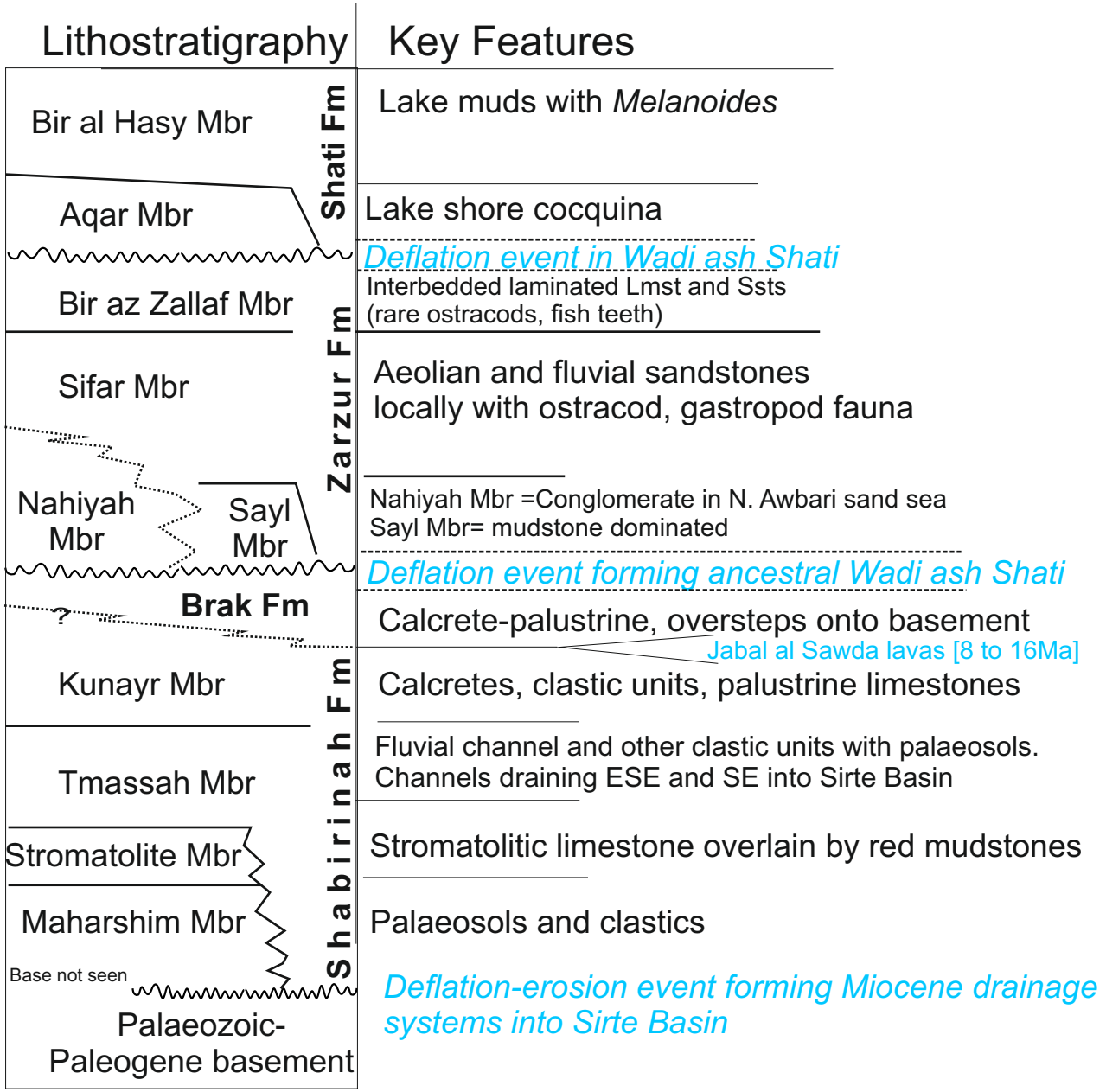
Lithostratigraphy
Key Features
Bir al Hasy Mbr
Shati Fm
Lake muds with Melanoides
Aqar Mbr
Lake shore cocquina
Deflation event in Wadi ash Shati
Bir az Zallaf Mbr
Interbedded laminated Lmst and Ssts
(rare ostracods, fish teeth)
Sifar Mbr
Zarzur Fm
Aeolian and fluvial sandstones
locally with ostracod, gastropod fauna
Nahiyah Mbr
Sayl Mbr
Nahiyah Mbr =Conglomerate in N. Awbari sand sea
Sayl Mbr= mudstone dominated
Deflation event forming ancestral Wadi ash Shati
Brak Fm
?
Calcrete-palustrine, oversteps onto basement
Jabal al Sawda lavas [8 to 16Ma]
Kunayr Mbr
Shabirinah Fm
Calcretes, clastic units, palustrine limestones
Tmassah Mbr
Fluvial channel and other clastic units with palaeosols.
Channels draining ESE and SE into Sirte Basin
Stromatolite Mbr
Stromatolitic limestone overlain by red mudstones
Maharshim Mbr
Palaeosols and clastics
Base not seen
Deflation-erosion event forming Miocene drainage systems into Sirte Basin
Palaeozoic-
Paleogene basement

Fig. 2.

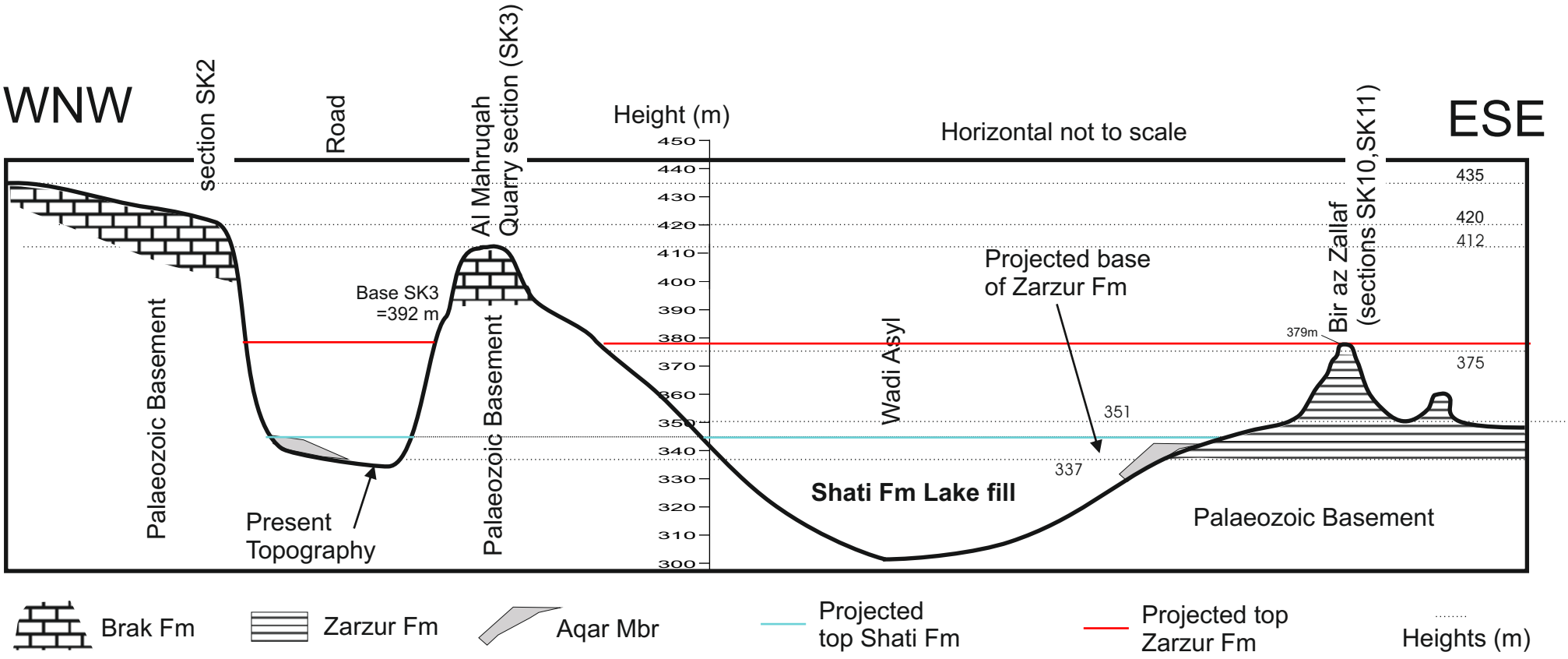
WNW
ESE
section SK2
Road
Al Mahruqah Quarry section (SK3)
Height (m)
Horizontal not to scale
Bir az Zallaf (sections SK10,SK11)
450
440
430
420
410
400
390
380
370
360
350
340
330
320
310
300
435
420
412
375
379m
351
337
Base SK3 =392 m
Palaeozoic Basement
Present Topography
Palaeozoic Basement
Wadi Asyl
Projected base of Zarzur Fm
Shati Fm Lake fill
Palaeozoic Basement
Brak Fm
Zarzur Fm
Aqar Mbr
Projected top Shati Fm
Projected top Zarzur Fm
Heights (m)

Fig. 3.

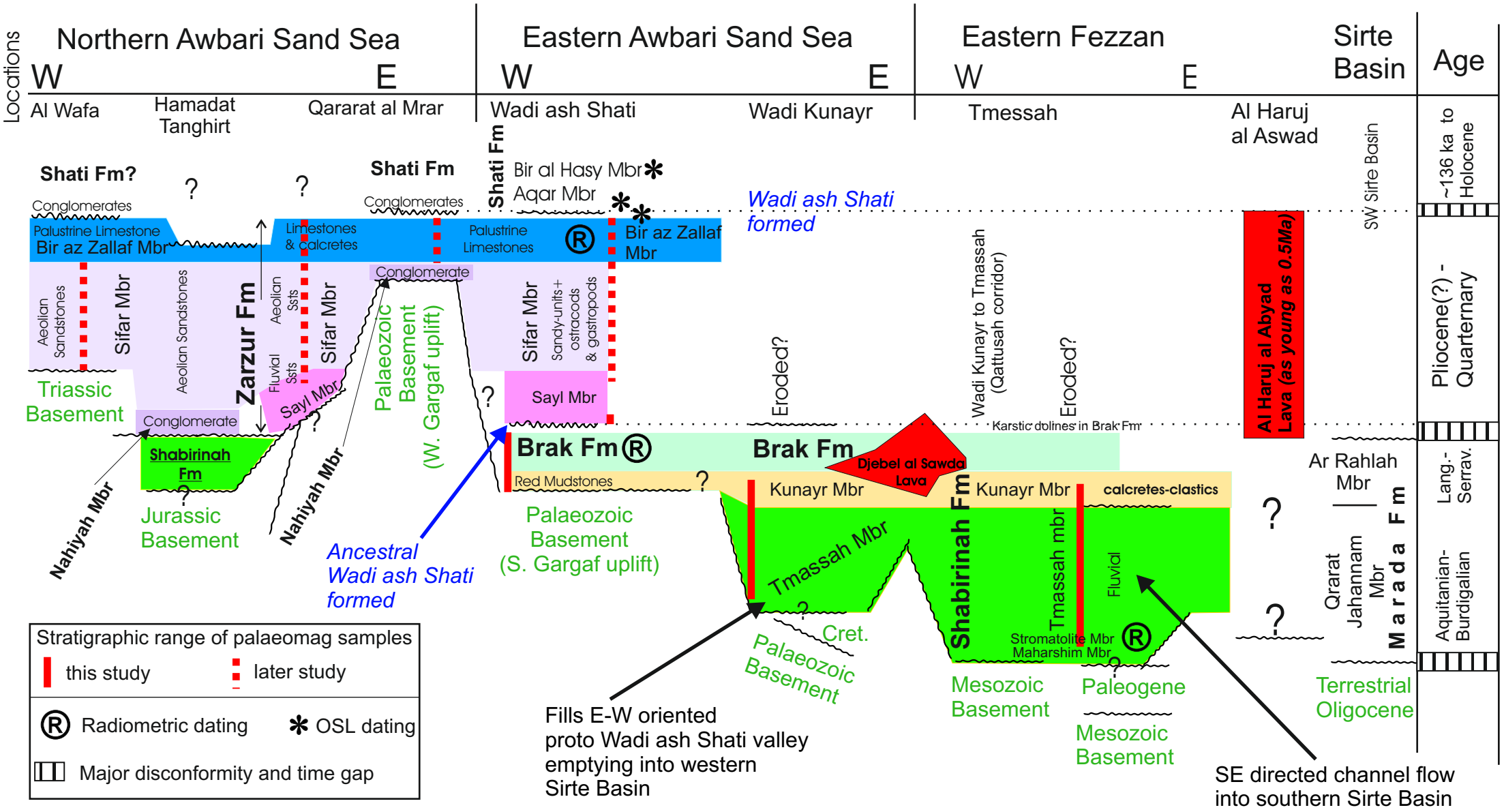
Locations
Northern Awbari Sand Sea
W
E
Al Wafa
Hamadat Tanghirt
Qararat al Mrar
Eastern Awbari Sand Sea
W
E
Wadi ash Shati
Wadi Kunayr
Eastern Fezzan
W
E
Tmessah
Al Haruj al Aswad
Sirte Basin
Age
~136 ka to Holocene
Pliocene(?) - Quarternary
Lang.-Serrav.
Aquitanian-Burdigalian
Terrestrial Oligocene
Shati Fm?
Conglomerates
Palustrine Limestone
Bir az Zallaf Mbr
Aeolian Sandstones
Sifar Mbr
Zarzur Fm
Triassic Basement
Conglomerate
Shabirinah Fm
Jurassic Basement
Nahiyah Mbr
Shati Fm
Conglomerates
Limestones & calcretes
Aeolian Ssts
Fluvial Ssts
Sifar Mbr
Sayl Mbr
Nahiyah Mbr
Conglomerate
Palaeozoic Basement (W. Gargaf uplift)
Ancestral Wadi ash Shati formed
Shati Fm
Bir al Hasy Mbr
Aqar Mbr
Palustrine Limestones
Bir az Zallaf Mbr
Sifar Mbr
Sandy-units + ostracods & gastropods
Sayl Mbr
Brak Fm
Red Mudstones
Palaeozoic Basement (S. Gargaf uplift)
Wadi ash Shati formed
Eroded?
Wadi Kunayr to Tmassah (Qattusah corridor)
Eroded?
Karstic dolines in Brak Fm
Brak Fm
Djebel al Sawda Lava
Kunayr Mbr
Kunayr Mbr
calcretes-clastics
Tmassah Mbr
Cret.
Palaeozoic Basement
Shabirinah Fm
Tmassah mbr
Fluvial
Stromatolite Mbr
Maharshim Mbr
Mesozoic Basement
Paleogene
Mesozoic Basement
Al Haruj al Abyad Lava (as young as 0.5Ma)
SW Sirte Basin
Ar Rahlah Mbr
Qrarat Jahannam Mbr
Marada Fm
Terrestrial Oligocene
Fills E-W oriented proto Wadi ash Shati valley emptying into western Sirte Basin
SE directed channel flow into southern Sirte Basin
Stratigraphic range of palaeomag samples
this study
later study
Radiometric dating
OSL dating
Major disconformity and time gap

Fig. 4. .

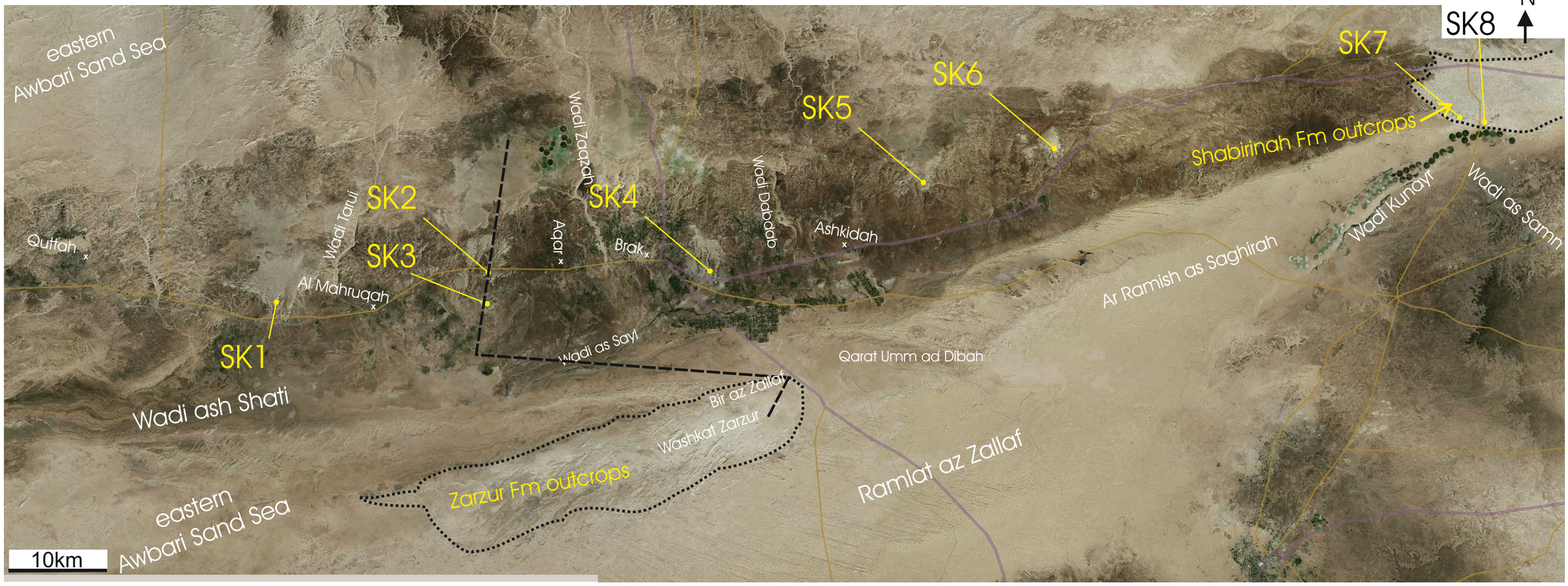
N
SK8
SK7
SK6
SK5
SK4
SK3
SK2
SK1
eastern
Awbari Sand Sea
Wadi Zaazah
Wadi Tarui
Wadi Dabdab
Shabirinah Fm outcrops
Wadi Kunayr
Wadi as Samn
Quttah
Aqar
Brak
Ashkidah
Al Mahruqah
Ar Ramish as Saghirah
Wadi as Sayl
Qarat Umm ad Dibah
Bir az Zallaf
Washkat Zarzur
Wadi ash Shati
Zarzur Fm outcrops
Ramlat az Zallaf
eastern
Awbari Sand Sea
10km

Fig. 5.

WSW

ENE

Fig. 6.

SK-1

SK-2

SK-3

SK-4

SK-5

SK-6

SK-7

SK-8

SK-9

Height ranges of Brak Fm plataeu

Geyt &Theidig Brak site 6

Abdullah-Site B (top 419-423 m)

Abdullah-Site A (top 412-419 m)

Geyh &Thiedig Brak sites 5b,c,e

Brak Fm

Palaeozoic Basement

Al Mahruqah Quarry

Geyh &Thiedig, Brak sites 6b,c

Top 413m

Shab. Fm

Aqar

Top Brak Fm (412-420 m)

Thick Breccia

Brak outcrop

Ashkidah outcrop

Post- Brak Fm Fault?

Ashkidah Brak Fm (~446 m)

Abdullah Site C (top ca. 444 m)

444 m

top ca. 430 to 432 m

Kunayr Mbr

Devonian Basement at ca. 400 m

Shabirinah Formation

ca. 437 m

Top= 458 m

Geyh &Thiedig Brak, site 8

Height (m) from Goggle Earth

Mud VF F M C VC Cong.

Sand

Locations

Al Mahruqah

Palaeozoic Basement

Base= ca. 393 m

Distances between Outcrops

12 km | 9 km | 2.8 km | 21 km | 31 km | 14 km | 43 km | 2.3 km | 33 km

285 m | 285 m | 285 m | 298 m | 320 m | 326 m | 334 m | 388 m | 390 m

Present Day Wadi elevation

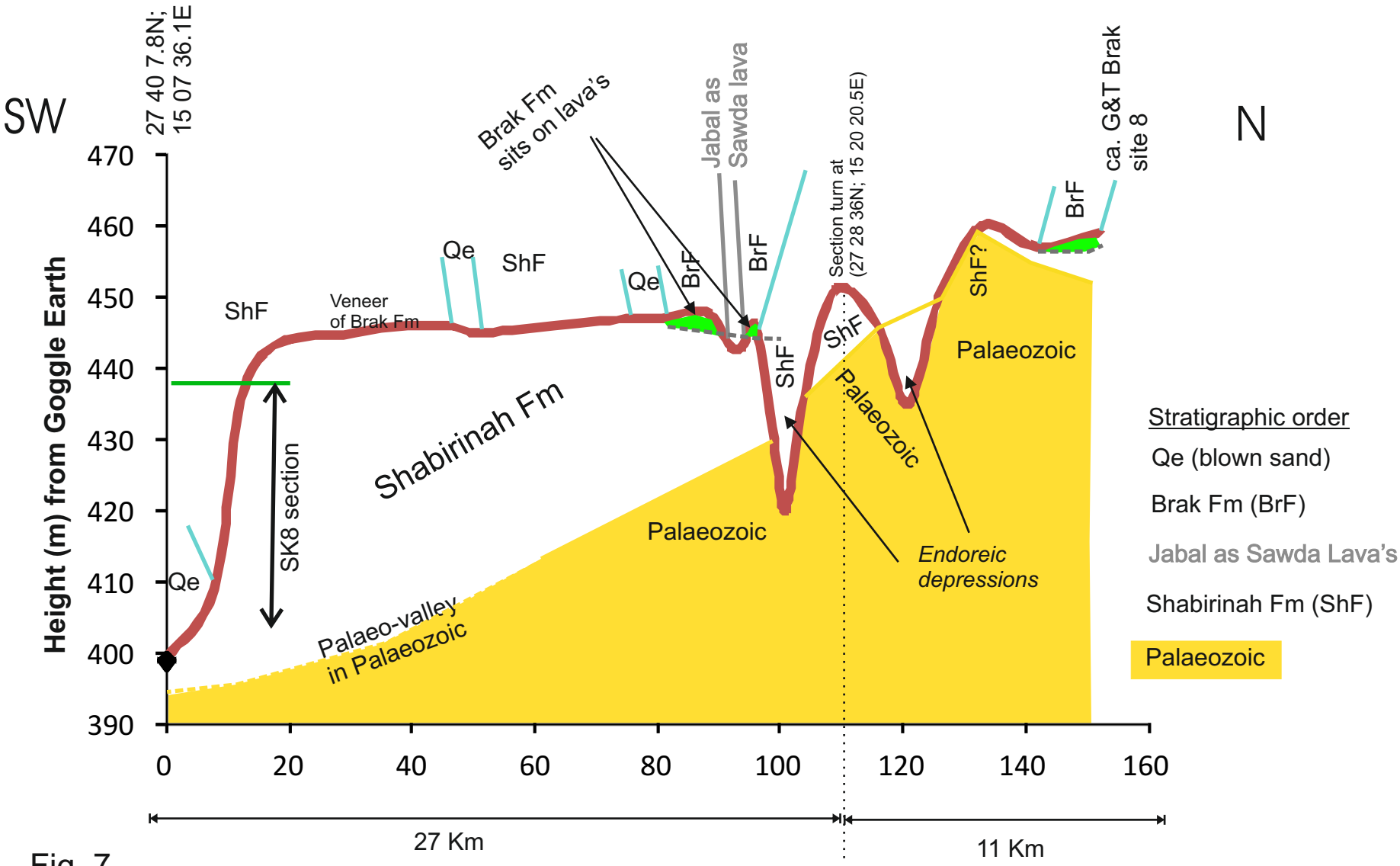
SW
N
27 40 7.8N; 15 07 36.1E
Height (m) from Goggle Earth
470
460
450
440
430
420
410
400
390
0
20
40
60
80
100
120
140
160
27 Km
11 Km
Brak Fm sits on lava's
Jabal as Sawda lava
Section turn at (27 28 36N; 15 20 20.5E)
ca. G&T Brak site 8
ShF
Veneer of Brak Fm
Qe
ShF
Qe
BrF
BrF
ShF
ShF
ShF?
BrF
Shabirinah Fm
SK8 section
Qe
Palaeozoic
Palaeozoic
Palaeozoic
Palaeo-valley in Palaeozoic
Endoreic depressions
Stratigraphic order
Qe (blown sand)
Brak Fm (BrF)
Jabal as Sawda Lava's
Shabirinah Fm (ShF)
Palaeozoic

Fig. 7.

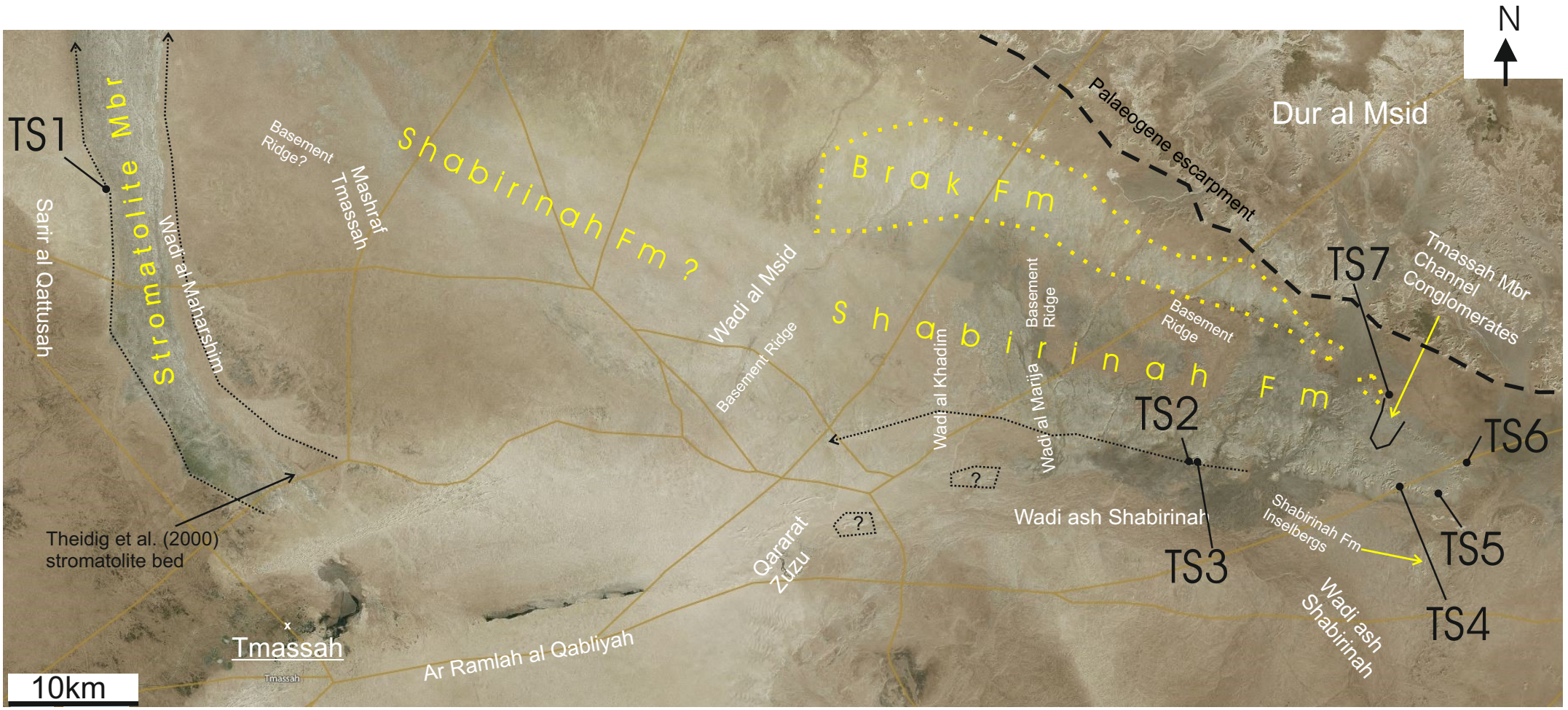

Observed and inferred outcrop boundary or trend of the Stromatolite Mbr

Observed and inferred outcrop of the Brak Fm

Fig. 8.

Fig. 9.

Cross-bedding dip directions
in Tmassah Fm
0%
5
10
15
Vm= 121°
N= 76

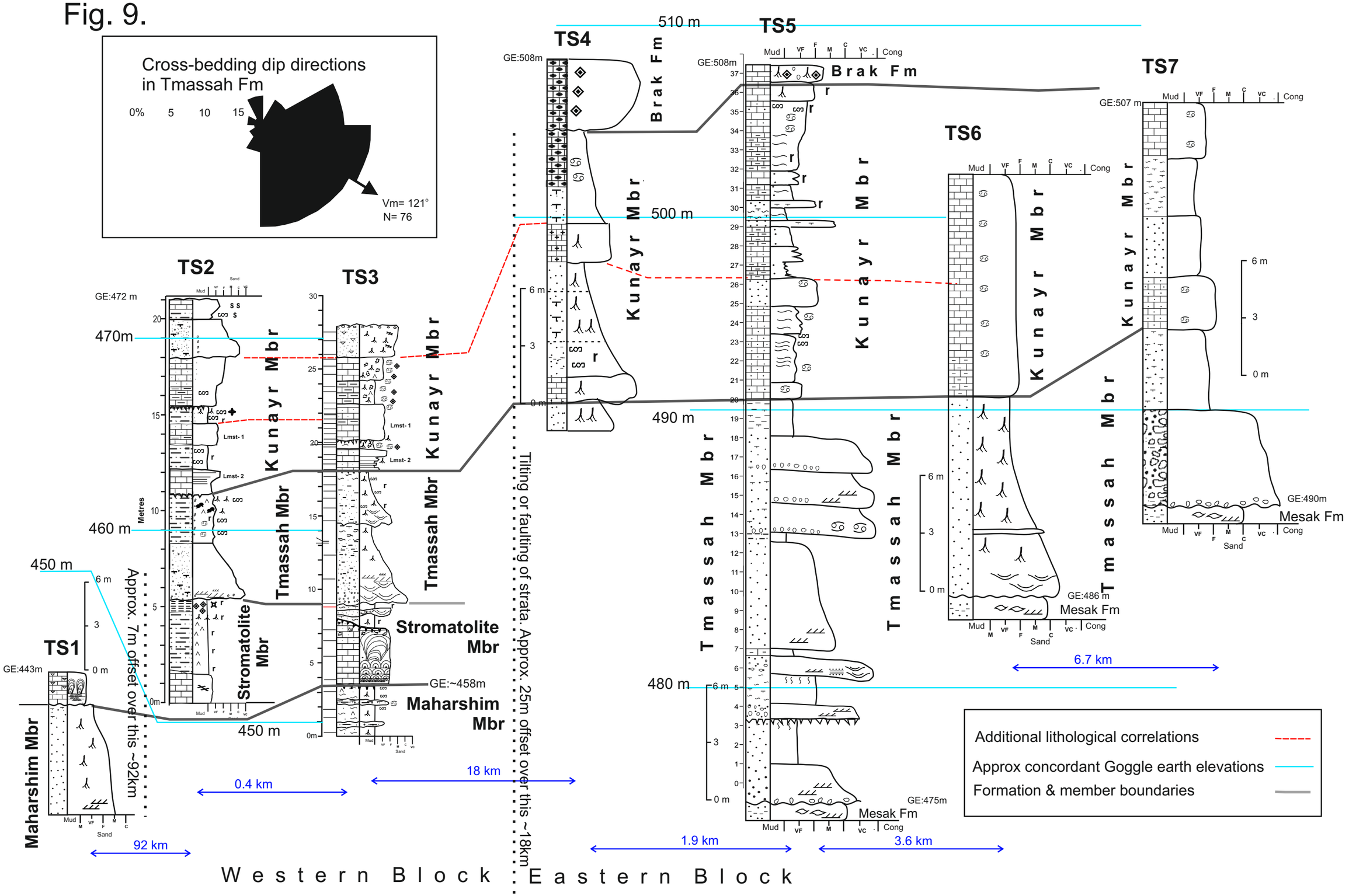
TS1
TS2
TS3
TS4
TS5
TS6
TS7
GE:443m
GE:472 m
GE:~458m
GE:508m
GE:508m
GE:486 m
GE:507 m
GE:490m
GE:475m
Mesak Fm
Brak Fm
Kunayr Mbr
Tmassah Mbr
Stromatolite Mbr
Maharshim Mbr
Lmst- 1
Lmst- 2
Mud
Sand
Cong
Metres
510 m
500 m
490 m
480 m
470m
460 m
450 m
450 m
6 m
3
0 m
Approx. 7m offset over this ~92km
Tilting or faulting of strata. Approx. 25m offset over this ~18km
92 km
0.4 km
18 km
1.9 km
3.6 km
6.7 km
Additional lithological correlations
Approx concordant Goggle earth elevations
Formation & member boundaries
Western Block
Eastern Block

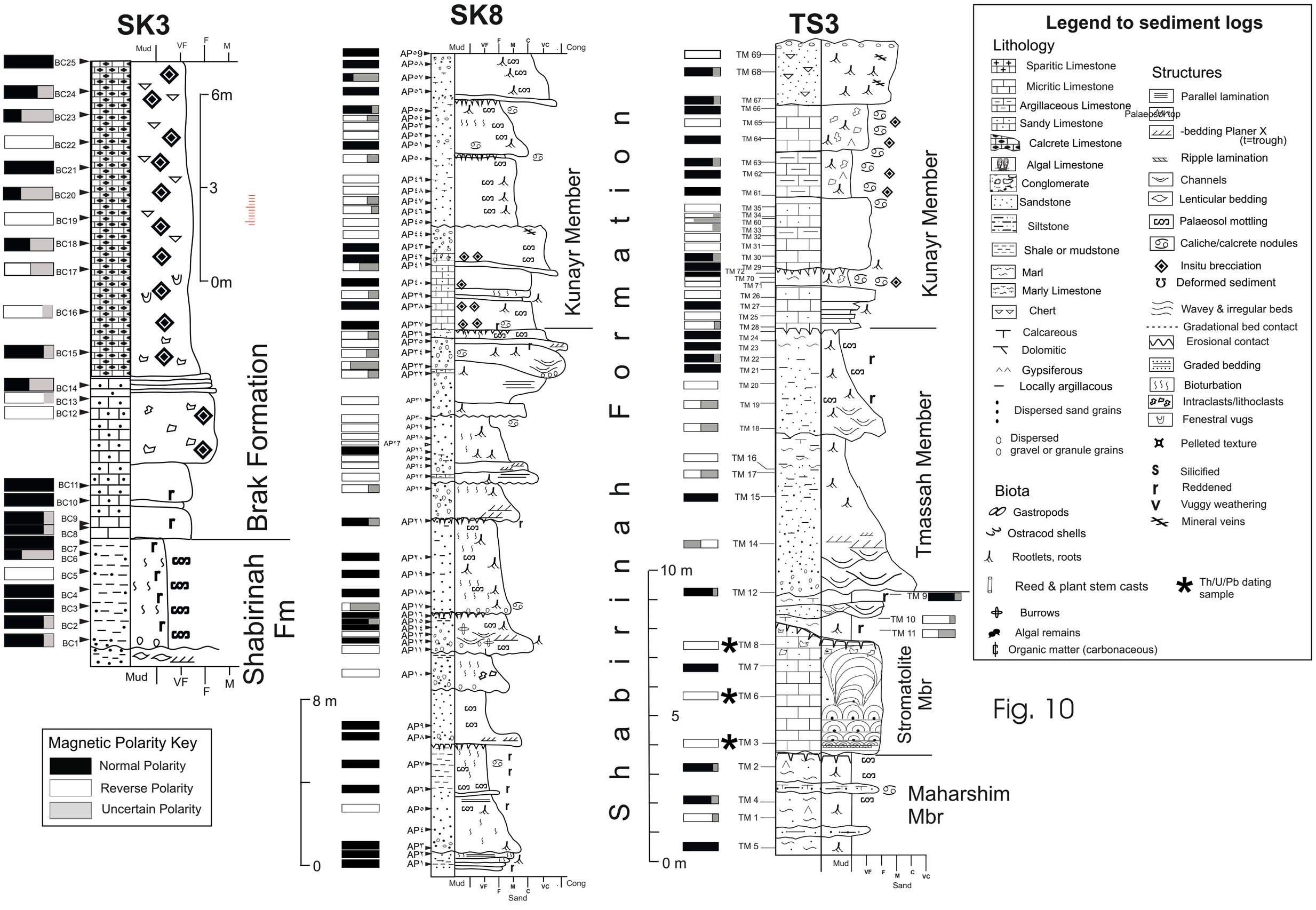
SK3
Mud
VF
F
M
6m
3
0m
BC25
BC24
BC23
BC22
BC21
BC20
BC19
BC18
BC17
BC16
BC15
BC14
BC13
BC12
BC11
BC10
BC9
BC8
BC7
BC6
BC5
BC4
BC3
BC2
BC1
r
Shabirinah Fm
Brak Formation
SK8
Mud
VF
F
M
C
VC
Cong
Kunayr Member
Kunayr Formation
8 m
0
Sand
TS3
TM 69
TM 68
TM 67
TM 66
TM 65
TM 64
TM 63
TM 62
TM 61
TM 35
TM 34
TM 60
TM 33
TM 32
TM 31
TM 30
TM 29
TM 72
TM 70
TM 71
TM 26
TM 27
TM 25
TM 28
TM 24
TM 23
TM 22
TM 21
TM 20
TM 19
TM 18
TM 16
TM 17
TM 15
TM 14
TM 12
TM 9
TM 10
TM 11
TM 8
TM 7
TM 6
TM 3
TM 2
TM 4
TM 1
TM 5
10 m
5
0 m
Shabirinah
Kunayr Member
Tmassah Member
Stromatolite Mbr
Maharshim Mbr
Mud
VF
F
M
C
VC
Sand
Magnetic Polarity Key
Normal Polarity
Reverse Polarity
Uncertain Polarity
Legend to sediment logs
Lithology
Sparitic Limestone
Micritic Limestone
Argillaceous Limestone
Sandy Limestone
Calcrete Limestone
Algal Limestone
Conglomerate
Sandstone
Siltstone
Shale or mudstone
Marl
Marly Limestone
Chert
Calcareous
Dolomitic
Gypsiferous
Locally argillacous
Dispersed sand grains
Dispersed gravel or granule grains
Biota
Gastropods
Ostracod shells
Rootlets, roots
Reed & plant stem casts
Burrows
Algal remains
Organic matter (carbonaceous)
Structures
Parallel lamination
Palaeosol top
-bedding Planer X (t=trough)
Ripple lamination
Channels
Lenticular bedding
Palaeosol mottling
Caliche/calcrete nodules
Insitu brecciation
Deformed sediment
Wavey & irregular beds
Gradational bed contact
Erosional contact
Graded bedding
Bioturbation
Intraclasts/lithoclasts
Fenestral vugs
Pelleted texture
S Silicified
r Reddened
v Vuggy weathering
Mineral veins
Th/U/Pb dating sample

Fig. 10

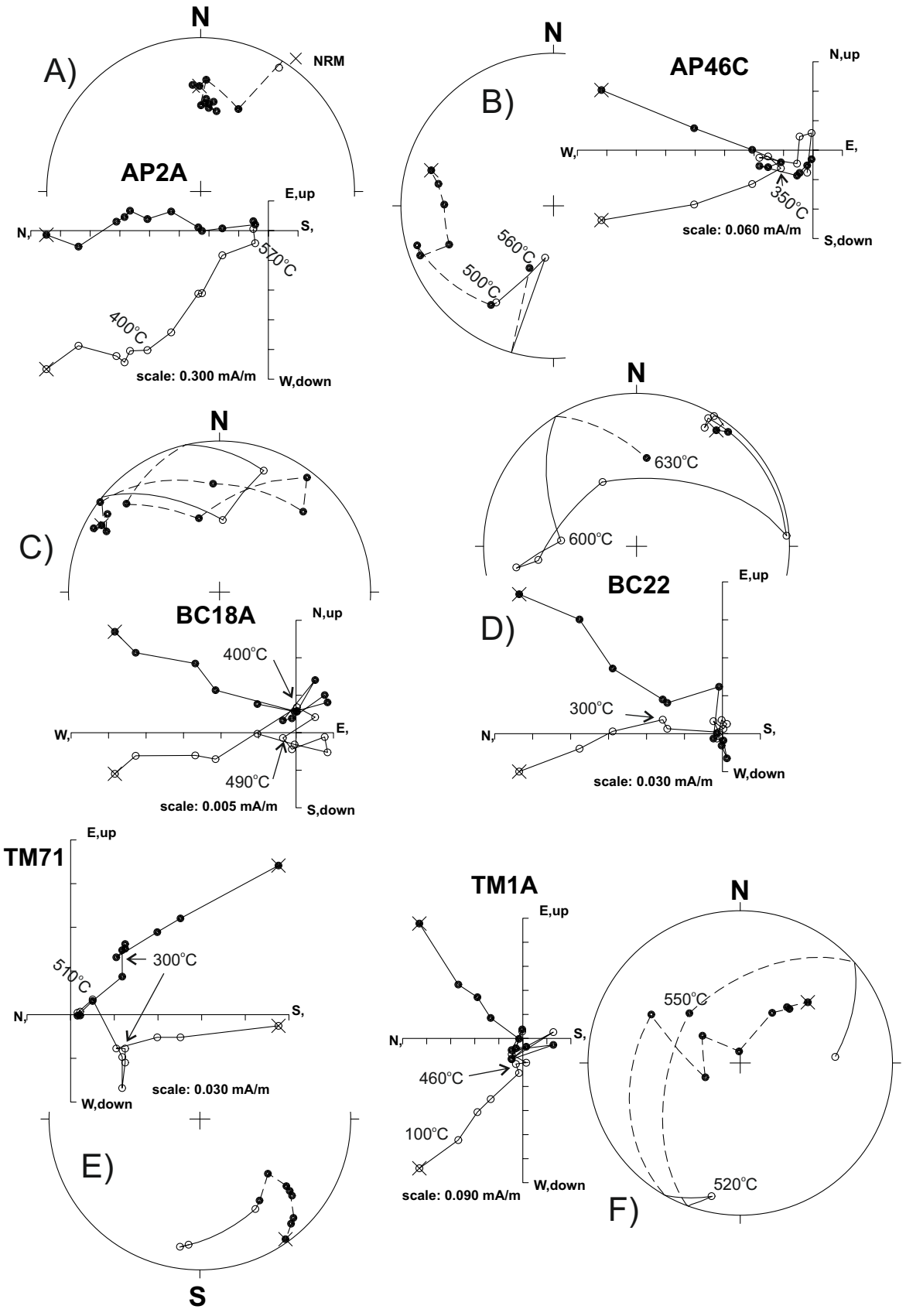
A)
N
NRM
AP2A
E,up
N,
S,
570°C
400°C
scale: 0.300 mA/m
W,down
B)
N
AP46C
N,up
W,
E,
350°C
scale: 0.060 mA/m
S,down
560°C
500°C
C)
N
BC18A
N,up
400°C
W,
E,
490°C
scale: 0.005 mA/m
S,down
D)
N
630°C
600°C
BC22
E,up
300°C
N,
S,
scale: 0.030 mA/m
W,down
TM71
E,up
510°C
300°C
N,
S,
scale: 0.030 mA/m
W,down
E)
S
TM1A
E,up
N,
S,
460°C
100°C
scale: 0.090 mA/m
W,down
N
550°C
520°C
F)

Fig. 11.

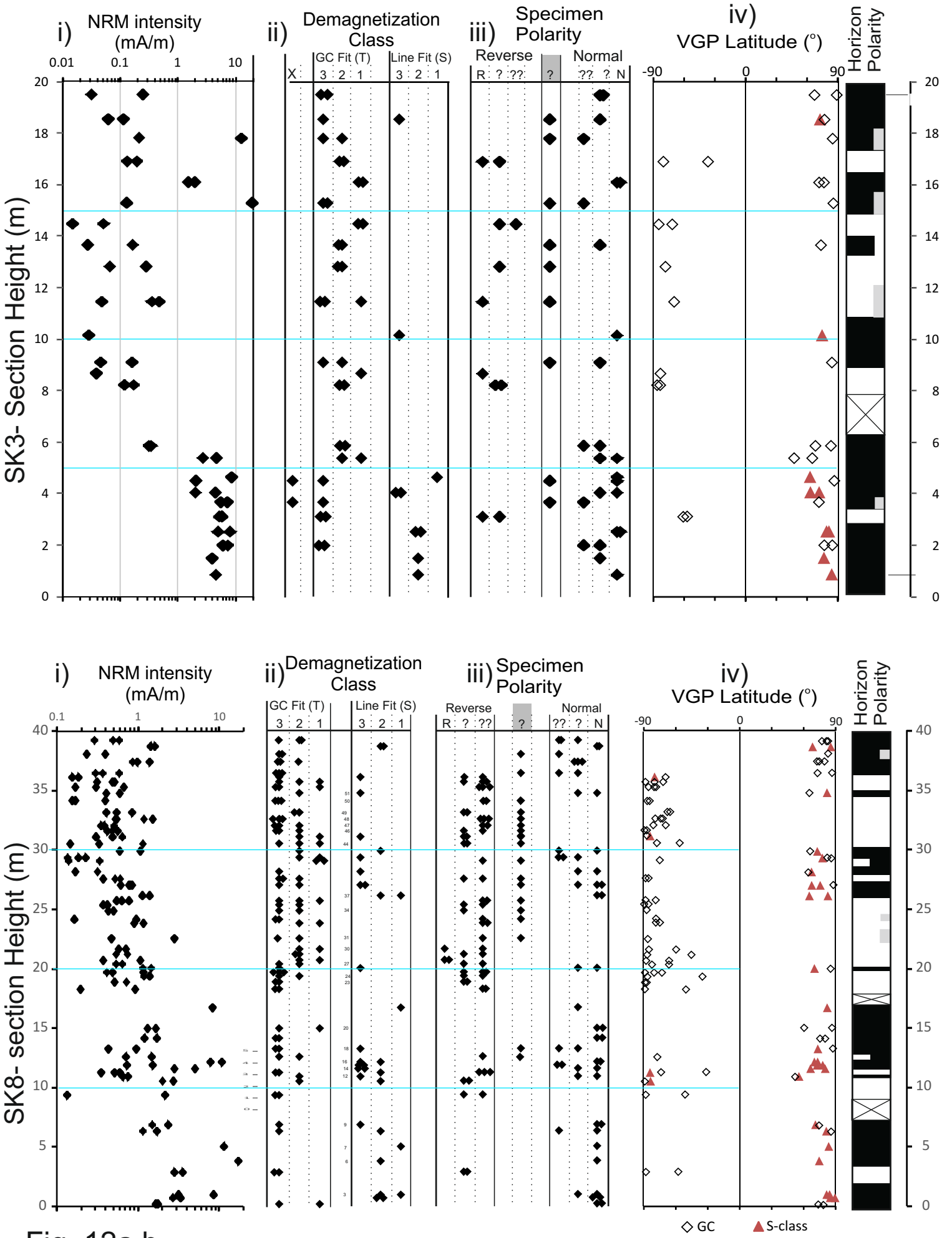
i) NRM intensity (mA/m)
0.01
0.1
1
10
ii) Demagnetization Class
GC Fit (T)
Line Fit (S)
X
3 2 1
3 2 1
iii) Specimen Polarity
Reverse
Normal
R ? ?? ? ?? ? N
iv) VGP Latitude (°)
-90
0
90
Horizon Polarity
SK3- Section Height (m)
0 2 4 6 8 10 12 14 16 18 20
i) NRM intensity (mA/m)
0.1
1
10
ii) Demagnetization Class
GC Fit (T)
Line Fit (S)
3 2 1
3 2 1
iii) Specimen Polarity
Reverse
Normal
R ? ?? ? ?? ? N
iv) VGP Latitude (°)
-90
0
90
Horizon Polarity
SK8- section Height (m)
0 5 10 15 20 25 30 35 40
GC
S-class

Fig. 12a,b.

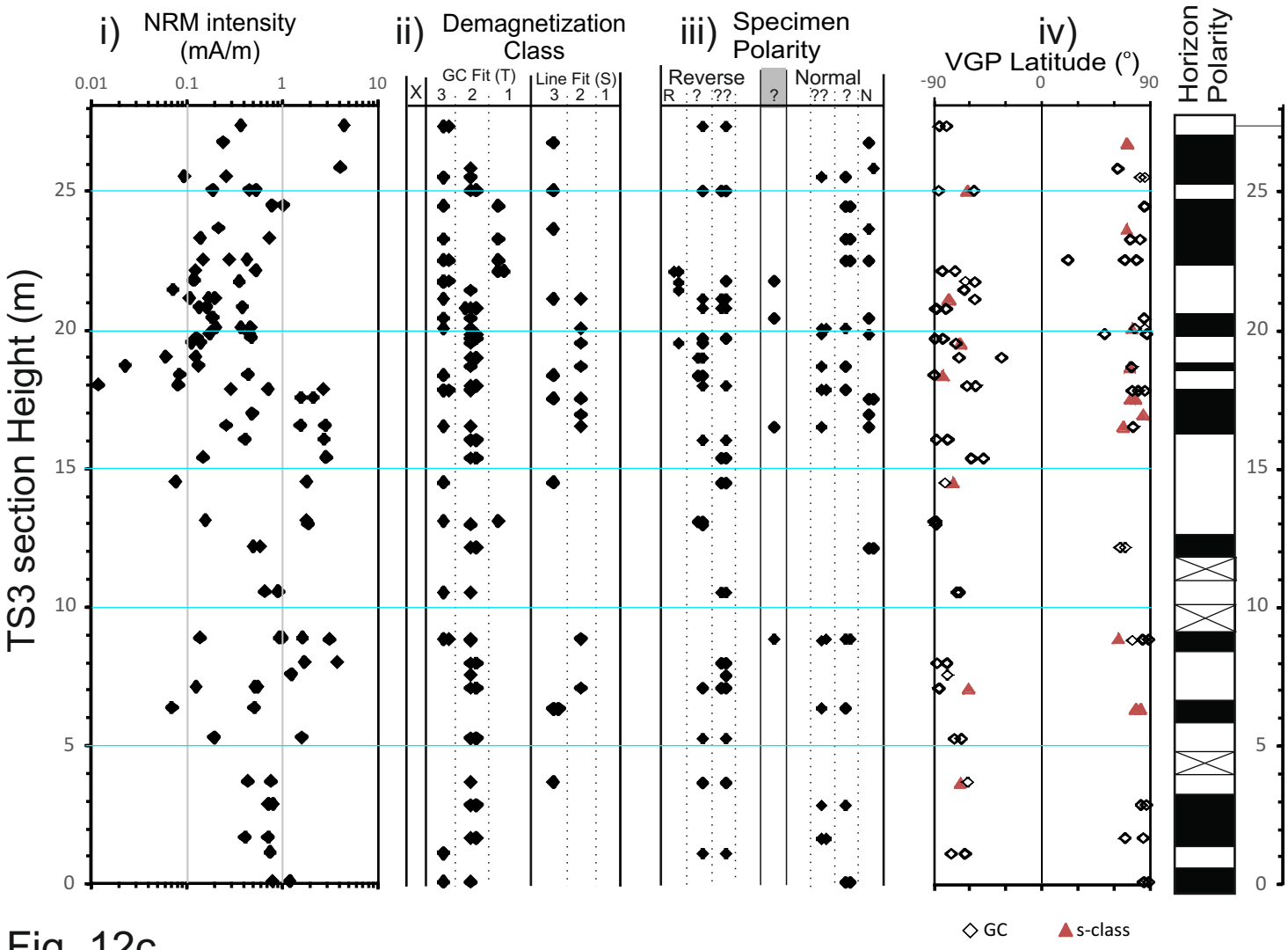
i) NRM intensity (mA/m)
0.01
0.1
1
10
ii) Demagnetization Class
X
GC Fit (T)
3 2 1
Line Fit (S)
3 2 1
iii) Specimen Polarity
Reverse
R ? ?? ?
Normal
?? ? N
iv) VGP Latitude (°)
-90
0
90
Horizon Polarity
TS3 section Height (m)
0
5
10
15
20
25
◇ GC
▲ s-class

Fig. 12c.

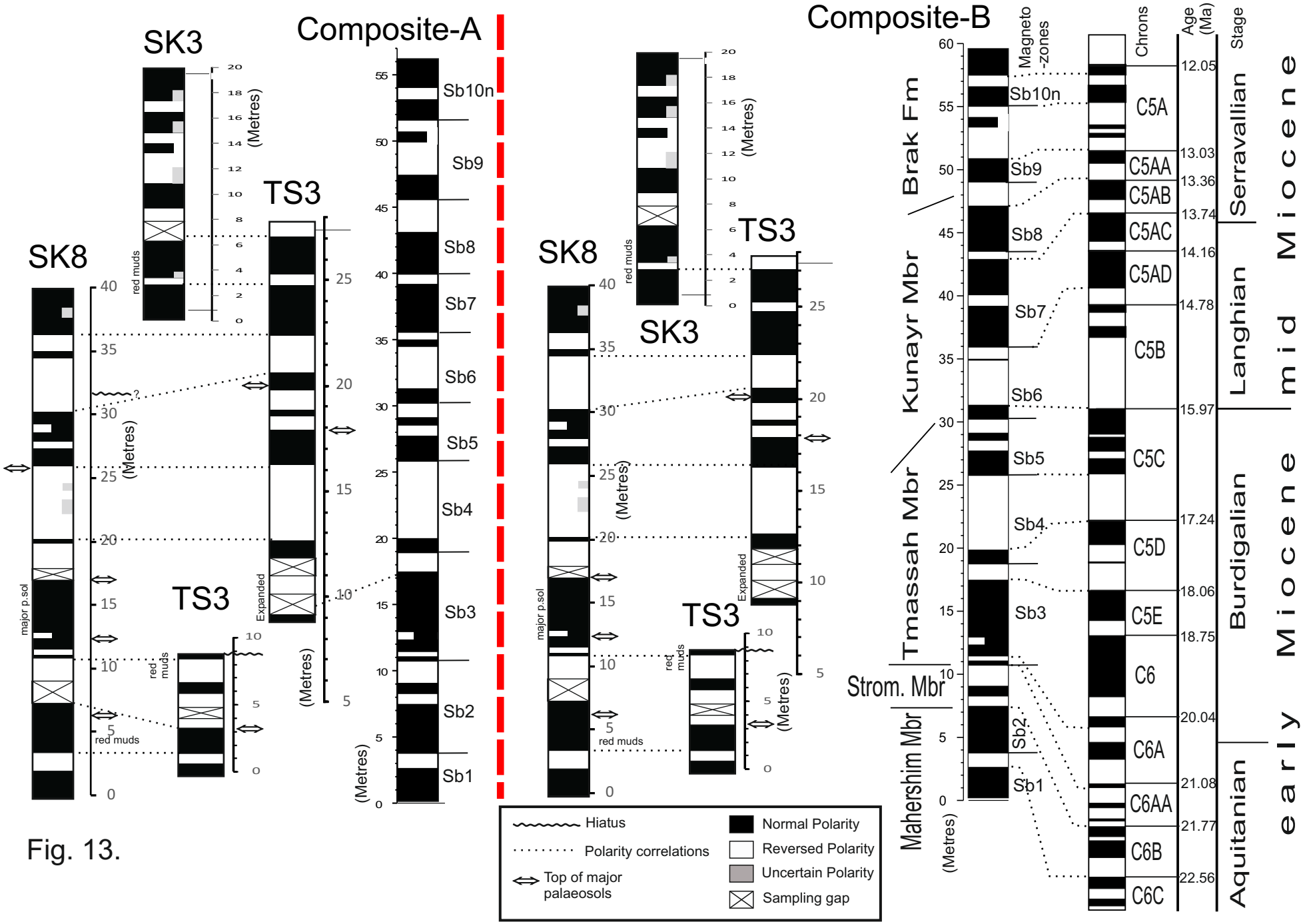
SK3
Composite-A
TS3
SK8
SK3
TS3
SK8
TS3
Composite-B
Sb10n
Sb9
Sb8
Sb7
Sb6
Sb5
Sb4
Sb3
Sb2
Sb1
(Metres)
red muds
major p.sol
Expanded
Hiatus
Polarity correlations
Top of major palaeosols
Normal Polarity
Reversed Polarity
Uncertain Polarity
Sampling gap
Brak Fm
Kunayr Mbr
Tmassah Mbr
Strom. Mbr
Mahershim Mbr
Magneto -zones
Chrons
Age (Ma)
Stage
C5A
C5AA
C5AB
C5AC
C5AD
C5B
C5C
C5D
C5E
C6
C6A
C6AA
C6B
C6C
12.05
13.03
13.36
13.74
14.16
14.78
15.97
17.24
18.06
18.75
20.04
21.08
21.77
22.56
Serravallian
Langhian
Burdigalian
Aquitanian
early Miocene
mid Miocene

Fig. 13.

Supplementary Information

Supplementary information includes:

1. **Part 1:** Formal definition of the new lithostratigraphy, illustrated with photos (SI Fig. S1) and detailed descriptions, tied to logs (Fig. S2). Locations of all sections discussed in this work are in SI Table S1, and listed in the google earth kmz file, with this supplementary information. Part 1 includes sedimentary logs and locations for the sections in the northern Awbari sand sea area, which help define the lithostratigraphy in the Zarzur Fm, but are not the main focus of this work (SI Figs. S3, S4).
2. **Part 2:** Additional magnetic data showing magnetic mineralogy data (SI Figs. S5, S6), nature of the magnetic overprints (SI Fig. S7), and the virtual geomagnetic pole data (SI Fig. S8).
3. **Part 3:** Methodology and results for attempted U-Th-Pb geochronology (SI Figs. S9 and Table S2).
4. **Part 4:** Additional figures and text which explain the alternative correlation models (SI Fig. S10) and discussion of the output from the sequence slotting procedures (SI Figs. S11, S12 and Table S3).

1. Description and type sections of the new lithostratigraphic units

We outline the sources for the naming of the lithostratigraphic units, and a brief lithologic description of the units, approach used to define bases and tops, and suggested type sections. We do not provide a comprehensive assessment here of late Quaternary-Holocene age units which belong to the Shati Formation, instead our focus here is largely the pre- late Quaternary units, particularly focussing on the Brak and Shabirinah formations. The Shati Formation units are described by Petit-Maire et al. (1980), Armitage et al. (2007) and Drake et al. (2006). Place name spellingsare taken from the IRC geology maps of Libya (Roncevic, 1984; Parizek et al., 1984; Berendeyev, 1985; Gundobin, 1985).

1.1 Al Mahruqah Group

We have upgraded the formation name, first used by Seidl and Röhlich (1984). They used Al Mahruqah to refer to the limestone units resting on basement on the northern side of Wadi ash Shati (i.e. our Brak Formation). Al Mahruqah is a village west of Brak, in Wadi ash Shati (Fig. 4).The name was later modified and expanded by Theidig et al. (2000) and Geyh and Theidig (2008) to include all the Miocene (?) and younger units on the fringes of the Awbari and Murzuq Sand Seas. We maintain this expansion of stratigraphic coverage, but upgrade the unit to group status to accommodate the new formations. Locations of all sections mentioned are detailed in Table S1.

1.2 Shabirinah Formation

Name from Wadi ash Shabirinah, the main E-W oriented wadi, east of Tmassah with extensive (over some 35 km distance) south-facing bluffs of the Shabirinah Formation on the North side of the wadi. Al Mahruqah Group sections in this area are also described by Koráb (1984). The formation is unfossiliferous except for ostracods seen in thin section in the limestone part of the Stromatolite Member.

Type sections: TS2 and nearby section TS3 (Fig. 6). TS5 is a good section which covers a larger stratigraphic thickness (Fig. 6) but it has no representatives of the Stromatolite or Maharshim members. An Al Mahruqah type section described by Koráb (1984) is present further south in the Wadi ash Shabirinah area and is there exposed in inselbergs. In both of the geological maps of the Wadi Kunayr and Wadi ash Shabirinah areas (Goudarzi, 1970; Koráb 1984; Wooler, 1984), this formation (and the Brak Formation) is erroneously combined with the late Cretaceous (Masstrictian) Bin Affin Member. However, both ourselves and Thedig et al.

Our field Seasons	Sect. ID	Location, Area	Palaeomag. sampled	Mbr/Fm present	Goggle Earth location	Ref. sources [Pmag code]
	Sk1	West of Al Mahruqah	no	Brak	27°, 29', 20"N; 13°, 51',6"E	G&T sites 5b,c,e; Abdullah (2010) site A
	Sk2	East of Al Mahruqah	no	Brak	27°, 31', 52"N; 14°, 4',9"E to 27°, 34', 60"N; 14°, 1',60"E	G&T site 6, Abdullah (2010) site B
2009	SK3	Quarry south of Al Marhruqah	yes	Brak, Shabirinah	27°, 30',20.1"N;14°, 04',5.0"E	Here, G&T site 6b,c; [BC]
2011	Sk4	Road side sections in Brak	no	Brak	27°, 31', 55.1"N;14°, 17',54.5"E	Here
	Sk5	Ashkidah	no	Brak	27°, 37', 22.0"N;14°, 31',59.5"E	Here
	Sk6	East of Ashkidah	no	Brak	27°, 38', 51.3"N;14°, 20',23.1"E	Abdullah (2010) site C, G&T site 7D
2005, 2009	Sk7	Lower part is cave in north Side of Wadi Kunayr	no	Kunayr, Shabirinah	27°, 40', 47.1"N;15°, 06',49.0"E	Here
2009	Sk8	North Side of Wadi Kunayr	yes	Kunayr, Shabirinah	27°, 40', 47.07"N;15°, 08',10.7"E	Here; [AP]
	Sk9	33 km NNE of SK8	no	Brak	27°, 55', 8"N;15°, 19',46"E	G&T site 8
2007,2011	SK10	Bir az Zallaf, Wadi ash Shati	yes	Bir az Zallaf, Sifar Top of Sayl	27°, 26', 0.9"N, 14°, 23',37.1"E to 27°, 26', 0.9"N, 14°, 23',37.1"E	Here and Abdullah (2010) section C, G&T?; [BZ,AL]
2011	SK11	Bir az Zallaf section in west side of hill. Sub-section to NE	yes	Bir az Zallaf, Sifar, top of Sayl	27°, 25', 47.5"N 14°, 23',12.2"E; to 27°, 25', 50"N; 14°, 23',15.7"E	Here;[BZ]
2007,2011	SK12	Washkat Zarzur, near Bir az Zallaf	yes	Sifar, top Sayl	27°, 24', 34.8"N;14°, 21',35.0"E	Here; [ALA, BZ]
2011	SK13	NW of Bir az Zallaf, Washkat Zarzur	yes	Aqar, Base of Sayl,	27°, 25', 29.09"N;14°, 20',54.2"E	Here; [BZ]
	NU1a	W. Awbari Sand Sea	no	Bir az Zallaf, Sifar	27°, 59', 21"N;10°, 49',49"E	Roncevic (1984), Fig.13
2008	NU1b	Al Kuthbanyar Ramliya, W Awbari Sand Sea	yes	Sifar	27°, 59', 47.9"N;10°, 50',12.5"E	Here [M,V]
2007,2008	NU1c	Al Kuthbanyar Ramliya, W Awbari Sand Sea	No	Bir az Zallaf, Sifar	27°, 59', 34.8"N;10°, 49',48.2"E	Here
	NU2a	Wadi Taharat, N. Awbari Sand Sea	no	Bir az Zallaf, Sifar	28°, 38',57.6"N; 11°, 21',13.07"E	Here

	NU2b	Wadi Taharat, N. Awbari Sand Sea	no	Nahiyah, Shabirinah(?)	28°, 41',1.2"N; 11°, 22',45.12"E	Here
	NU2c	Wadi Taharat, N. Awbari Sand Sea	no	Nahiyah, Sifar	28°, 42'N;11°, 12'E	Berandeyev (1985) fig. 14
2010	NU3a	Wadi as Sifar, N. Awbari Sand Sea	yes	Sifar, top Sayl	28°, 23',22.1"N;12°, 27',19.5"E	[QM2]
2010	NU3b	Wadi as Sifar, N. Awbari Sand Sea	yes	Bir az Zallaf, Sifar	28°, 23',5.42"N; 12°, 27',44.97"E	[QM5]
2010	NU3c	Wadi as Sifar, N. Awbari Sand Sea	yes	Bir az Zallaf, Sifar	28°, 22',51.7"N; 12°, 29',55.2"E	[QM4]
2010	NU3d	Wadi as Sifar, N. Awbari Sand Sea	yes	Bir az Zallaf, Sifar	28°, 24',29.3"N; 12°, 27',53.2"E	[QM3]
2008	NUS3e	Wadi as Sifar, N. Awbari Sand Sea	yes	Bir az Zallaf, Sifar	28°, 18',11.09"N; 12°,39',59.60"E	[QM1]
2009	TS1	Sarir al Qattusah, NW of Tmassah	No	Stromatolite, Maharshim	26°, 43',27.9"N; 15°, 36',40.1"E	Here
2009	TS2	N. side of Wadi Ash Shabirinah East of Tmassah	No	Kunayr, Tmassah, Stromatolite, Maharshim	26°30'51.90"N; 16°29'50.40"E	Here
2009	TS3	N. side of Wadi Ash Shabirinah East of Tmassah	yes	Kunayr, Tmassah, Stromatolite, Maharshim	26°,30',54.20"N; 16°,30',20.6"E to 26°,30',45.10"N; 16°,30',3.10"E	[TM]
2009	TS4	N. side of Wadi Ash Shabirinah East of Tmassah	No	Brak, Kunayr, Tmassah,	26°, 29',45.9"N; 16°, 40',37.5"E	Here
2009	TS5	N. side of Wadi Ash Shabirinah East of Tmassah	No	Brak, Kunayr, Tmassah,	26°, 29',25.6"N; 16°, 41',42.5"E	Here
2009	TS6	N. side of Wadi Ash Shabirinah East of Tmassah	No	Kunayr, Tmassah,	26°, 30',53.4"N; 16°, 43',5.1"E	Here
2009	TS7	N. side of Wadi Ash Shabirinah East of Tmassah	No	Brak?, Kunayr, Tmassah	26°, 32',59.1"N; 16°, 39',48.2"E	Here

Supplementary Table. S1. Locations of sections figured in this work, and sections mentioned in text, but not figured here. G&T= section location from Geyh and Theidig (2008).

(2000) consider the clastic units here to belong to the Al Mahruqah. In the Wadi Kunayr area the older geological map of Collomb (1961), like us, assigns these units to the Miocene, also associating them with units in Wadi ash Shati, that we now call the Al Mahruqah Group. The numerous magnetozones from these strata clearly show they are not Masstrictian in age, as the Masstrictian has a much simpler magnetic polarity pattern.

Age: Aquitanian to earliest Serravallian, chrons C6C to C5AAr

1.2.1 Maharshim Member

From the NNW-SSE oriented Wadi al Maharshim, 28 km to the NW of Tmassah (as marked on Tmassah Geology map). To the west and NW of this wadi there are good exposures of the lower two members of the Shabirinah Fm. Outcrops young towards the east in the Wadi al Maharshim to Tmassah area. This member can also be seen at section TS3 (SI Fig. S1B).

Base not seen. Top defined by base of overlying Stromatolitic Member (SI Fig. S1B). Thickness ~7 m or more (at section TS1, Fig. 6).

Description: Clastic unit with well-developed palaeosols, chalky groundwater calcretes, extensive rootleting and some cross-bedded sandstones.

Type section: *at TS1.*

Age: mid Aquitanian, chrons C6C to C6Bn.

1.2.2 Stromatolite Member

Name from the dramatic and distinctive stromatolite mounds which occur in the upper part of limestone bed that forms the lower part of this member (SI Fig. S1A, S1C). Theidig et al. (2000) has probably previously figured the stromatolites from the limestone unit in this member as their Plates 1e, 1f (and possibly Plate 5c), but assigned them to their 'Bir az Zallaf Member'

Base defined by the base of the distinctive white, stromatolitic limestone forming the lower part of this member (SI Fig. S1B). Top defined by base of overlying Tmassah Mbr (SI Fig. S1D). Thickness up to ~8 m at section TS2 and TS3.

Description: A lower white limestone unit, with weakly developed stromatolitic textures and occasional mounds on the upper surface, overlain by red, to locally green smectitic mudstones. The limestone bed locally displays large stromatolitic mounds on the upper surface (e.g. at 26°,31',47.9"N; 16°,24',31.7"E and 27°,26',2.8"N; 15°,34',15.6"E and 26°,30',55.3"N; 16°,31',57.6"E), when the overlying red mudstone is eroded. The mudstone displays extensive pedogenic mottling (Fig. S1D). The mudstone may contain sandstone beds. The limestone bed contains ostracods. In thin section the limestones are micritic, with scattered fragments of micritised ostracods. Textures are strongly peloidal.

Type section: TS3. Auxiliary sections occur in the vicinity of TS2 and TS5 and up to ca. 10 km to the east (Fig. 6).

Age: late Aquitanian, chrons C6AAr to C6Ar.

1.2.3 Tmassah Member

Name from the town south of Sabha. To the east of Tmassah scattered outcrops of the Tmassah Member occur (and other units of the Shabirinah Formation) as far east as the NE end of Wadi ash Shabirinah (Fig. S1E). The fluvial-dominated units below the Kunayr Member in the Wadi Kunayr area are also assigned to the Tmassah Member.

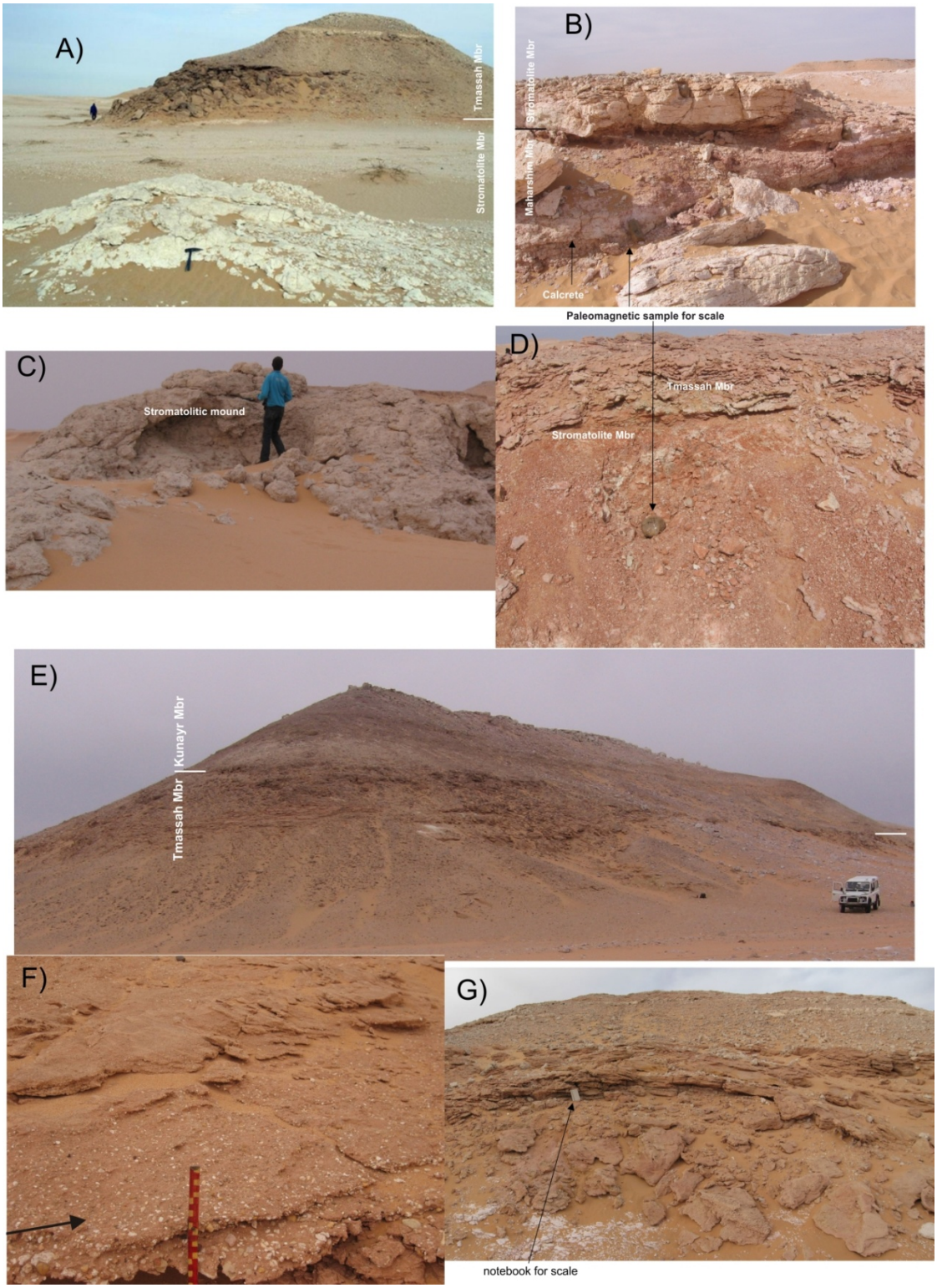

Fig. S1. Photographs illustrating the new lithostratigraphy, and key features of these units. A) Stromatolitic mound (in foreground) in the limestone part of the Stromatolite Member overlain by all the Tmassah Member in this small hill, which at this location is composed of coarse-grained cross bedded sandstone (section TS3). B) Base of the Stromatolite Member (white limestone in upper part of photo) overlying the mottled upper part of the Maharshim Member. The lower part of the outcrop shows a layer of calcrete (at ca. 2.5m in log in Fig. 6). C) Stromatolitic mounds in the top of the limestone bed In the Stromatolite Member ca. 9 Km west of section TS2 (Fig. 5). D) Base of the Tmassah Member (top of outcrop), overlying red mudstones forming the top of the Stromatolite Member (Section TS3). Sample TM10 is shown. E) Tmassah Member underlying the Kunayr Member at section TS5, in which the Kunayr Member has no well-bedded limestones, but is shown by the presence of rubbly calcrete nodules throughout. F) Pebbly sandstone in the base of the Tmassah Member (arrowed) , photo from near section TS2. G) Cross-bedding in the lower part of the Tmassah Member (scale shown by notebook), photo from section TS2.

Fig. S1. continued. H) View of the prominent limestone bed in the Kunayr Member (from section TS2), overlying the Tmassah Member in the lower part of the photo, with the upper-most part of the Kunayr Member shown in the distance. I) close-up of the heavily rootletted sandstone, and overlying darker, reddish palaeosol (top of photo). Height shown in photo ~ 2.5 m. J) The lower parts of the Shabirinah Formation in the SK8 section (Wadi Kunayr), showing the darker-coloured palaeosols behind the person, and the channellised nature of the sandstone bedies in the upper part of the section. Photo starts from the ca. 7 m level of the log in Fig. 10. K) Gypsum with chicken-wire texture in the top-most part of the Tmassah Member, immediately below the base of the Kunayr Member, section TS3. L) Desiccation cracks with upstanding ridges picked out by more carbonate-rich parts in a mudstone-rich layer in the lowest limestone in the Kunayr Member (section TS2). M) Termite burrow pod (adjacent to knife) in an extensively rootleted and burrowed silty sandstone in the Tmassah Member from section SK7.

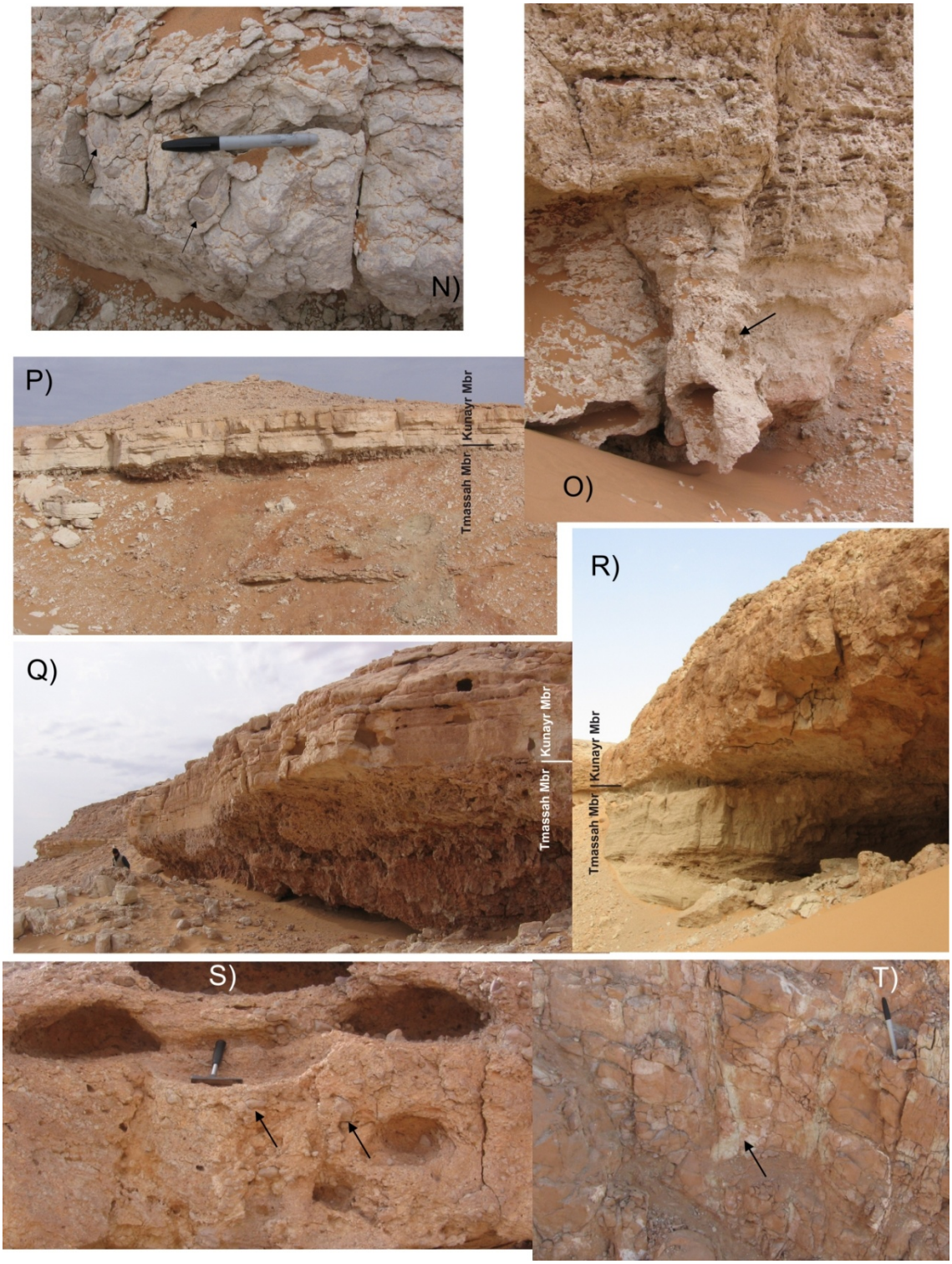

Fig. S1. continued. N) Pseudo-breccia developed in the base of the Kunayr Member ca. 100m east of the TS-5 section in the Wadi ash Shabirinah area (Fig. 6). O) A large rhizoconcretion (pen for scale) developed in the base of the Kunayr Member (ca. 200m east of the TS-5 section in the Wadi ash Shabirinah area; Fig. 6). P) upper-most clastic units of the Tmassah Member underlying the well-bedded lacustrine limestones in the base of the Kunayr Member (section TS3). Q) base of the Kunayr Member seen in the TS3 section in the Wadi ash Shabirinah area (Fig. 6), displaying the well-bedded lacustrine limestones, overlying the heavily rootleted top of the Tmassah Member. R) Base of the Kunayr Member in the Wadi Kunayr area in section SK-7 (Fig. 7), displaying heavily calcretised limestones overlying locally cross-bedded clastics. Section height shown ca. 10 m. T) red mottled mudstones from the upper most part of the Shabirinah Formation, in the lower part of section SK3 (Fig. 7). The mudstones display vertical mottling structures (arrowed) that may be ghosts of rootlet structures. S) Brak Formation in the Wadi ash Shabirinah area (some ca. 6.5 km NW of section TS7), displaying pseudo-breccia (arrowed) due to extensive calcretisation.

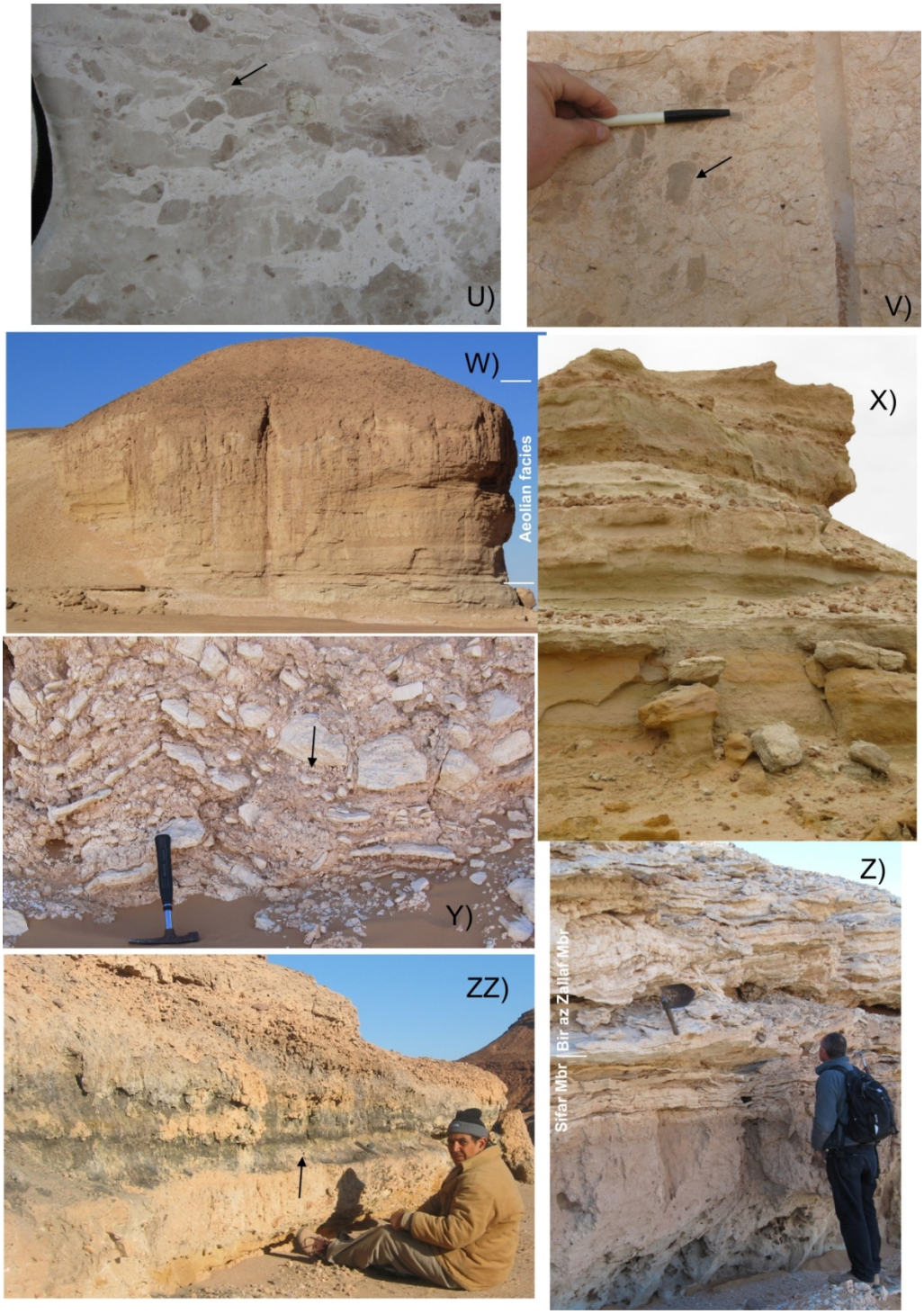

Fig. S1. continued. U) Pseudo- breccias with veinlets (arrowed), typical of the mid and upper parts of the Brak Formation, with several generations of cement, and colour density of breccias pods, probably related to the relative dolomite and silica content (on a polished block). V) Similar textures to U) seen in the type section, SK3 of the Brak Formation (near Al Marhuqah in Wadi ash Shati), in the quarried face. W) Aeolian cross-bedded facies of the Sifar Member in section NU3a, occupying the mid part of this cliff (shown on log in Fig. S4 starting in the photo at ca.6 m level). X) Typical outcrop of the Sifar Member of the Zarzur Formation, with harder more calcareous ribs of sandstone (sometimes gastropod or ostracods rich) interbedded with softer green and brown sandstones, mostly lacking sedimentary structures. Height of section ca. 17 m (section SK12), Washkat Zarzur near Bir az Zallaf. Y) Gypsum- facies in the Bir az Zallaf Member consisting of inter-bedded layers of gypsum (darker, arrowed) and micritic white limestone, in this case deformed by a tepee structure. Section NU3b Northern Awbari sand Sea (Fig. S3). Z) Typical limestone facies of the base of the Bir az Zallaf Member, consisting of laminated, crinkly-bedded limestones interbedded with friable sandstone and sandy limestone layers, resting on the underlying sandstones of the Sifar Member (Section NU3-d, Northern Awbari sand Sea; Fig. S3). ZZ) Outcrop of the Bir al Hasy Member of the Shati Formation, displaying typical fossil rich dark silts (arrowed) interbedded between fine-medium sand layer above and below. El Grafya 25 km east of Jarma.

Base defined by first major fluvial sandstone unit (often cross-bedded; Fig. 1G), erosively based (Fig. 1F), cutting into the underlying red mudstones of the Stromatolite Member (if underlying member is seen). Top defined by base of overlying Kunayr Member. Thickness up to ~21 m (at section TS5, SI Fig. S1E).

Description: Variety of fluvial clastics (SI Figs. S1F, S1G), often displaying well developed channel features (Fig. S1J) and cross bedding. Pebbly sandstone (Fig. S1F) to sandstone to sandy mudstone intervals. May contain dark humid palaeosol levels (SI Fig. S1I). May contain minor limestone intervals, and intervals of mudstone. Intervals may be reddened and contain pedogenic mottling. Finer grained sandstone to siltstone intervals may be heavily rootleted (SI Fig. S1I), these may be more frequent at basin margin locations (e.g. section TS-6, Fig. 6). In the Wadi Kunayr area termite- nests (Fig. S1M) occur like those described by Bown (1982). The boundary with the overlying Kunayr Member may show evidence of erosion, or more typically well-developed rootleting, and palaeosol development (SI Fig. S1K, S1O, S1Q). Away from basin-centre locations the lower part of the Tmassah Member probably laterally interdigitates with the Stromatolite and Maharshim members, to rest on basement. Thin sections show large well-rounded quartz clasts in a matrix of angular to sub-angular particles. Carbonate cements are similar to those in the Kunayr Member.

Type section: TS3, with auxiliary type section at TS5 (Fig. 6), where the Tmassah Member sits on basement.

Age: earliest Burdigalian to latest Burdigalian, chrons C6An.1n to C5Cn.

1.2.4 Kunayr Member

From Wadi Kunayr, east of Wadi ash Shati, an E-W oriented wadi with extensive outcrops on its northern flank of the Tmassah and Kunayr members (the wadi houses the irrigation circles of the Areal Agricultural Project).

Base defined by first major calcareous bed (palustrine limestone; SI Figs. S1P, S1Q, S1R) following the Tmassah Member clastics. Top defined by base of overlying Brak Formation. Thickness up to ~16m.

Description: Complex interdigitation of carbonates and clastics (SI Fig. S1H). Clastics may be of mixed lacustrine/fluvial/aeolian(?) origin (SI Fig. S1T). Carbonates range from variably calcretised palustrine limestones from thin to thick bedded, with pseudo-brecciated units (SI Fig. S1N) grading into nodular calcretes within the clastics. In the area east of Tmassah, the base may locally contain either a thickly-bedded, brecciated palustrine limestone (to east of section TS5, SI Fig. S1O, S1S), or laminated palustrine limestone's (e.g. sections TS2 and TS3, SI Figs. S1P, S1L). These represent lateral equivalents, with the more better developed palustrine limestone's closer to the basin centre to the west. Pedogenic mottling is common throughout the clastics, as is rootlet development at a variety of scales from small (mm) to big (metres). Locally with some levels of well developed palaeosols. May contain a massive, well-cemented, rootleted sandstone bed in its upper parts, in the Wadi ash Shabirinah area. The upper part of the member may laterally interdigitate with the Brak Formation. In thin section limestones tend to be more spar-rich than the Brak Fm, with complex cementation phases in heavily rootleted intervals. No fossils were seen at outcrop or in thin sections.

Type section: TS5 with auxiliary sections at SK8 and TS3 (Figs. 6,7). Section TS2 is re-drawn from that shown as Fig. 13 of Drake et al. (2008).

Age: latest Burdigalian to early Serravallian, chrons C5Cn to C5AAr.

1.3 Brak Formation

Upgraded from the 'Brak Member' used in some literature to refer to this dominantly carbonate unit (Theidig et al., 2000; Abdullah, 2010), with type area around Brak, and the Paleozoic basement outcrops on the north side of Wadi ash Shati. Formerly the "Calcari di Murzuch" (Murzuq Limestone; Desio, 1971) and the 'Al Mahruqah formation' of Seidl and Rohlich (1984). Theidig et al. (2000) suggested the Brak also occurs in the region Murzuq to Tmassah, although we have not seen these Brak Formation outcrops.

Base defined by well cemented, often fairly pure limestone, with main part of unit showing distinct brecciated texture (SI Figs. S1U, S1V). Top is a major unconformity surface, often heavily karstified (dolines locally important). Thickness variable, but up to 15 m is seen in Wadi ash Shati; although often thinner than this. Contact with underlying Shabirinah Formation seen in the area east and NE of Tmassah (Fig. 5), and inferred in the area north of Wadi Kunayr (Figs. 4, 8).

Description: Well cemented white dolomitic palustrine limestones, often massive and poorly bedded, and variably mottled on flat fresh surfaces (Figs S1U, S1V). Showing pedogenic brecciation with rare vadose vugs, reddish wispy clots, and occasionally with pisoids and oncoids (Plates 1g, 1h in Theidig et al., 2000). Often seen resting on heavily brecciated basement rocks in Wadi ash Shati area, which may be several metres thick (Plate 1b in Theidig et al., 2000). In Wadi ash Shati, Abdullah (2010) has described a deformed clastic rich unit at the base, which clearly rests on basement, which from his photographs appears to be heavy calcretised and brecciated basement rocks. The upper surface of the Brak Formation often forms extensive dolines and major karst surface features and plateaus, which are probably relict from the time of unconformity formation before deposition of the Zarzur Formation. The formation may contain minor interbedded siliciclastic units. No fossils have been seen in thin section or outcrop. In the type section, thin sections of the palustrine limestones are typically pedoidal with apparent intraclasts, occasional pisoids and coated grains, with multiple phases of cementation (Fig. S1U). More sparry cements occur as veins and veinlets. Frequency of spar cements and peloids increase up through the Brak Fm.

Type section: SK3, a location previously suggested by Theidig et al. (2000) and Geyh and Theidig (2008).

Age: early to late Serravallian, chrons C5AAr to C5An.

1.4 Zarzur Formation

Name from Washkat Zarzur region (marked on Sabha geology map), in which extensive outcrops of the Zarzur Formation occur in Wadi ash Shati, to the south of Brak.

Top defined by the youngest part of the Bir az Zallaf Member, which is normally a silicretised limestone on the plateau tops. Base defined by the unconformity on various underlying Mesozoic and Palaeozoic units. Unconformity may be marked by pedogenic structures such as mottling, and rootleting developed in the underlying unit (e.g. section SK12), a basal calcrete-rich palaeosol (section NU1b), conglomerate (e.g. section NU2b) or occasionally a sharp erosional boundary.

Type section: Bir az Zallaf, section SK10 to SK11 (Fig. 4), which cover the Bir az Zallaf Member. Auxiliary sections at SK12 and NU3a (Fig. S3).

Age: younger than Serravallian and older than 420 ka.

1.4.1 Sayl Member

Name from Wadi Sayl to the North of major Zarzur Formation outcrops in Wadi ash Shati, south of Brak (Fig. 4).

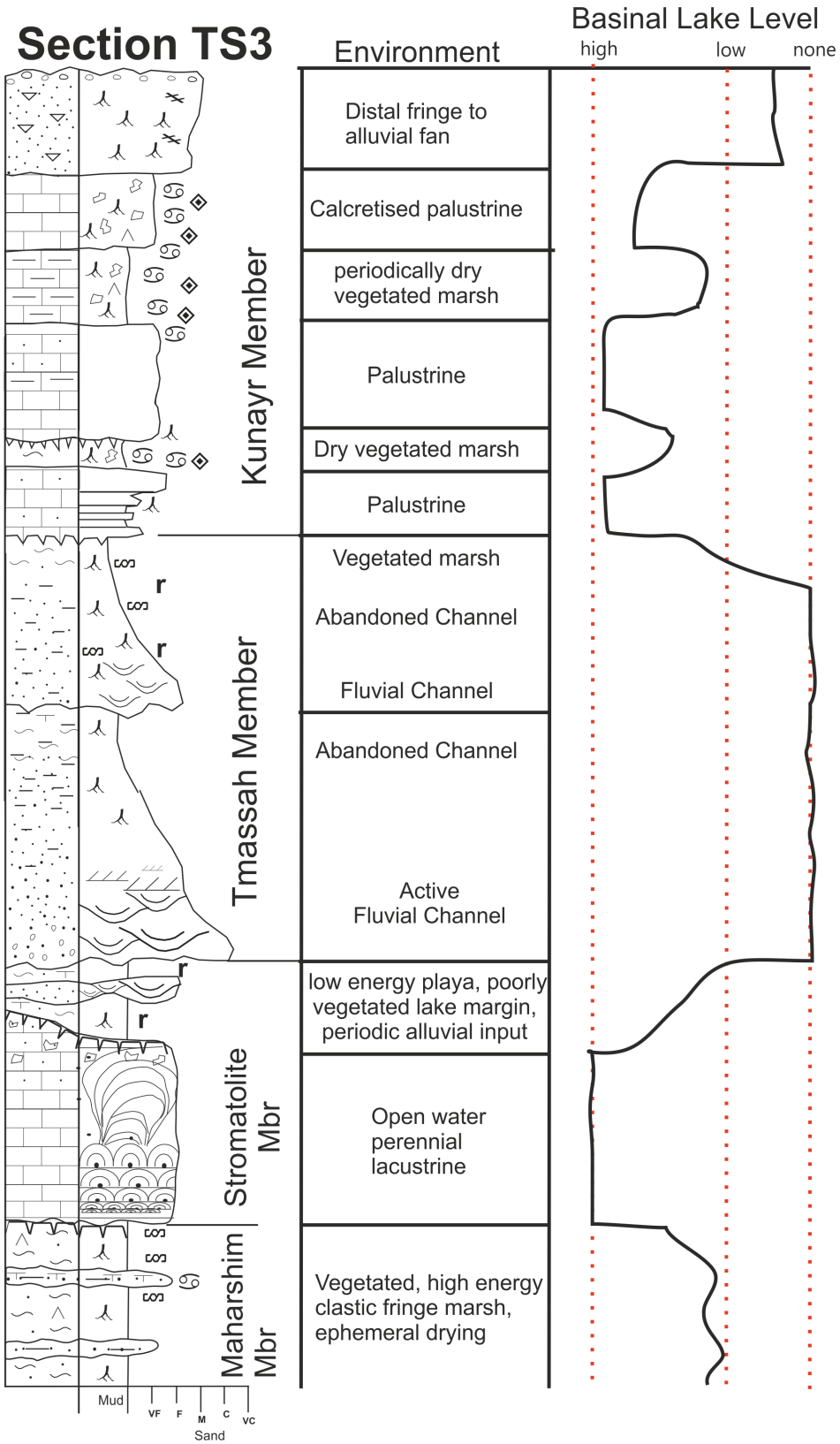

Fig. S2. Environmental model of the Shabirinah Formation, based on section TS3. The fluvial systems of the Tmassah Member probably bypassed or overrode the lacustrine system which developed during the Stromatolite Member. The low energy lacustrine system associated with the upper part of the Stromatolite Member was more saline than the palustrine systems of the Kunayr Member. The palustrine lake margin systems of the Kunayr and Maharshim members were more coarse-clastic dominated, and may have had an element of aeolian input in additional to the fluvial/alluvial inputs. The lake level interpretation assumes that a permanent lake (the main 'basin') existed W and SW of this section at all times, other than during the Tmassah Member.

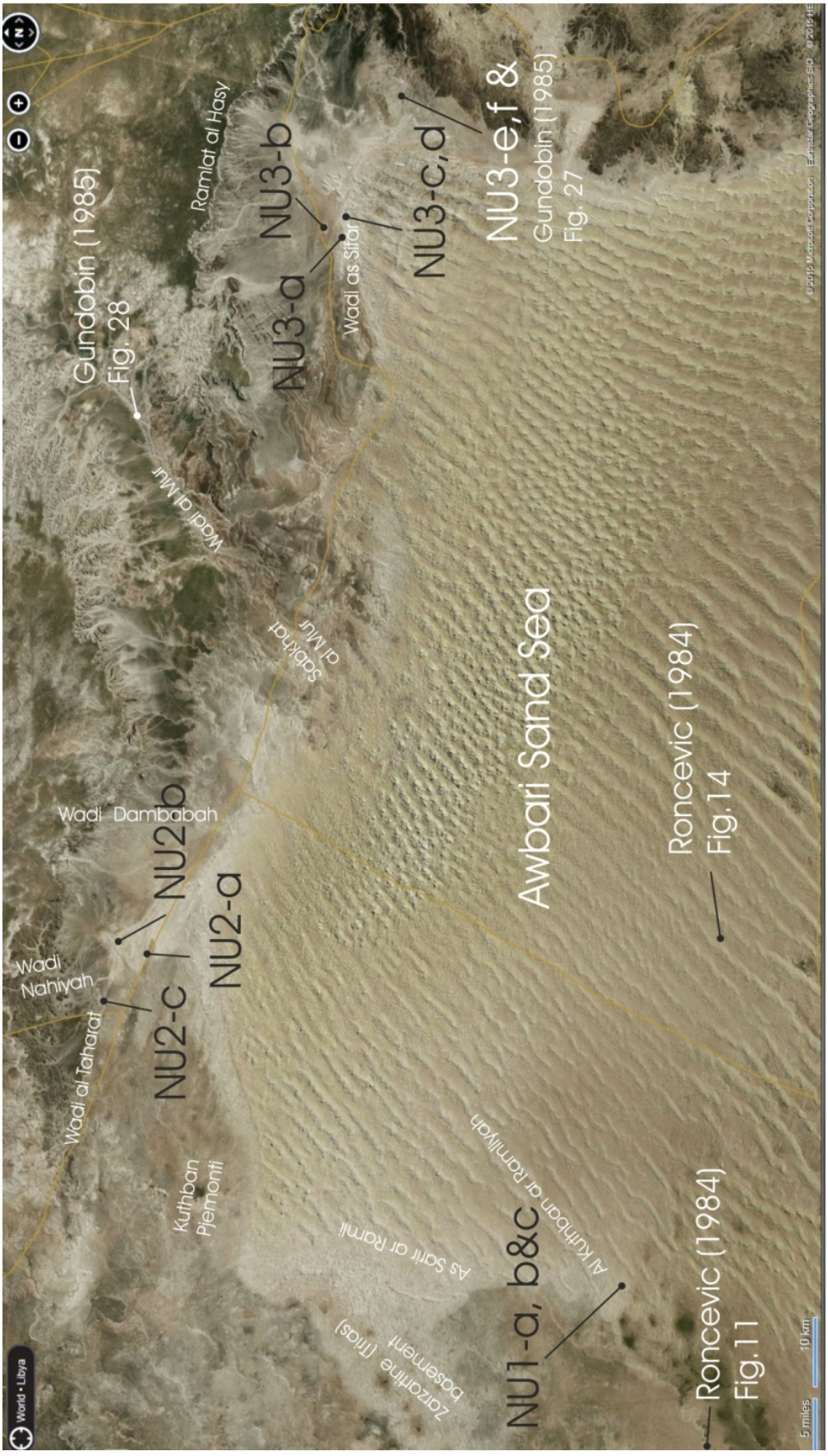

Fig. S3. The figured sections and locations in the northern Awbari Sand Sea, discussed in the supplementary information. Image from www.bing.co.uk.

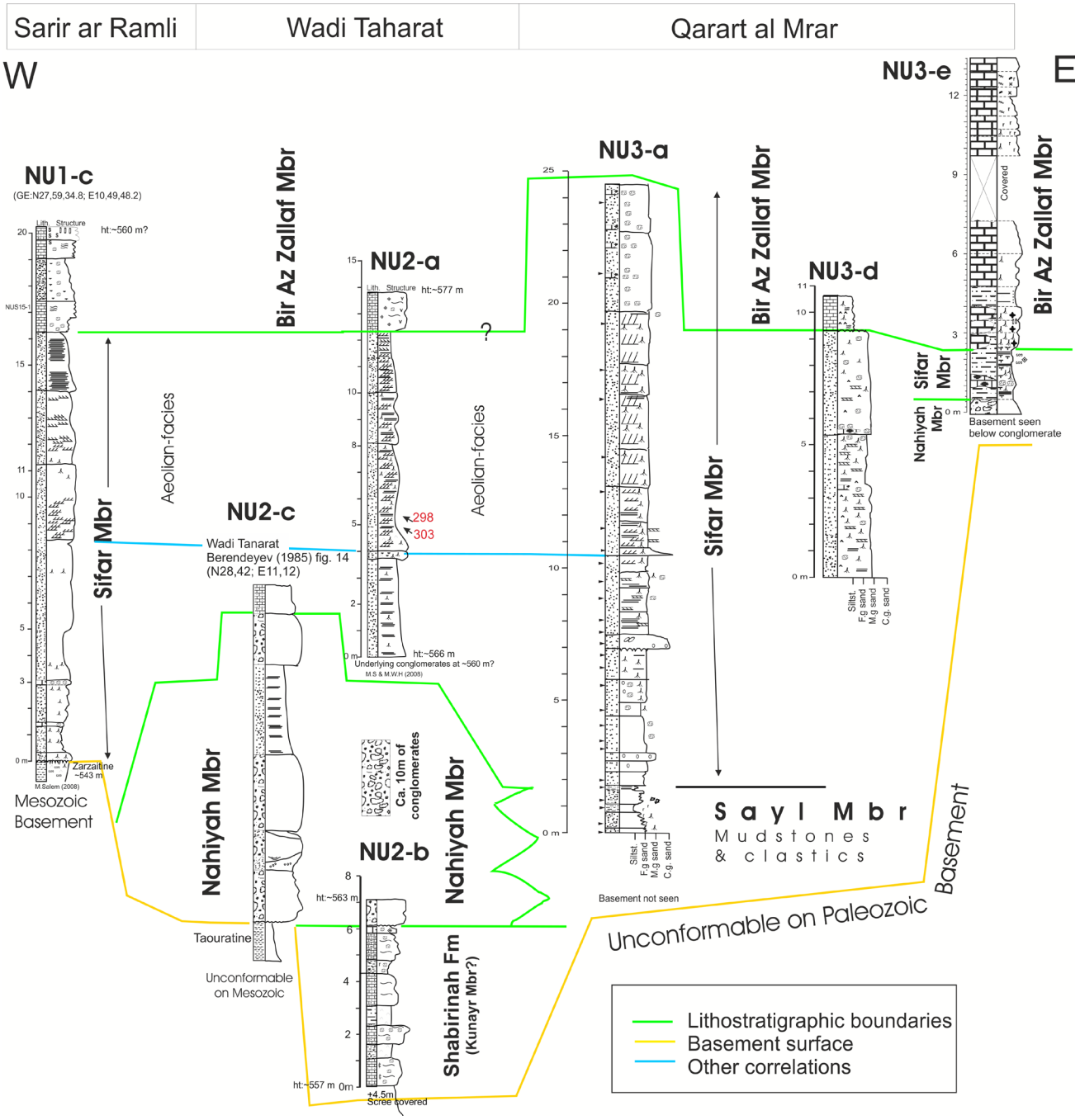

Fig. S4. Schematic relationships of Northen Awbari Sand Sea sections, mostly in the Zarzur Formation (location code=NU). See Fig. S1 and Table S3 for locations. Cross bedding directions shown in red. Section NU2-c is redrawn from Berendeyev (1985), all others from this study.

Top defined by first incoming of major mudstone units in the lower parts of the Zarzur Formation (Fig. S4). Base when seen is base of Zarzur Formation. Thickness of the order of 10-12m at Bir az Zallaf.

Description: Interbedded grey to green to rare red mudstones and fine to course sandstones. No complete section has been seen, since in Wadi ash Shati the Aqar Member cuts into this unit. Of fluvial-lacustrine origin.

Type section: One not seen. There may be one west of Bir az Zallaf or at or slightly west or SW of location 28,23,48.6N; 12,26,27.9E; SK12, SK13 include upper and lower boundaries of this member respectively (Fig. 4).

Age: Younger than Serravallian and older than 420ka.

1.4.2 Nahiyah Member

Region and named well on south side of Wadi Taharat (SI Fig. S1), with good exposures of the Nahiyah Member conglomerate, and its contact with the underlying Shabirinah Formation, and overlying exposures of the Sifar Member (Fig. S4).

Top defined by last conglomerate bed. Base is base of Zarzur Formation. Thickness about 10-15 m.

Description: Assorted clast-supported conglomerates with interbedded sandstone layers, with clasts derived from the underlying basement units (Fig. S4). Clasts of black chertified wood common in the Hamadat Tanghirt region.

Type section: No complete section seen, but upper and lower boundaries of this unit seen at sections NU2a and Nu2b. Member is exposed along the escarpment ca. 2 km to the NW and 2 to 5 km to the ESE from NU2a. Berendeyev (1985) has also figured (his Fig. 14) a similar section (NU2c; SI Fig.S4), which may equate with this unit, and could serve as a type section.

Age: Younger than Serravallian and older than 420 ka.

1.4.3 Sifar Member

Origin of name is Wadi as Sifar marked on geology map to the south of major outcrops in the Qararat al Marar area (N. Awbari Sand Sea) in which major well exposed outcrops of the Zarzur Formation occur (SI Fig. S3).

Top and based defined by overlying member units. Up to 22 m thick.

Description: Well sorted sandstone, fine to coarse grained, occasionally pebbly, often rootleted or with other bioturbation structures destroying most original sedimentary structures. Rootlets may be preserved as gypsum casts. Rootleting systems may be several metres long vertically. Parts may be cross-bedded and or well laminated, if rootleting is not too severe. Large-scale aeolian cross-bedding more common in its upper parts (Fig. S1W). May contain nodular or groundwater chalky calcretes, or impersistant layers of ostracod or gastropod rich sandstone (as in Wadi ash Shati; Fig. S1X). Of mixed fluvial (lower parts) to aeolian origin in upper parts. Often seen in contact with basement at off-basin centre locations. In thin section the sandstones are quartz-rich with minor feldspar, containing well rounded larger grains within a matrix of sub-angular smaller sand particles. Fossiliferous horizons of ostracods and gastropods and may contain rare ooids and coated grains. Less consolidated intervals are cemented by micritic rims, and chalky calcrete horizons (in western Ubari Sand Sea area) are composed of dense micrite.

Type section: NU3a (SI Fig. S3, S1W), with auxiliary section at SK12 (Fig. S4).

Age: younger than Serravallian and older than 420ka.

1.4.4 Bir az Zallaf Member

Name from the prominent inselberg south of Brak. A prominent limestone bearing unit at the top of the Zarzur Formation (SI Figs. S1Y, S1Z). A similar usage was largely implied by Theidig et al. (2000) and Geyh and Theidig (2008), since their focus was on the carbonate units, largely ignoring the dominant underlying siliciclastic units, which make up 90% of the Zarzur Formation.

Base defined by the oldest major laminated limestone unit. Up to 6.5m thick

Description: Interbedded laminated limestones (Plates 3c, 3d in Theidig et al., 2000), and green or orange rootleted sandstones (Fig. 2 in Armitage et al., 2007). Sandstones are often poorly consolidated. Limestones typically have undulose bedding, and may show sharp, erosional contact onto the underlying sandstone. Limestones may contain ostracods, fossil fish, fossillised phragmites, or tepee structures (SI Fig. S1Y) or interbedded gypsum (Plates 3e, 3f in Theidig et al., 2000). Limestone's may grade laterally into nodular palustrine limestones or rarely nodular calcretes. Massive calcrete beds, having brecciated texture may occur where this unit sits on basement (e.g. section NU3e; Fig. S4), or at basin margin locations. In thin sections, limestones tend to be Fe-poor micrites, with occasional ostracods, peloidal intervals and intraclasts. At basin margin sections (e.g. NU3e) calcretisation has produced heavily micritised fossils (ostracods, algal fragments) in peloidal palustrine limestones, with sparry cements.

Type section: SK10 with auxiliary section at NU3c (SI Fig. S1Z). SK10 is the same type area (their site 2b) as proposed by Geyh and Thiedig (2008).

Age: *Pliocene(?) to possibly as young as 420 ± 37 ka (sample FZ5 in sand near the top of member; Armitage et al., 2007) . Other OSL dated samples from this member were all saturated, casting some doubt on the reliability of the one near-saturated OSL date. Dating of the limestone beds using ^{230}Th/U suggests ages of 206-259 ka (Geyh and Thiedig, 2008) in conflict with the OSL date.*

1.5 Shati Formation

Named after Wadi ash Shati in which this formation has many small outcrops (Drake et al., 2006) of Quaternary-Holocene lake deposits.

Base defined by unconformity onto various Palaeozoic strata and Zarzur Formation in Wadi ash Shati and Qararat al Marar (Fig. 9). Top defined by overlying modern dune sands, Wadi deposits and interdune lake deposits.

Description: Includes various deposits including shell rich deposits (Aqar Member) to gastropod rich silts and mudstones, sometime organic rich (Bir al Hasy Member) to various kinds of sandy and pebbly-sand deposits, some of which may be fluvial in origin (and contain bivalves) and probably some units may be aeolian.

Age: In Wadi ash Shati 150 ka (from uranium-series dates from the Aqar M Member; Petit Maire et al., 1980) to 6 ka from OSL dates (Armitage et al., 2007; Drake, et al., 2006). In Wadi al Ajal the lacustrine units range in age down to ca. 250 ka (Drake et al., 2006).

1.5.1 Aqar Member:

Already, widely used in the literature derived from Petit-Maire et al. (1980), described in detail by them and Theidig et al. (2000), Geyh and Theidig (2008).

Description: Cross-bedded, shell-rich shore line deposit, often interbedded with variable amounts of sandstone (see Plates 4a to 4d, 2c in Theidig et al., 2000, Fig. 3 in Armitage et al., 2007).

Type section: 10 km east of Quttah and 0.6km south of the main road (27°28',40"N; 13°53'10"E, sample locality Xv of Petit-Maire, 1982), as suggested by Theidig et al. (2000). Additional auxiliary sections at 27°31',26"N; 14°06'08"E and 27°29'30"N; 14°00'39"E as suggested by Petit Maire et al. (1980) and Geyh and Thiedig (2008).

Age: OSL dates give ages 97.7 ± 6.5ka to 108 ±9 ka (Armitage et al., 2007). TIMS uranium-series dates suggest an age of 128 ka (Thiedig et al., 2000) to ~135 ka from 21 uranium-series ages obtained by Petit-Maire et al. (1980) using shells from the coquina. ^{230}Th/U dates from the Aqar Member suggest median ages of 136 ± 5ka (Geyh and Theidig, 2008).

1.5.2 Bir al Hasy Member :

From a well near the Qararat al Marar NU3-e section (Fig. S3). Section NU3-e shows excellent exposures of fossil-rich mudstones and siltstones resting unconformably on the upper parts of the Zarzur Formation. Gundobin (1985) has this area figured in his Fig. 27, but their description and interpretation is erroneous. He failed to recognise the significant topography on the basal unconformity of the Shati Formation at this location, in which fragments of the gastropod-bearing Bir al Hasy Member are spread-out down the wadi, on top of the Zarzur Formation, filling shallow depressions and cracks in the underlying unit. Hence, Gundobin's Fig. 27 log, is a random mix of the two formations. Some of the other map sheets in the northern Awbari Sand Sea area have used Gundobin's Fig. 27 as a kind of type-section to infer fossil-content into Zarzur Formation type units further west, which is again erroneous, since the visibly abundant gastropods occur in the overlying Bir al Hasy Member only. In this immediate area, the Bir al Hasy Member locally has a conglomerate at its base.

Description: Dark coloured silts and mudstones containing gastropods (*Melanoides* sp., *Bulinus* sp.), locally with sandy or gravelly interbeds (SI Fig. S1ZZ). Poorly consolidated. Described also by White et al. (2000, 2006) and Drake et al. (2006) from Wadi al Ajal, and Petit Maire et al. (1980) from Wadi ash Shati.

***Type section**: NU3f (28°,18',16.62"N; 12°,40',22.2""E). Auxiliary key location at el Ghrayfah 25 km east of Awbari (Fig. S1ZZ and Plate 5b in Theidig et al., 2000), dated by Armitage et al. (2007) to 53 ±6.3ka to 11 ka.*

***Age:** OSL dates from 52.8 ± 6.3 ka at the base to as young as 9.2 ± 0.6ka (Brooks et al., 2003; Armitage et al., 2007). Older in Wadi al Ajal (Drake et al., 2006).*

1.6 Comments about other proposed lithostratigraphic units

Geyh and Theidig (2008) have described the Antalkhata Member from outcrops in the Awbari Sand Sea. We have not seen the location figured by them, but have seen similar outcrops in interdune depressions which we have considered to be Holocene or late Quaternary interdune lake deposits, composed of limestones, that are typically fossil-rich, and occasionally stromatolitic. The fossil rich nature of their unit is unlike the Shabirinah Formation, but much more like a unit of the Shati Formation, so we consider their Antalkhata member to be likely younger than the Brak Formation.

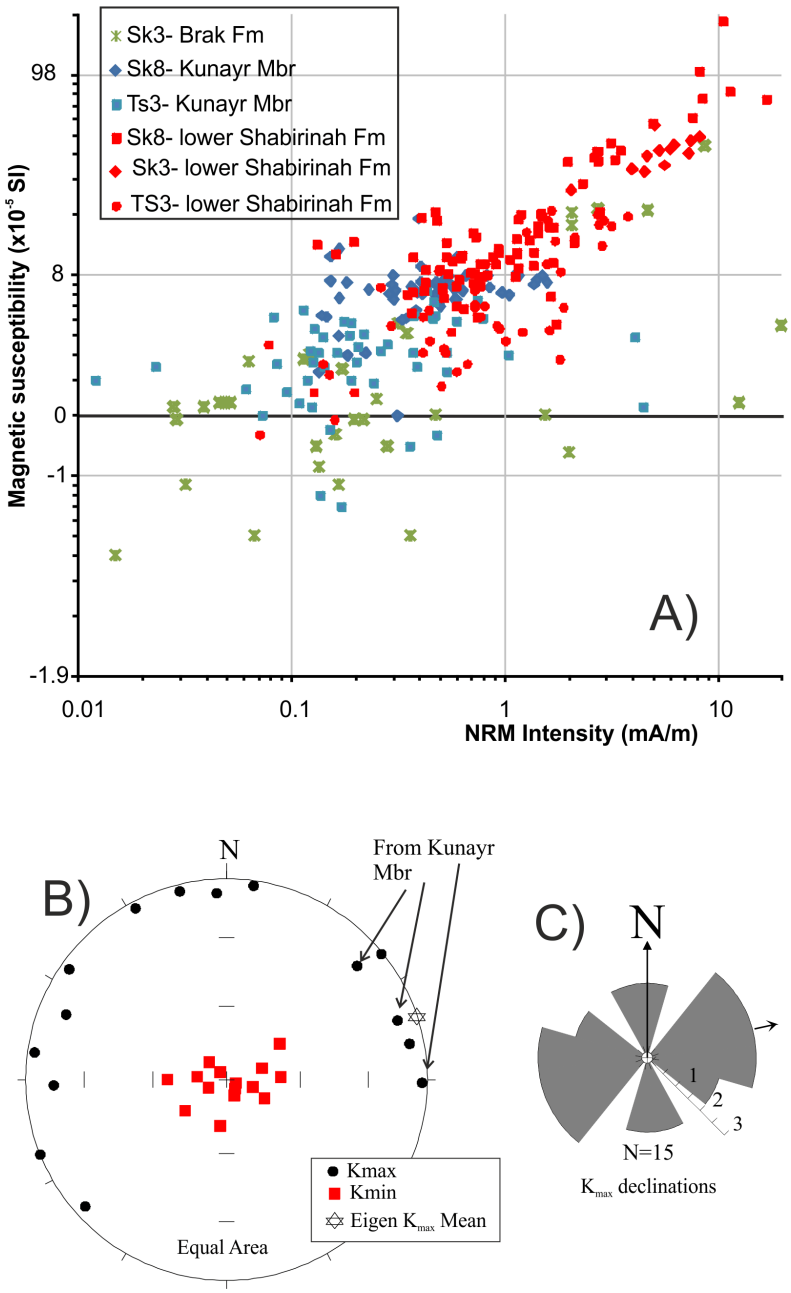

Fig. S5. a) NRM intensity and magnetic susceptibility of all specimens from the Shabirinah and Brak formations (magnetic susceptibility values have 2.0 added to value to plot on the log scale). B), C) Anisotropy of magnetic susceptibility of specimens from the SK8 section, with shown in C), the declinations of the K_{max} axes (reflected about 0-180^{o}), and mean direction indicated with an arrow (all specimens from Tmassah Member, except three specimens from the Kunayr Member, indicated by their flagged K_{max} directions in B).

2. Additional magnetic data

The natural remanence intensity and magnetic susceptibility are strongly related to the lithology and formations, with much of this variation controlled by either the carbonate content, or the degree of reddening (Fig. S5a). The anisotropy of magnetic susceptibility of specimens displays a depositional fabric (Fig S5B), with the Kmax axes appearing to reflect paleocurrent orientations (Fig. S5C). Rock magnetic data indicates both magnetite and haematite as the source of the ferromagnetic properties (Fig. S6), likely contributing to the rather complex palaeomagnetic behaviour of these samples (Fig S7). Existing paleopole data for the African Miocene is very scattered (Fig. S8), but our data is rather more tightly grouped along the 0-30 Ma segment of the African apparent polar wander path, which shows relatively little movement in the last 50 Ma.

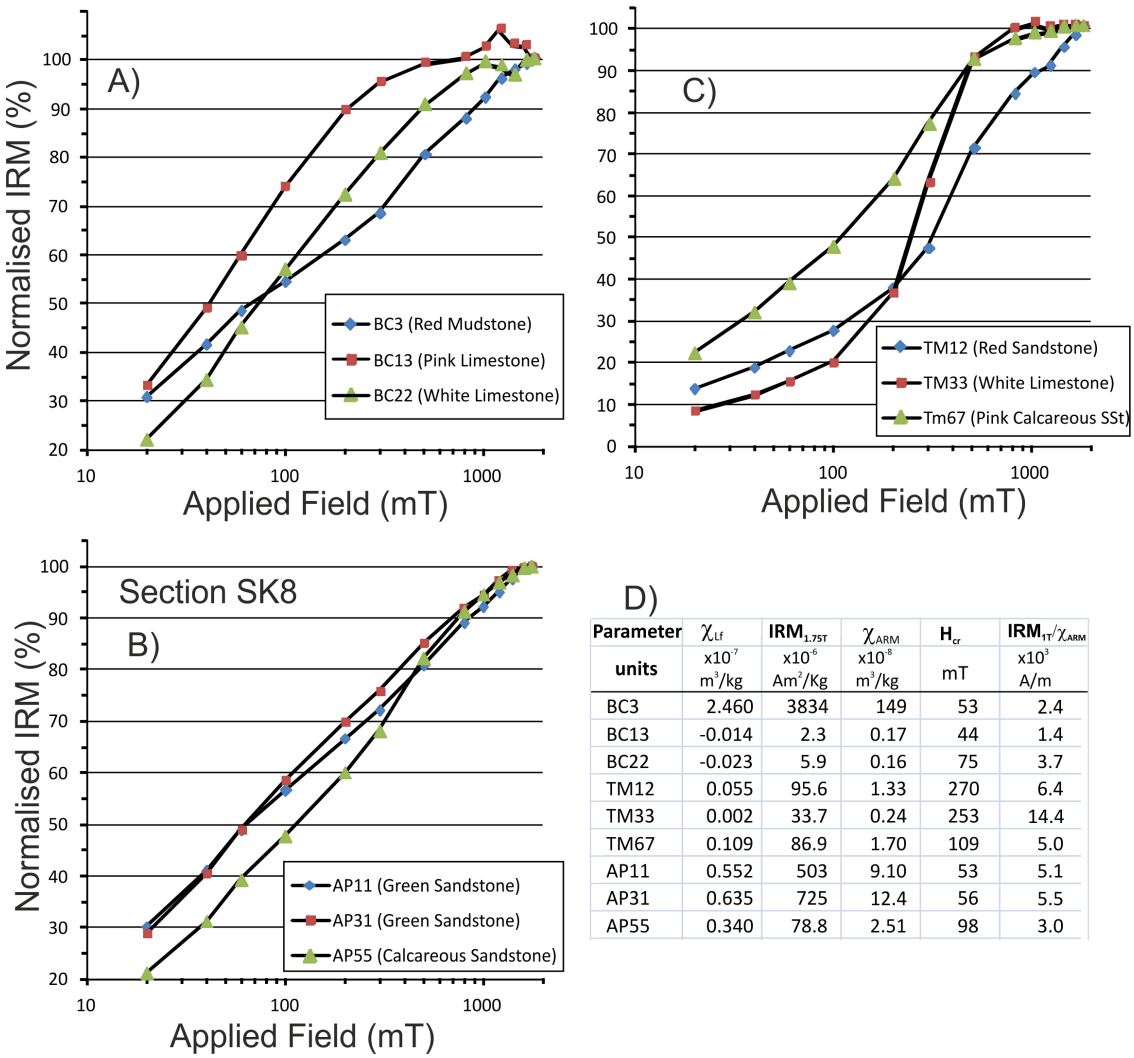

D)

Parameter	χ_{LF}	$IRM_{1.75T}$	χ_{ARM}	H_{cr}	IRM_{1T}/χ_{ARM}
units	x10^{-7} m^3/kg	x10^{-6} Am^2/Kg	x10^{-8} m^3/kg	mT	x10^3 A/m
BC3	2.460	3834	149	53	2.4
BC13	-0.014	2.3	0.17	44	1.4
BC22	-0.023	5.9	0.16	75	3.7
TM12	0.055	95.6	1.33	270	6.4
TM33	0.002	33.7	0.24	253	14.4
TM67	0.109	86.9	1.70	109	5.0
AP11	0.552	503	9.10	53	5.1
AP31	0.635	725	12.4	56	5.5
AP55	0.340	78.8	2.51	98	3.0

Fig. S6. Rock magnetic data for representative specimens from the Shabirinah and Brak formations. A,B and C show normalised isothermal remanent magnetisation data with respect to the (backfield) magnetic field applied, and type of specimen lithology. D) Shows summary magnetic properties of mineral abundance parameters of low frequency magnetic susceptiblity (χ_{LF}), saturation magnetisation at 1.75T (IRM 1.75T) and susceptibility of anhysteretic magnetisation (χ_{ARM}). The coercivity of remanence (H_{cr}) and the magnetite granulomtry proxy IRM_{1T}/χ_{ARM} are shown.

3. U-Th and U-Pb dating, methods and details

3.1 Sample preparation

Fourteen carbonate samples from the TS2 and TS3 sections were sub-sampled for assessment of suitability for U series geochronology. Sub-sample slabs containing relatively unaltered carbonate were obtained using a Dremel tool fitted with a diamond cutting disk and ultrasonically cleaned in water. These slabs were mounted in 25 mm diameter epoxy mounts that were polished flat and the top surface sliced off for preparation of 100 µm-thick petrographic sections for microscopy. The petrographic sections permit transmitted light microscopy but were thick enough to facilitate SEM imaging (e.g. cathodoluminescence) without burning the surface due to charge build-up and also to facilitate potential follow-up laser ablation ICP-MS analysis. The remaining mount was re-ground with diamond paste to yield a flat and highly polished surface suitable for laser ablation ICP mass spectrometry (LA-ICP-MS) and reflected light microscopy. Sub-sample slabs for solution-mode U-Th isotope analysis were obtained adjacent to the petrographic sample locations.

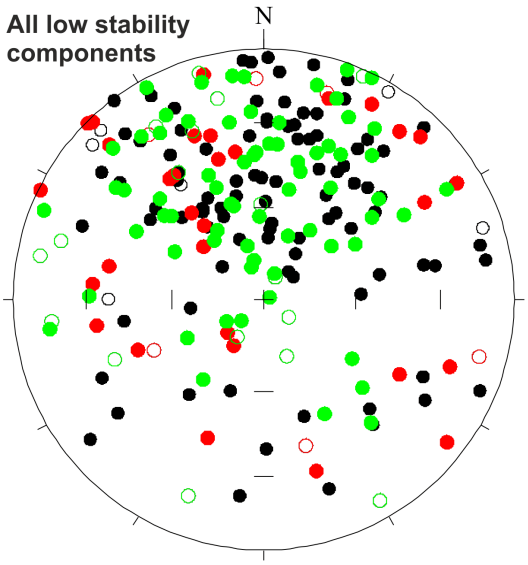

Eigen mean= Declination =356.2°, Inclination = 43.4° R= 133.419, n=225. Type:Bipolar, Rotational Symmetry of Bipolar distribution accepted at 95% probability, 95% Circular confidence Cone: 8.3°

Fisher Mean. Normal Polarity Directions: Dec= 354.9°, Incl.= 45.0°, Alpha(95%)= 6.2°, k= 3.63, n= 198, R= 143.7628, R-bar= 0.7261,

Fisher Mean, Reverse Polarity Directions: Dec.= 174.4°, Incl.= -17.7°, Alpha(95%)= 32.7°, k= 1.71, n= 27, R= 11.7576, R-bar= 0.4355,

All directions converted to Normal Polarity: Dec.= 354.8°, Inc.= 43.0°, Alpha(95%)= 6.4°, k= 3.17, n= 225, R= 154.3089, R-bar= 0.6858,

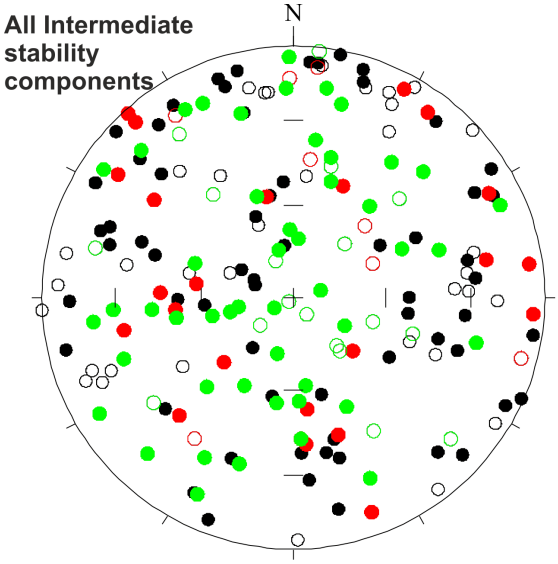

Intermediate stability components
Eigen Mean statistics

Tao	1	2	3
Declination	62.8°,	326.1³,	220.2°
Inclination	32.0°,	10.6³,	55.9°
EigenValue	57.5080,	65.5971,	73.8949 R= 46.886, n=197

Uniformity Hypothesis accepted- vectors apparently random

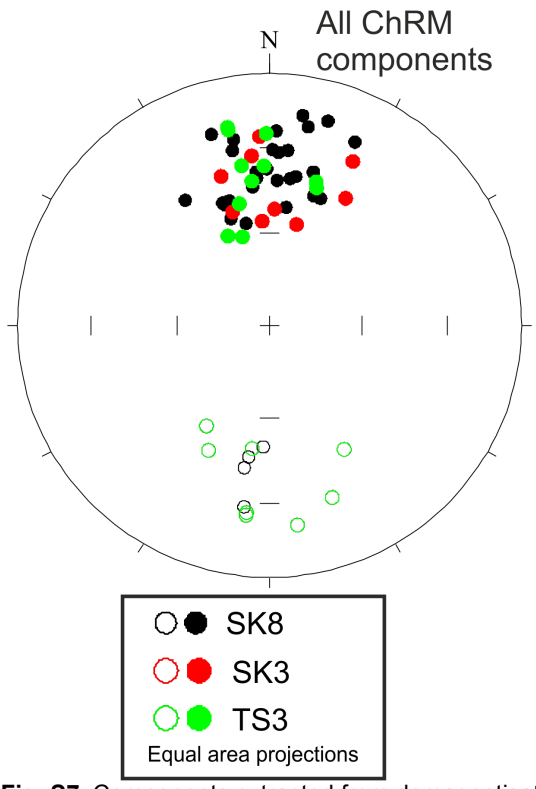

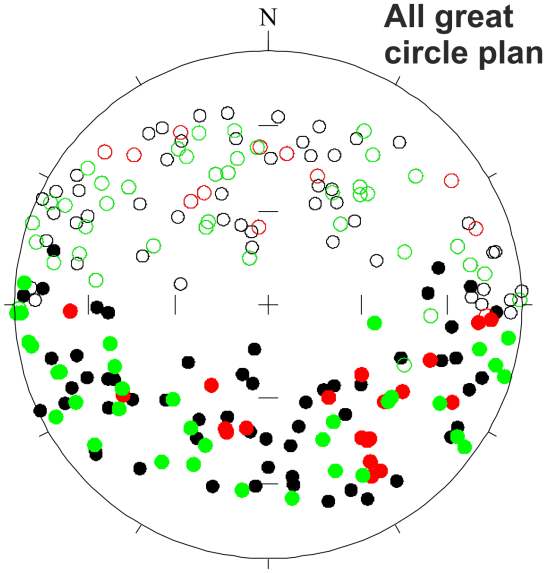

Eigen Mean Statistics

Tao	1	2	3
Declination	183.6°,	256.9°,	332.1°
Inclination	-44.3°,	16.4°,	-41.1°
EigenValue	10.7293,	90.7331,	112.5376, R= 9.499, n=214

Distribution Type: Girdle, with girdle plane spanned by Tao2 and Tao 3 with girdle pole at Tao1
Rotational Symmetry of Girdle distribution accepted at 95% probability
95% Circular confidence Cone: 3.8°

Fig. S7. Components extracted from demagnetisation data, and their statistical evaluation. The ChRM statistics are detailed in Table 2.

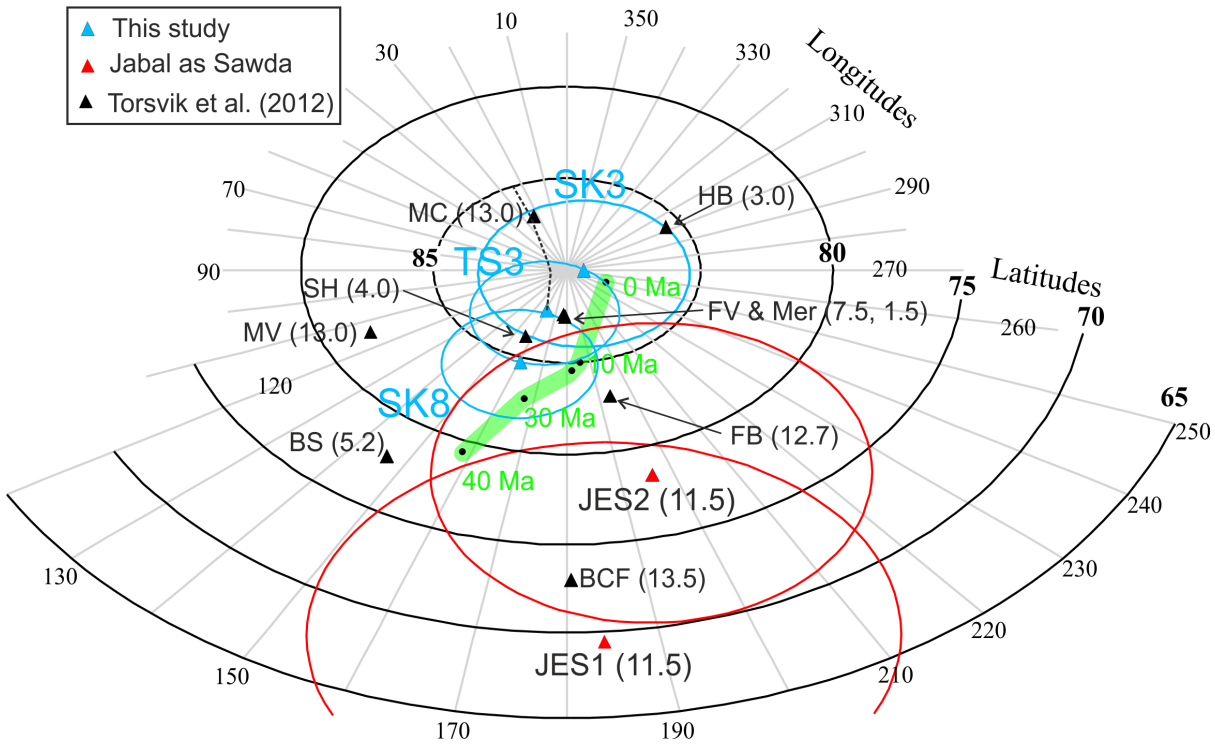

Fig. S8. Miocene to recent North African palaeopoles, with 95% confidence cones shown for the Libyan data. Blue are data from this study, red from Jebal as Sawda (JES1 = Ade-Hall et al. 1975; JES2 = Schultz & Soffel, 1973). Green is the Gondwana apparent polar wander path (APWP) from Torsvik et al. (2012; Table 7), labeled in 10 Ma increments. Other labels in black are poles (age in Ma), listed inTorsvik et al. (2012). FV=Famara Volcanics, Canary Islands (CI); BS= Basalt Series II, CI; MV= Miocene Volcanics, CI; MC=Basalt Series I, CI; Mer= main Ethiopian rift basalts; HB= Hadar Basin, Ethiopia; SH= South Holhol-Djibouti; BCF= Blue Clay Formation, Malta; FB=Ethiopian flood basalts. Dashed line from the TS3 pole is the expected trend in the pole position, if we undid ~5^{o} of inclination shallowing. Similar trends are shown with the SK poles.

3.2 Petrography

Microscopy showed most of these samples contained significant silicate detritus rendering them unsuitable for U-Th geochronology. Generally, unsuitable samples possessed a uniform detritus distribution precluding an isochron approach, while a further sample (FEZZ/04/64/2) was unsuitable due to the presence of several carbonate generations that could not be isolated and individually sampled, due to their small physical dimensions. Samples that passed screening for detritus and considered the most likely to be successful for geochronology (SI Fig. S8; SI Table S2) included micritic limestones TM3, TM6, TM8, and FEZZ/04/64/5, and two coarser-grained limestones FEZZ/04/64/4 and FEZZ/04/64/6.

3.3 Laser ablation reconnaissance for in-situ U-Pb and U-Th analysis

LA-ICP-MS screening of these samples was done along line rasters on all chips using a New Wave Research 193 nm excimer UV laser fired at 10 Hz using a ca. 100 μm diameter laser spot at ca. 7 J/cm^2 fluence. All ablations employed He as the ablation cell carrier gas. Some samples were screened using a Nu Instruments MC-ICP-MS fitted with a U-Pb optimized detector block (Horstwood et al., 2003), while other samples were screened using a Nu single collector fast scanning sector field ICP-MS (SF-ICP-MS) following analytical protocols in Roberts and Walker (2016). Only semi-quantitative data were obtained, given the aim was to locate regions favourable for subsequent detailed analysis. Areas within a single sample chip that yielded a spread in U/Pb elemental and Pb isotope ratios for the chip as a whole were sought. Unfortunately, insignificant variation in U/Pb ratio, together with relatively uniform Pb isotope ratios of common Pb composition, were the norm, with the conclusion that the carbonate U and Pb contents and isotope characteristics

precluded their use for U-Pb geochronology. Additionally, the semi-quantitative uranium and thorium ion beam intensity data showed that while carbonates have ca. 0.1-2 ppm U contents, the amounts of accompanying ^{232}Th indicate their relative unsuitability for U series geochronology. Furthermore, direct determination of U series ages was impossible given ^{230}Th signals at or below the detection limit of the instrumentation.

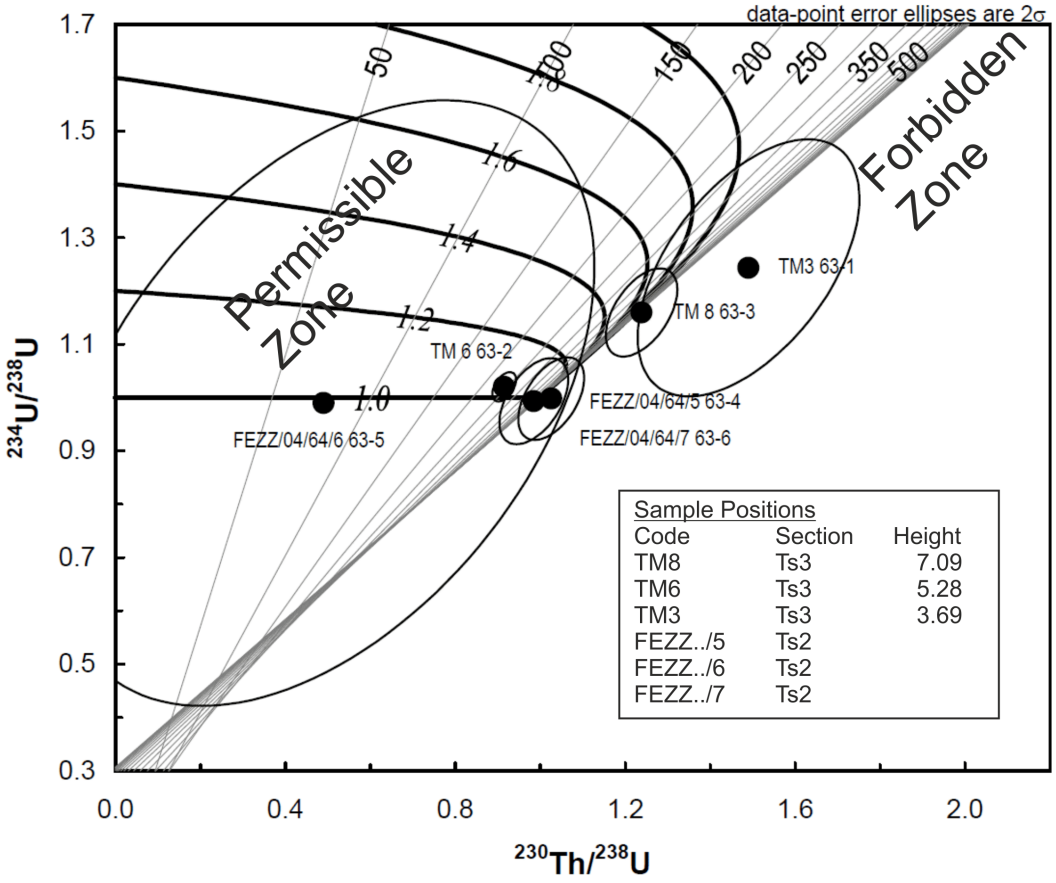

Fig. S9. The detrital Th-corrected 230Th/238U vs 234U/238U data. A series of sloping lines represent age contours (50 to 500 ka). Data points to the right of the 500 ka contour (approximate 230Th/234U secular equilibrium) plot in a 'forbidden zone' where the observed isotope compositions cannot be generated by normal U decay to Th. Such forbidden zone data are indicative of open-system conditions in samples and so no age can be determined because the main prerequisite condition required for application of the U-Th age equation is violated.

Sample	U (ppm)	^{232}Th (ppb)	$^{230}Th/^{232}Th$	±2σ (%)	$^{230}Th/^{238}U$*	±2σ (%)	$^{234}U/^{238}U$*	±2σ (%)	ρ 08-48	$\delta^{234}U$ init	±2σ (abs)	Age (ka, BP)	±2σ (abs)
TM 3	1.1	1.08	4.1	±2.0	1.4900	±14.3	1.243	±15.8	0.54			>500	
TM 6	1.50	0.24	17.8	±1.8	0.9149	±2.5	1.020	±2.2	0.49	1.0400	±0.04	242.0	±23.7
TM 8	1.28	0.55	8.6	±1.8	1.2390	±5.5	1.160	±5.8	0.05			>500	
FEZZ/04/64/4	5.40	2.21	7.6	±1.4	1.0260	±6.2	0.998	±6.3	0.50			>500	
FEZZ/04/64/5	0.51	0.90	1.3	±1.7	0.4898	±106.4	0.990	±46.9	0.45	0.9870	±0.57	74.4	±101.6
FEZZ/04/64/6	3.25	1.38	7.0	±2.5	0.9847	±6.7	0.993	±6.6	0.50	0.9670	±0.44	>500	

Notes: * activity ratios corrected for detrital Th using average continental detritus U/Th and Th isotope composition;
** Age in ka (detrital Th-corrected), BP relative to 2016 AD; italics indicate activity ratios.
Ages calculated using the decay constants of Cheng et al. (2013)

Supplementary Table S2. Solution-mode U-Th data summary. Corrections for detritus contributions assumed an average continental U and Th composition ([^{232}Th/^{238}U] = 1.2 ± 50%, [^{230}Th/^{238}U] = 1 ± 50%, and [^{234}U/^{238}U] = 1 ± 50%). For the samples that passed screening for detritus, and the estimated ages. All samples are from the carbonate bed in the Stromatolite Mbr. FEZZ/04/64/.. samples from 26, 30, 51.1N; 16,29, 58.2E.

3.4 Solution-mode U-Th chronology

Six samples with the lowest content of silicate detritus from the TS2 and TS3 section samples were analysed for U-Th, to further investigate the carbonate isotope systematics. The samples were subjected to total dissolution using a mixture of concentrated HNO_3-$HClO_4$-HF and U and Th separated by anion ion exchange chemistry. U and Th isotope data were obtained on a Neptune Plus multicollector ICP-MS. These analytical protocols are described in detail by Douarin et al. (2013). The U and Th decay constants of Cheng et al. (2013) were used in all activity ratio and age calculations. Raw data were processed using the Isoplot add-in (Ludwig, 2013) and in-house reduction engines employing Excel and Matlab.

3.5 U-series results

The best samples in terms of relatively low Si-detritus content were assessed for U-Pb by both laser ablation ICP-MS, and analysed for U-Th by solution-mode ICP-MS. However, the fairly homogeneous distribution and abundance of Si-detritus relative, to host carbonate, indicated these samples were unsuitable for U-Th chronology (SI Fig. S9). This is since isochron methods only help where a large spread in the relative proportions of silicate detritus and carbonate occurs in the samples.

Sample TM3 is the worst case and is far enough to the right of the secular equilibrium age contour to suggest significant open-system U-Th behaviour (SI Fig. S9). Th is relatively immobile but in oxidizing environments uranium is very mobile and recrystallisation or major disturbance of the carbonate at any time can cause uranium to be redistributed. Uranium loss would explain the measured isotope composition of TM3. TM8 and FEZZ/04/64/5 and FEZZ/04/64/7 also plot slightly in the forbidden zone, albeit sufficiently close to the secular equilibrium isotope composition so as to indicate only limited open-system behaviour or a slight inaccuracy in the Th isotope composition assumed for the detritus that is used to correct the raw isotope data. If the latter is the case then these samples record closed systems that are at least 500 ka old. Two analyses plot in the permissible zone for closed isotope systems (Fig. S9). TM6 had the highest [^{230}Th/^{232}Th] of all the samples and yielded an age of 242 ± 24 ka (Table S2). The validity of this age would depend upon it being in correct stratigraphic order relative to TM8 (which it is not). Sample TM3 plots so far into the forbidden zone (not shown) that it can be dismissed from consideration when interpreting the significance of the data for the other two TM samples. The other sample in the permissible zone is FEZZ/04/64/5 which has such a low [230Th/232Th] as to render corrected isotope ratios and calculated “age” highly suspect given that the other FEZZ samples suggest true ages >500 ka. Given that open system behaviour is possible in some of these samples, the same may apply here and this young “age” could easily be accounted for by uranium influx.

Given the general unsuitability of the rocks that were analysed, and those that were eliminated during the initial screening, we can say emphatically that they are unsuited to U-Th analysis. The chronology of these rocks needs to be investigated with other methods, unless much cleaner carbonates can be found.

4. Details of the sequence slotting and age models

A graphical expression of the two best fitting sequence slotting correlations is shown in SI Fig. S10, for the two magnetostratigraphic composites A and B. In a visual sense, it is clear that both the Serravallian correlation models show a better match to the GPTS, particularly for the interval younger than chron C6. The Tortonian correlation models tend to show a poor match over the chron interval C5AD to C5A.

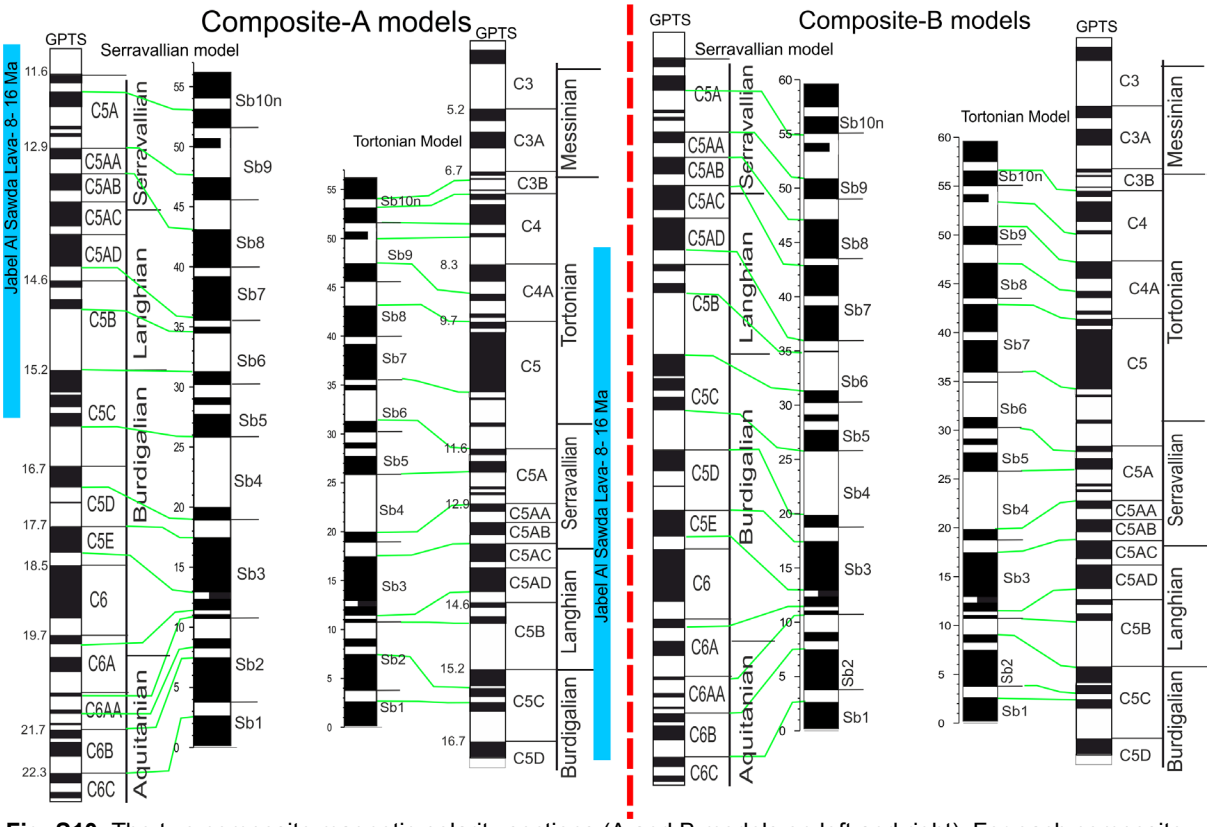

Fig. S10. The two composite magnetic polarity sections (A and B models on left and right). For each composite model the two most likely correlations to either of the intervals is shown which begin in the Serravallian and the latest Tortonian. Correlation lines shown in green derived from the sequence slotting.

Since the sequence slotting does not 'know' that normal polarity should correlate with normal polarity, we force it into this, by weighting the polarity variable (set at either -1 or +1 value) with a value of 5 times the base value of 1.

The alternative correlation models can clearly be seen in the H-matrix plots (SI Fig. S11b, S11b), by the brighter bands inclined down to the right across the plot. The values shown on the H-matrix plots are the ratio of the constrained path (i.e. as the matched composite polarity data is incrementally slid past the GPTS) relative to the (optimum) minimum CPL, with brighter values indicating path-length values near the CPL optimum (Gordon et al 1988). These give a visual clue to the search paths (i.e. somewhat similar to similarity matrix plots in Gary et al., 2005) sought by the sequence slotting, which in a simple sense find the path with the 'brightest response' through this matrix.

The Oligocene correlation model (Composite B, SI Fig. S12a) actually gives the lowest Δ value, only marginally lower than the composite B Serravallian model. This is also the case for the N-CSTAT value. However, the high degree of inter-chron variability in the parameters (see description of Δ value in Table S3) makes these slotting parameters less useful for considering the best overall fit. In terms of the RV association parameters, and the individual parameter correlations (i.e. Spearman R_s, SI Fig. S12a) between matched chrons and magnetozones, the Oligocene age model is the worst fitting (SI Fig. S12a).

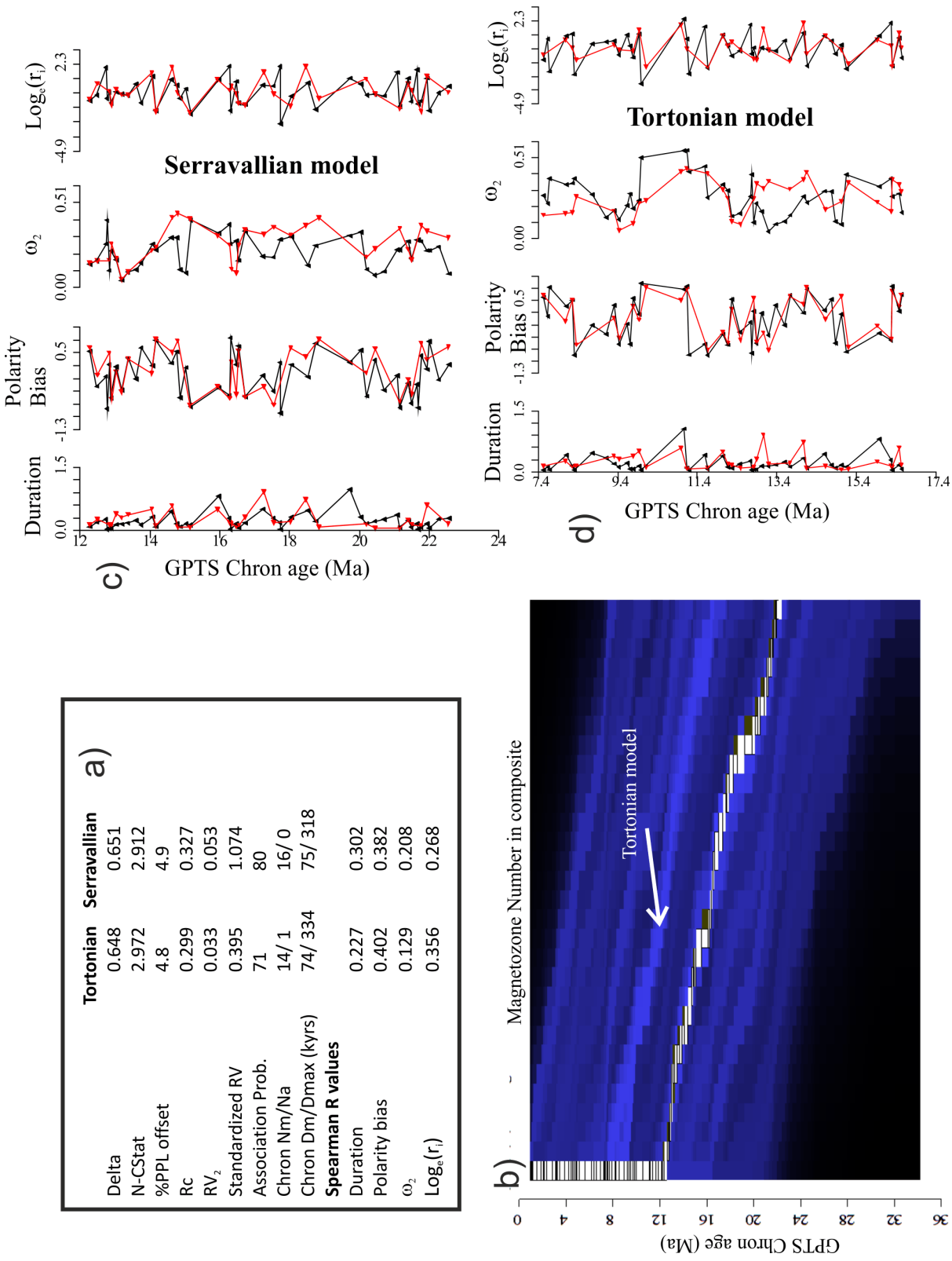

	Tortonian	Serravallian
Delta	0.648	0.651
N-CStat	2.972	2.912
%PPL offset	4.8	4.9
Rc	0.299	0.327
RV_2	0.033	0.053
Standardized RV	0.395	1.074
Association Prob.	71	80
Chron Nm/Na	14/ 1	16/ 0
Chron Dm/Dmax (kyrs)	74/ 334	75/ 318
Spearman R values		
Duration	0.227	0.302
Polarity bias	0.402	0.382
ω_2	0.129	0.208
Log$_e$(r$_i$)	0.356	0.268

Fig. S11. Sequence slotting model output for the magnetic polarity composite-A, shown on the left panel in Fig. S10. a) the statistical summary of the Tortonian and Serravallian correlation models (see Table S3 for parameter description). b) The H-matrix plot, where the brighter blue bands correspond to alternative correlation models. The mostly likely model (ending in Serravallian) is shown as the white boxes across the plot, with y-axis height (of the boxes) corresponding to GPTS chron duration. The band corresponding to the Tortonian model is arrowed. The x-axis on this plot is the magnetozone number. Green boxes indicate alternative 'slots' the same as the optimum. c) and d) The input data to the slotting model, plotted against chron age for the two correlation options (shown in left panel in Fig. 10), derived from the sequence slotting. GPTS chron data in red, section data in black. Parameters described in Table S3.

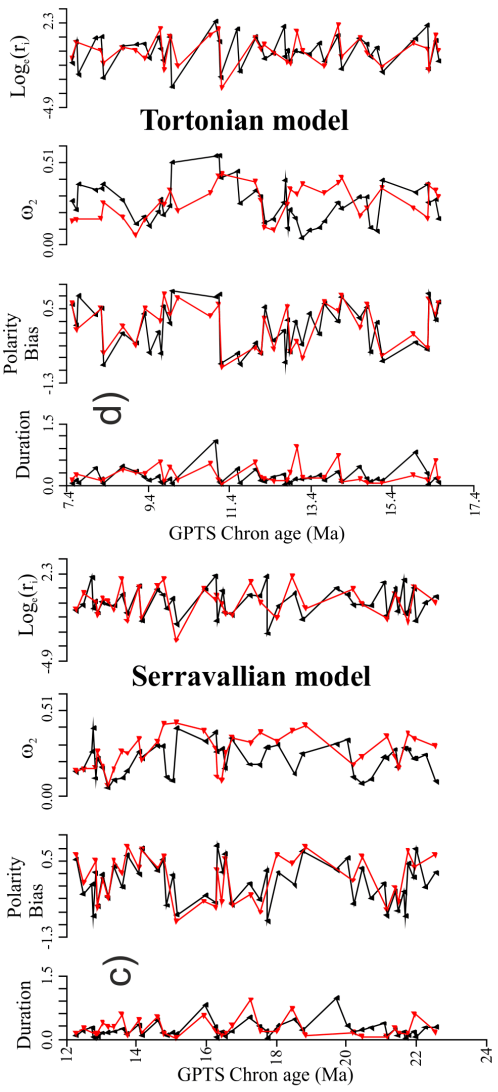

a)	Tortonian	Serravallian	Oligocene
Delta	0.636	0.638	0.630
N-CStat	2.969	2.925	2.832
%PPL offset	8.3	6.1	8.6
Rc	0.282	0.416	0.150
RV_2	0.016	0.126	0.020
Standardized RV	0.443	2.65	0.118
Association Prob.	73	90	70
Chron N_m/N_a	12/1	14/0	18/0
Chron D_m/D_{max} (kyrs)	113/245	56/318	
Spearman R values			
Duration	0.198	0.330	0.118
Polarity Bias	0.537	0.475	0.313
ω_2	0.129	0.201	0.031
Log$_e$ (r$_1$)	0.431	0.320	0.353

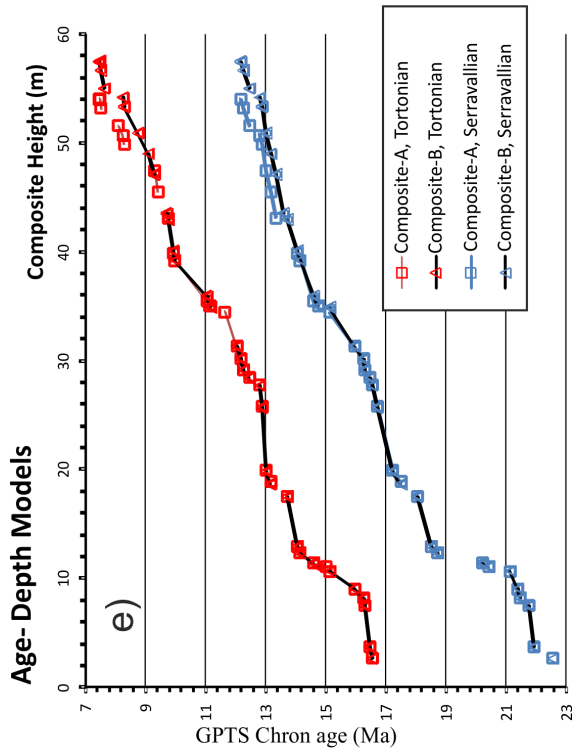

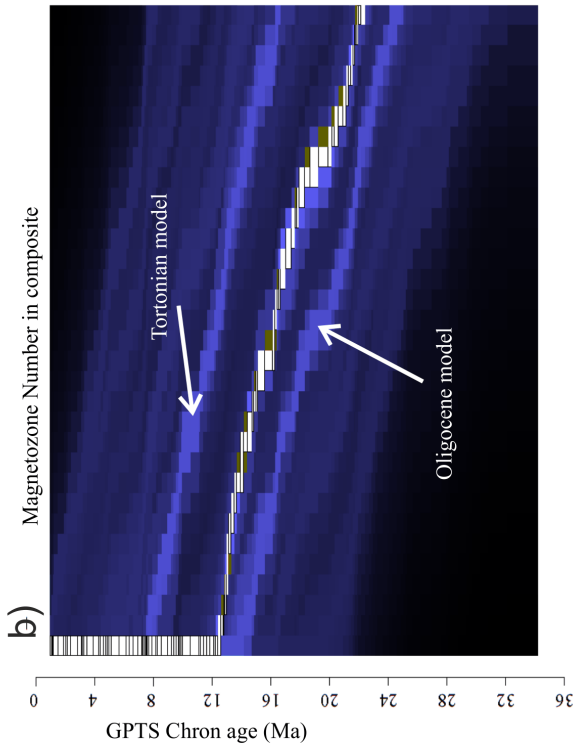

Fig. S12. Sequence slotting model output for the magnetic polarity composite-B (right panel in Fig. S10), showing data for the three mostly likely correlation models. a) to d) details as in Fig. S11 (parameters shown in A) detailed in Table S3). e) Depth-age models for the two polarity composites A and B, and the Tortonian and Serravallian age models. The age-depth relationships for the two age models are similar for composite A and B apart from the upper part of the composite sections. Parameters described in Table S3.

Statistic	Description and comments
Delta (Δ)	Δ= (2**min*(CPL))/(APL + BPL) – 1, where CPL is the combined path length, or the total discordance between the start and end of the matched points (in multivariate space) when slotted together. APL is the individual path length through the GPTS chrons, and BPL is the individual path length through the matched data. The value of the CPL is controlled by the type of scaling and distance measure used, since this will control the magnitude of the discordance measured by CPL (see Thompson and Clark, 1989). The best slotting model of the many considered for each slotting run is that with the minimum CPL (hence *min*(CPL)), where the *min* indicates the search criteria. Δ is a goodness of match statistic independent of the chosen distance measure and the units of measurements used, and measures of the 'local-fit' of the two sequences. If correctly scaled, Δ generally lies between zero and somewhere around 1.0; a small value of Δ (less than ca. 0.5) indicates that Sequences A and B are interleaved or slotted together very well (Thompson and Clark, 1989; Thompson et al., 2012). Generally the Δ value expresses the goodness of fit well with datasets which have a low degree of inter-level variability (i.e. smoothly varying wiggles). In contrast, the parameterisation of the GPTS tends to give high variability between the chrons, since chron durations have a near random distribution (Lowrie and Kent, 2004).
N-CSTAT	The normalised CSTAT. A measure of the robustness of the fit, base on a sensitivity analysis (Gordon et al., 1988). Generally smaller N-CSTAT values are associated with better, more robust slotting. The CSTAT value is a sensitivity statistic, which is the reduction in the CPL when a particular chron in the GPTS is omitted (i.e. a test of the sensitivity of the model to missing chrons in the GPTS). i.e. each GPTS chron has a CSTAT value. The N-CSTAT value is the average CSTAT value divided by the average PPL.
%PPL offset	The PPL is the partial path length, or the discordance between adjacent points or (path length of sub-segments of the total CPL). %PPL is simply the sum of the absolute discordance between those matched chrons and magnetozones in the GPTS and matching sequence, expressed as a percentage of the CPL. Better match's should have lower %PPL in any set of slotted models. The Serravallian model for composite B has the lowest %PPL value, whereas for the polarity composite A the two age models have similar values.
R_c	The congruence coefficient a measure of the similarity (or association) of the two datasets. It measures the similarity of two configurations by computing a cosine between matrices of observations. R_c has a range like regression coefficients (i.e. up to +1 for positive association), but is not a regression coefficient (see Abdi, 2010). The largest R_c value is the Serravallian age model for composite B. Broadbooks and Elmore (1987) provide a method to test if R_c is significantly different from zero.
RV_2	The RV coefficient is a measure of the similarity (or association) of the two datasets. It is a matrix correlation coefficient. It corresponds to a squared cosine and therefore the RV coefficient takes values between 0 and 1 (Abdi, 2010). The RV_2 coefficient is a modification of the RV coefficient (taking values -1 to +1) according to Smilde et al. (2009) and is a more robust measure of common information contained in the two datasets. The largest RV_2 value is from the Serravallian age model for composite B.

RV_{std}	This is the standardized RV coefficient of Josse et al. (2008) (and Z_{Rv} statistic of Abdi 2007) which allows an approximate evaluation if the RV coefficient is significantly different from zero. Values of RV_{std} >1.65 suggest the RV value reflects a significant association between the two datasets. However, the tests in Josse et al. (2008) suggest RV_{std} should be >~2 for an approximate 95% confidence value. Only the Serravallian age model for composite B has RV_{std} >1.65 (SI Fig. S12a).
Association probability, P_a	This is derived from the log-transformed Z statistic in Josse et al. (2008), which is tested against a standard normal distribution (SI Figs. S10a, S12a). This approximation evaluates the probability ($p=1-P_a$) that the RV coefficient is significantly different from zero. i.e. Larger values of the association probability, P_a indicate a better match between the datasets. The Serravallian age model for composite B has the largest P_a value (SI Fig. S12a). RV_{std} and P_a do not indicate the 'significance of the match', but only the probability of some association between the datasets.
N_m/N_a	N_m= number of chrons missing from the GPTS in the magnetostratigraphic match. N_a= number of additional magnetozone in the matched succession not present in the GPTS. These numbers should be at a minimum for a good match, but will depend on the sampling rate of the GPTS. N_a values >=1 imply spurious magnetozones in the section not present in the GPTS. Both of the Tortonian models have spurious magnetozones present in C5An (SI Fig. S10).
D_m/D_{max}	D_m= mean duration (in kyrs) of chrons missing from the GPTS in the match. D_{max}= duration of longest chron missing from the GPTS in the match (in kyrs). These give an idea of the missing time represented in the match. The longest chron missing is C6r for the Serravallian models, and C4An or C5ABn for the Tortonian models.
Spearman coefficients (R_s)	These are the rank correlation coefficients between the values of the two dataset of the duration, polarity bias, ω_2 and $Log_e(r_i)$ used in the sequence slotting procedure (using the correlation model given by the sequence slotting). Clearly larger values of R_s would be expected for better matches. The R_s allows a comparison of which are the stronger control variables in the matching process. In this case, for both composite models the polarity bias, and $Log_e(r_i)$ seem to be generally stronger than duration and ω_2 (SI Figs. S11a, S12a). This can be seen by inspecting the dataset co-plots with GPTS age in SI Fig. S11c,d and SI Fig. S12c,d.
Polarity Bias parameter	For chron/magnetozone i, the polarity bias= $\sum_{j=i-1}^{j=i+1} d_j p_j / \sum_{j=i-1}^{j=i+1} d_j$, where d_j is the duration of the chron or magnetozone, and p_j is the polarity (values -1 or +1) of the chron or magnetozone. It ranges from intervals in which reverse polarity dominates (bias <-0.5) to intervals in which normal polarity dominates (bias >+0.5).
Shearmans spacing statistic ω_2	$\omega_{2=} \frac{0.5*\sum_{j=i-1}^{1+1} abs(\overline{d}-d_j)}{\sum_{j=i-1}^{i+1} d_j}$, where d_j is the chron or magnetozone duration, and $\overline{d}$ is the mean duration in the interval i-1 to i+1 (see Olson et al., 2014). i.e. ω is a measure of how much the durations deviate from their average length.

Supplementary Table S3. Explanation of statistics derived from sequence slotting, and parameters used in the sequence slotting and shown in SI Figs. S11 and S12.

References

Abdi, H., 2007. RV coefficient and Congruence coefficient. In: Salkind, N. (Ed.), Encyclopaedia of measurement and statistics. Thousand Oaks, CA: Sage, pp. 850-856.

Abdi, H., 2010. Congruence: Congruence coefficient, RV -coefficient, and Mantel coefficient. In: Salkind, N. (Ed.), Encyclopaedia of Research Design. Thousand Oaks, CA, Sage, pp. 223-230.

Abdullah, M., 2010. Petrography and Facies of the Al- Mahruqah Formation in the Murzuq Basin, SW Libya. (PhD. Thesis), Universität Hamburg.

Ade-Hall, J. M., Reynolds, P. H., Dagley, P., Mussett, A. E., Hubbard, T. P., 1975. Geophysical studies of North African Cenozoic volcanic areas: II. Jebel Soda, Libya. Canadian Journal of Earth Sciences 12, 1257-1263.

Armitage, S.J., Drake, N.A., Stokes, S., El-Hawat, A., Salem, M.J., White, K., Turner, P. McLaren, S.J., 2007 Multiple phases of North African humidity recorded in lacustrine sediments from the Fezzan Basin, Libyan Sahara. Quaternary Geochronology 2, 181–186.

Berendeyev, N.S., 1985. Geological map of Libya 1:250,000, Sheet: Hamadat Tanghirt (NH 32-16) Explanatory Booklet. Industrial Research Centre, Tripoli.

Broadbooks, W. J., Elmore, P. B., 1987. A Monte Carlo study of the sampling distribution of the congruence coefficient. Educational and Psychological Measurement 47, 1–11.

Bown, T. M., 1982. Ichnofossils and rhizoliths of the nearshore fluvial Jebel Qatrani Formation (Oligocene), Fayum Province, Egypt. Palaeogeography, Palaeoclimatology, Palaeoecology 40, 255-309.

Brooks, N., Drake, N., McLaren, S.J., White, K., 2003. Studies in Geography, Geomorphology, Environment and Climate. In: Mattingly, D.J., Dore, J., Wilson, A.I. (Eds.), The Archaeology of Fazzan: Synthesis, Society for Libyan Studies, London, pp. 37–74.

Cheng, H., Edwards, R.L., Shen, C.-C., Polyak, V.J., Asmerom, Y., Woodhead, J., Hellstrom, J., Wang, Y., Kong, X., Spötl, C., Wang, X., Alexander, E.C. Jr., 2013. Improvements in ^{230}Th dating, ^{230}Th and ^{234}U half-life values, and U-Th isotopic measurements by multi-collector inductively coupled plasma mass spectrometry. Earth and Planetary Science Letters 371-372, 82-91.

Collomb, G.R., 1962. E`tude geologique du Jabal Fezzan et de sa bordure Paléozoque. Notes Mémoiré, Compagnie Française des Pétroles, 1, pp. 35-36.

Desio, A., 1971. Outlines and problems of the geomorphological evolution of Libya from the Tertiary to the present day. In: Gray, C. (Ed.), 1st symposium on the geology of Libya. Fac. Sci. Univ. Libya, Tripoli, pp. 11-37.

Drake, N.A, White, K. McLaren, S., 2006. Quaternary climate change in the Germa region of the Fezzan, Libya. In: Mattingly, D., McLaren, S.J., Savage, E. al-Fasatwi, Y., Gadgood, K. (Eds.), The Libyan desert: nature resources and cultural heritage. Society for Libyan Studies, pp. 133-144.

Drake , N.A, El-Hawat, A.S., Turner, P., Armitage, S.J., Salem, M.J., White, K.H., McLaren, S.J., 2008. Palaeohydrology of the Fezzan Basin and surrounding regions: the last 7 million years. Palaeogeography, Palaeoclimatology, Palaeoecology 263, 131-145.

Douarin, M., Elliot, M., Noble, S.R., Sinclair, D., Henry, L.-A., Long, D., Moreton, S.G., Roberts, J.M., 2013. Growth of north-east Atlantic cold-water coral reefs and mounds during the Holocene: A high resolution U-series and ^{14}C chronology. Earth and Planetary Science Letters 375, 176-187.

Gary, A.C, Johnson, G.W. Ekart, D.D., Platon E., Wakefield, M.I., 2005. A method for two-well correlation using multivariate biostratigraphical data. In: Powell, A. J., Riding, J. B. (Eds.), Recent Developments in Applied Biostratigraphy. The Micropalaeontological Society, Special Publications, pp. 205–217.

Geyh, M.A., Thiedig, F., 2008. The Middle Pleistocene Al Mahruqah Formation in the Murzuq Basin, northern Sahara, Libya evidence for orbitally-forced humid episodes

during the last 500,000 years. Palaeogeography, Palaeoclimatology, Palaeoecology 257, 1-21.
Gordon, A.D., Clark, R.M. Thompson, R., 1988. The use of constraints in sequence slotting. In: Diday, E. (Ed.), Data analysis and informatics, V. North Holland Publishing, Amsterdam, pp. 353-364.
Goudarzi, G.H., 1970. Geology and mineral resources of Libya — a reconnaissance. U.S. Geological Survey Professional Paper, 660, 104p
Gundobin, V.M., 1985. Geological map of Libya 1:250,000, Sheet: Qararat al Marar (NH 33-13) Explanatory Booklet. Industrial Research Centre, Tripoli.
Horstwood, M.S.A., Foster, G.L., Parrish, R.R., Noble, S.R., Nowell, G.M., 2003. Common-Pb corrected in situ U-Pb accessory mineral geochronology by LA-MC-ICP-MS. Journal of Analytical Atomic Spectrometry 18, 837-846.
Koráb, T., 1984. Geological Map of Libya 1: 250 000. Sheet: Tmassah NG 33-7. Explanatory Booklet. Industrial Research Centre, Tripoli.
Lowrie, W., Kent, D.V., 2004. Geomagnetic polarity timescales and reversal frequency regimes, In: Channell, J.E.T., Kent, D.V., Lowrie, W., Meert, J. (Eds.), Timescales of the palaeomagnetic field, America Geophysical Union, pp. 117-129.
Ludwig, K.R., 2012. Isoplot 3.75: A geochronology toolkit for Microsoft Excel, Berkeley Geochronology Center Special Publication 5, 75p.
Parizek, A., Klen, L., Rohlich, P., 1984 Geological map of Libya 1:250,000, Sheet: Idri (NG 33-1) Explanatory Booklet. Industrial Research Centre, Tripoli.
Petit-Maire, N., Delibrias, G., Gaven, C., 1980. Pleistocene lakes in the Shati area, Fezzan (27, 30'N). Palaeoecology of Africa, 12, 289-295.
Josse, J. Pages, J., Husson, F., 2008. Testing the significance of the RV Coefficient. Computational Statistics and Data Analysis 53, 82-91.
Olson, P., Hinnov, L., Driscoll, P., 2014. Nonrandom geomagnetic reversal times and geodynamo evolution. Earth Planetary Science Letters, 388, 9–17.
Roberts, N.M.W., Walker, R.J., 2016. U-Pb geochronology of calcite-mineralized faults: Absolute timing of rift-related fault events on the northeast Atlantic margin. Geology (published on-line June 2016, DOI: 10.1130/G37868.1).
Roncevic, N.S., 1984. Geological map of Libya 1:250,000, Sheet: Hasi Anjiwal (NG 32-4) Explanatory Booklet. Industrial Research Centre, Tripoli.
Seidl, K., Röhlich, P., 1984. Geological map of Libya, 1: 250 000. Sheet Sabhá (NG 33-2), Explanatory Booklet, Industrial Research Centre, Tripoli.
Schultz A., Soffel H.C., 1973 Paleomagnetism of Tertiary basalts from Libya. Geophysical Journal of the Royal Astronomical Society, 32, 373–380.
Smilde, A. K., Kiers, H.A.L., Bijlsma S., Rubingh C.M., van Erk, M.J., 2009. Matrix correlations for high-dimensional data: the modified RV-coefficient. Bioinformatics 25, 401–405.
Thiedig, F.M., Oezen, D., El-Chair, M., Geyh, M.A., 2000. The absolute age of the Quaternary lacustrine limestone of the Al Mahruqah Formation - Murzuq Basin, Libya. In: Sola, M.A., Worsley, D. (Eds.), Geological Exploration in the Murzuq Basin. Elsevier, Amsterdam, pp. 89–116.
Thompson, R., Clark, R.M., 1989. Sequence slotting for stratigraphic correlation between cores: theory and practice. Journal of Paleolimnology 2, 173–184.
Thompson, R., Clark, R.M., Boulton, G.S., 2012. Core correlation. In: Birks, H.J.B., Lotter, A.F. Juggins, S., Smol, J.P. (Eds.), Tracking Environmental Change Using Lake Sediments: Data Handling and Numerical Techniques, Developments in Paleoenvironmental Research, Volume 5, pp. 415–430.
Torsvik, T. H., Van der Voo, R., Preeden, U., Mac Niocaill, C., Steinberger, B., Doubrovine, P. V., van Hinsbergen D.J.J., Domeiere, M., Gaina, C., Tohver, E. , Meert, J.G., McCausland, P. J.A., Cocks, L. R. M., 2012. Phanerozoic polar wander, palaeogeography and dynamics. Earth-Science Reviews 114, 325-368.
White, K., McLaren, S., Black, S., Parker, A., 2000. Evaporite minerals and organic horizons in sedimentary sequences in the Libyan Fezzan: implications for palaeoenvironmental reconstruction. In: McLaren, S.J., Kniveton, D.R. (Eds.), Linking

Climate Change to Land Surface Change. Kluwer Academic Press, Amsterdam, pp. 193–208.

White, K., Charlton, M., Drake, N., McLaren, S., Mattingly, D., Brooks, N., 2006. Lakes of the Edeyen Awbari and the Wadi al-Hayat. In: Mattingly, D., McLaren, S. J., Savage, E., al-Fasatwi, Y. & Gadgood, K. (Eds.), The Libyan Desert, Natural Resources and Cultural Heritage. The Society for Libyan Studies, London, pp. 123–130.